

THE MECHANISM OF BRITTLE FRACTURE IN CN3MN GRADE
SUPERAUSTENITIC STAINLESS STEEL

A THESIS SUBMITTED TO
THE GRADUATE SCHOOL OF NATURAL AND APPLIED SCIENCES
OF
MIDDLE EAST TECHNICAL UNIVERSITY

BY

MERTCAN BAŞKAN

IN PARTIAL FULFILLMENT OF THE REQUIREMENTS
FOR
THE DEGREE OF MASTER OF SCIENCE
IN
METALLURGICAL AND MATERIALS ENGINEERING

FEBRUARY 2015

Approval of the thesis:

**THE MECHANISM OF BRITTLE FRACTURE IN CN3MN GRADE
SUPERAUSTENITIC STAINLESS STEEL**

submitted by **MERTCAN BAŞKAN** in partial fulfillment of the requirements for the degree of **Master of Science in Metallurgical and Materials Engineering Department, Middle East Technical University** by,

Prof. Dr. Gülbin Dural Ünver

Dean, Graduate School of **Natural and Applied Sciences**

Prof. Dr. Cemil Hakan Gür

Head of Department, **Metallurgical and Materials Engineering**

Assoc. Prof. Dr. Yunus Eren Kalay

Supervisor, **Metallurgical and Materials Eng. Dept., METU**

Examining Committee Members:

Prof. Dr. Tayfur Öztürk

Metallurgical and Materials Eng. Dept., METU

Assoc. Prof. Dr. Yunus Eren Kalay

Metallurgical and Materials Eng. Dept., METU

Prof. Dr. Cemil Hakan Gür

Metallurgical and Materials Eng. Dept., METU

Prof. Dr. Bilgehan Ögel

Metallurgical and Materials Eng. Dept., METU

Assist. Prof. Dr. Caner Şimşir

Manufacturing Eng. Dept., ATILIM UNIVERSITY

Date: 04.02.2015

I hereby declare that all information in this document has been obtained and presented in accordance with academic rules and ethical conduct. I also declare that, as required by these rules and conduct, I have fully cited and referenced all material and results that are not original to this work.

Name, Last Name: Mertcan BAŞKAN
Signature :

ABSTRACT

THE MECHANISM OF BRITTLE FRACTURE IN CN3MN GRADE SUPERAUSTENITIC STAINLESS STEEL

Başkan, Mertcan

M.S., Department of Metallurgical and Materials Engineering

Supervisor: Assoc. Prof. Dr. Yunus Eren Kalay

February 2015, 91 Pages

Steel is one of the most widely used materials in almost every major engineering application. Their uses extend from the large constructions in the capitals to the small kitchenware products in houses. Steel has been known since the ancient times, and the properties of steel have been enhanced for hundreds of years by the help of the improvements in metallurgy and material science. Steel has been almost at the center to the discovery-based development of new alloys with notable properties. The steel family has been still growing with the innovations in compositions, heat-treatments and production techniques.

Attributed primarily to its remarkable deteriorative properties, CN3MN, is one of the significant Super Austenitic Stainless Steel (SSS), which is a subclass of austenitic stainless steels. Main application areas of CN3MN are marine constructions and oil wells due to their excellent corrosion resistance and superior toughness. However, according to the results of recent time temperature transformation (TTT) diagrams, incorrect heat-treatments for as short as 15 minutes causes fracture toughness of the alloy to decrease by 50% as embrittlement occurs. Wrought steel pieces are typically smaller in size and can be heat-treated and cooled rapidly in order to avoid

embrittlement. However, in the case of cast superaustenitic stainless steel, cooling rate is much slower so the regions suffered from such embrittlement is extended.

The focus of this study is to understand the mechanisms of the embrittlement problem after annealing heat-treatments for very short times i.e. 30 seconds to 16 minutes at 927°C. The fracture surfaces were investigated by using scanning electron microscope (SEM). Failure analysis results showed a ductile to brittle failure transition for relatively short annealing times. The first reason for embrittlement was defined as the precipitates formed at the grain boundaries. Since the intermetallic precipitates are very brittle, they deteriorate the mechanical properties when the brittle network is formed on the grain boundaries. Average precipitate size in 30-second annealed specimen was found to be about 400 nm with a high number density. The crystal structure of the precipitates formed in short-term annealing could not be matched with previously determined secondary phases in austenitic stainless steel. The kinetics of the nucleation and growth was determined to be very sluggish in the previous studies. In this study, it is shown that the newly determined precipitates have relatively high nucleation rates. This is related to inhomogenous distribution of Mo after the homogenization. These Mo-rich regions are thought to trigger a rapid precipitation.

Second mechanism observed in CN3MN is transgranular embrittlement. The heat-treated specimens contained some cracks with zigzag pattern. Close observation of such defects revealed stacking-fault type imperfections, which lead to step-like cracking observed in micron-length scales. The reason of having such faulted regions was connected to having low stacking fault energy. Stacking fault energy of austenite phase in CN3MN was calculated to be between 12-30 mJ/m² which is quite low for a metallic alloy. Another implication for low SFE was the dislocation distribution. Low SFE promotes entangled dislocation structure instead of subgrain formation, which limits the dislocation motion. The low SFE suppress the crosslinking and climb processes, which are the most active phenomena to maintain dislocation motion. The stacking-fault observed in austenitic matrix changes the FCC by HCP sequence within the defected nano-metric regions. Therefore, the vast majority of transgranular cracks were formed within the brittle HCP-sites resulting into catastrophic transgranular fracture.

Keywords: Stainless steel, CN3MN, Electron microscopy, Defects, Intermetallics

ÖZ

CN3MN SÜPEROSTENİTLİ PASLANMAZ ÇELİKLERDE GEVREK KIRILMA MEKANİZMALARI

Başkan, Mertcan

Yüksek Lisans, Metalurji ve Malzeme Mühendisliği Bölümü

Tez Yöneticisi: Doç. Dr. Yunus Eren KALAY

Şubat 2015, 91 Sayfa

Çelik çok büyük yapılardan evlerdeki küçük mutfak malzemelerine kadar hayatın her alanında en yaygın olarak kullanılan malzeme ürünlerinden biridir. Bununla birlikte, bilinen eski malzemelerden biri olmakla beraber, metalurji ve malzeme bilimindeki gelişmelere bağlı olarak yüzyıllardır kendi özelliklerini geliştirmektedir. Çelik her zaman için üstün özellikler gösteren malzeme keşiflerinin merkezinde bulunmuştur. Çelik ailesi kompozisyon, ısı-ışılma ve üretim özelliklerinin gelişmesi ile her geçen gün daha da büyümektedir.

CN3MN, süperöstenitli paslanmaz çelikler, üstün korozyon dirençleri ile östenitik paslanmaz çelik ailesinin bir alt grubunu oluşturmaktadır. Uygulama alanları genel olarak, diğer paslanmaz çelik alaşımlarının korozyona uğrayacağı deniz ve deniz altı yapıları ve petrol kuyuları gibi hem mekanik özelliklerin hem de korozyon dayancınının çok iyi olması gereken uygulamaları kapsamaktadır. Ancak, öncesinde bu alışımda çözülmesi gereken ciddi bir sorun vardır. Bu alaşımlar, 15 dakika gibi kısa süreli ısı işlemlere maruz kaldığı zaman tokluk dayancını yarı yarıya kaybetmekte ve gevrek kırılma karakteristiği göstermektedir. Dövme çelik alaşımlar genellikle küçük boyutlarda oldukları için bu tür kırılma davranışı göstermemektedirler. Buna karşın dökümle üretilen süperöstenitik paslanmaz çeliklerde, soğuma hızı çok yavaş ve homojen olmadığı için bazı bölgelerde bu kırılma türüne rastlanılmaktadır. Bu sebeple,

kırılma mekanizmaları çok iyi anlaşılabilir bu şekilde kırılmayı önleyecek tedbirler alınmalıdır.

Bu çalışmanın amacı, 927°C de 30 saniye ile 16 dakika arasındaki kısa süreli, uygulanan ısı işlemlerinden sonra gözlemlenen gevrekleşme mekanizmalarının belirlenmesidir. Bunun için, öncelikle, ısı işlem gören numuneler sadece homojenize edilen numuneler ile mikroyapısal olarak taramalı elektron mikroskobu ile karşılaştırılmışlardır. Bu kıyaslamalardan çıkan sonuçlardan, kırılmanın tane sınırları boyunca oluşan çökeltiler olabileceği düşünülmüştür. Bu çökeltiler daha önce literatürde sıklıkla incelenen ikincil fazlardan (Laves, sigma, chi) farklı oldukları tespit edilmiştir. Metallerarası bileşikler genel olarak gevrek davranış gösterdiklerinden dolayı, tane sınırlarında çekirdeklenip büyüdükleri zaman malzemenin dayancını düşürürler. Gerçekleştirilen analizlere göre, 30 saniye ısı işlem görmüş numunedeki çökelti büyüklüğü ortalama 400 nm ve birim alandaki çökelti sayısı çok yüksektir. Önceki çalışmalarda bu çökeltilerin oluşma kinetiklerinin çok yavaş olduğunun belirlenmesine rağmen, bu çalışmada tespit edilen çökeltilerin hızlı kinetiklere sahip olmasının sebebi numunenin alaşım elementleri açısından homojen olmamasıdır. Özellikle molibdenum numune boyunca homojen olarak dağılmamış ve bu elementce zengin olan bölgeler çökeltiler için tetikleyici olarak davranmıştır.

Gözlemlenen ikinci mekanizma kristalografik hatalar sonucu oluşan tane içi gevrekleşmedir. Isıl işlem görmüş numunelerde zigzag şeklinde çatlaklar belirlenmiştir. Bu çatlakların HRTEM ile incelenmeleri sonucunda o bölgelerde nano boyutlarda dizilim hatalarına rastlanılmıştır. Bu hataların oluşma sebebinin alaşımın sahip olduğu düşük dizilim hatası enerjisi olduğu tespit edilmiştir. CN3MN için dizilim hatası enerjisi 12-30 mJ/m² olarak hesaplanmıştır. Ayrıca, birbiriyle iç içe geçmiş dislokasyon dağılımı da bu malzemedeki dizilim hatası enerjisinin düşük olduğunu desteklemektedir. Dizilim hata enerjisinin düşük olması FCC yapı içerisinde kayma sistem sayısı sınırlı kırılğan HCP dizilimlerin oluşmasına yol açmaktadır. Bu sebeple kırılmanın büyük bir bölümü, HCP dizilim boyunca tane içinde gerçekleşmektedir.

Anahtar kelimeler: Paslanmaz çelik, CN3MN, Elektron mikroskobu, Kristal hataları, Metallerarası bileşikler

To My Precious Family...

ACKNOWLEDGEMENT

This work is financially supported by BAP 2014-007-214-1. I would like to thank Prof. Scott.L Chumbley for providing the samples and sharing invaluable experience and information with us throughout the study. Also, I must appreciate the Dr. Michael Feuerbacher in The Ernst Ruska-Centre (ER-C) for Microscopy and Spectroscopy with Electrons for conducting in-situ TEM experiments.

I would never have been able to finish my thesis without the guidance of Assoc. Prof. Yunus Eren Kalay and I would like to express my deepest gratitude to him, for his excellent guidance and providing me with an excellent atmosphere for doing research. I am sure that I will be always appreciated to his dignified contributions in both academic and job career.

I count myself very lucky to get acquainted with Serkan Yılmaz for his precious supports and share information about microscopes whenever I need. Besides, his contributions are not limited with the academic life, he was always a good friend who I knocked his door when I needed a different perspective about things happened in my life. I want to represent my special thanks to my lab mates Özgün Acar, Mustafacan Kutsal, Can Yıldırım, Ayşe Merve Genç Ünalın, Fatih Sıkan, Mert Övün, Bengisu Yaşar, Eyüp Can Demir, Anıl Kantarcıoğlu, Tuba Demirtaş and Şermin Özlem Turhan who provide very peaceful studying atmosphere during working hours and very funny times all the time. I also would like to thank Simge Tülbez, Berk Doğu, Yelda Meyva, Sena Okay, Lütfi Ağartan, Mehmet Hazar Şeren, Doğanca Sarı, Ezgi Onur, Yedigâr Seymen and Burçin Kaygusuz for their invaluable friendship. Finally, I want to give my special thanks to my dear love. Everything has been changing in a positive manner after she entered my life. Finally, I am thoroughly appreciated to my parents and my pretty sister for their great love, patience, trust and contributions since I was born. It is really nice to know they are always with me.

TABLE OF CONTENTS

ABSTRACT.....	v
ÖZ	vii
ACKNOWLEDGEMENT	x
TABLE OF CONTENTS	xi
LIST OF TABLES	xiii
LIST OF FIGURES	xiv
NOMENCLATURE.....	xviii
CHAPTERS	
1. INTRODUCTION	1
2. LITERATURE REVIEW.....	5
2.1. Stainless Steels	5
2.1.1. An Introduction to Stainless Steels	5
2.1.2. Thermodynamics of Stainless Steels.....	6
2.1.3. Classification of Stainless Steels.....	8
2.1.4. Properties of CN3MN	17
2.2. Formation of Intermetallics.....	18
2.2.1. Common Types of Intermetallics in Austenitic Stainless Steels	18
2.2.2 Effects of Precipitates on the Mechanical Properties.....	24
2.3. Crystallographic Defects in Steel.....	24
2.3.1. Dislocations.....	24
2.3.2 Stacking Faults	29
2.3.3 Twins.....	31
3. EXPERIMENTAL PROCEDURE	33
3.1. Production and Heat-Treatments of the Samples.....	33
3.2. Mechanical Analyses	34

3.3. Structural Analyses	35
3.4. Microstructural Analyses	35
3.4.1. Metallographic Sample Preparation	35
3.4.2. Optical Microscope Analyses.....	35
3.4.3. SEM Analyses	35
3.4.4. EBSD Analyses	36
3.4.5. TEM Analyses.....	37
4. RESULTS AND DISCUSSION	41
4.1 Stages of Embrittlement	41
4.2 Intergranular Embrittlement	44
4.2.1 Microstructures.....	44
4.2.2 Structural Analyses of Precipitates	48
4.2.3 Origin of the Precipitates.....	52
4.3 Transgranular Embrittlement	57
4.3.1 White-Bands.....	60
4.3.2 Stacking-Faults.....	65
5. CONCLUSION & FUTURE RECOMMENDATIONS	77
5.1. Conclusions	77
5.2. Future Recommendations.....	78
REFERENCES.....	82
APPENDICES.....	88

LIST OF TABLES

TABLES

Table 2.1	Examples of martensitic stainless steels and compositions [13].....	12
Table 2.2	The compositions of selected austenitic stainless steels [11].....	15
Table 2.3	Chemical composition range of CN3MN [21].....	18
Table 2.4	Common precipitates observed in austenitic stainless steels [22-30].	19
Table 2.5	Comparison of edge and screw dislocations [43].....	26
Table 2.6	Stacking fault energies of various alloy systems [43].....	31
Table 2.7	Twin systems in different cubic systems [43].....	32
Table 3.1	The annealing durations and the given specimen codes for CN3MN.....	34
Table 4.1	List of interplanar spacing calculated from SADP at various zone axis...49	
Table 4.2	The composition defined by ASTM Standards and the results of the EDS measurements collected from the regions shown in Figure 4.9(b).	50
Table 4.3	EDS measurements of precipitates.....	56
Table 4.4	Average grain sizes for selected specimens.	59
Table 4.5	EDS measurements from the regions shown in Figure 4.24 (wt%).	64
Table 4.6	SFE (mJ/cm^2) of CN3MN formulas based on chemistry.....	73
Table 4.7	Parameters used in the SFE calculations.....	74
Table 4.8	Mechanical properties used in calculations of SFE [1,68].....	75

LIST OF FIGURES

FIGURES

Figure 1.1 Graph showing the world steel consumption between 1970 and 2012. The inset table summarizes the total steel production of various countries in 2011 and	1
Figure 2.1 Classification of iron-alloy phase diagrams.....	6
Figure 2.2 Schaeffler Diagram	7
Figure 2.3 (a) The corrosion rate of steels with different chromium concentrations at room temperature (b) weight losses in the given experimental conditions for steels with different chromium concentrations [6,7].....	8
Figure 2.4 Fe-Cr Phase Diagram [10].	9
Figure 2.5 Fe-Cr phase diagrams with (a) 0.05 wt. % C and (b) 0.1 wt. % C [11]...	10
Figure 2.6 The evolution diagram of ferritic stainless steels [12].....	11
Figure 2.7 IT diagrams of (a) AISI 430 ferritic stainless steel austenitized at 1090°C (b) AISI 410 martensitic stainless steel austenitized at 980°C [15].....	12
Figure 2.8 Family of martensitic stainless steel grades [12].	13
Figure 2.9 Fe-Cr-Ni phase diagram at 1100°C and various austenitic stainless steel compositions implemented on the diagram [10].	14
Figure 2.10 Family of austenitic stainless steels [12].	16
Figure 2.11 Examples for the microstructures of (a) duplex stainless steel [18] and (b) precipitation-hardened stainless steel [19].	17
Figure 2.12 (a) BF TEM image of intergranular sigma particle (2000h, 750°C), Diffraction patterns along (b) [001], (c) 111 and (d) [011] zone axes [36, 37].....	20
Figure 2.13 (a) DF image of intergranular Laves particle (240 hours, 950°C) (b) BF image of transgranular Laves particle along with defects parallel to each other (c) BF image a fault-free Laves phase (d) SADP from the particle in (c).....	21
Figure 2.14 Number and volume densities of precipitates from annealed samples.	22
Figure 2.15 Microstructures of the samples exposed to heat-treatments at 800°C for (a) 1 hour, (b) 4 hours, (c) 12 hours, (d) 48 hours [40].	23

Figure 2.16 (a) BSE image of 30-min-annealed sample at 872°C (b) Impact strength as a function of time-at-temperature for an 872°C heat-treatment [39].	24
Figure 2.17 Geometrical representations of edge and screw dislocations [43].	25
Figure 2.18 Schematic drawing of Cross-Slip [43].	26
Figure 2.19 Schematic drawings of (a) perfect and (b) partial dislocations [44].	27
Figure 2.20 Schematic drawings of (a) Shockley and (b) Frank partials with intrinsic stacking fault [44].	28
Figure 2.21 (a) Ladder-like structure developed within a twin of an austenitic grain (b) interaction of slip band with a high angle grain boundary [45].	28
Figure 2.22 (a) Straight sessile dislocations parallel to the [110] direction (b) Dissociated Shockley Partial [46].	29
Figure 2.23 Schematic drawings of (a) fcc stacking sequence, (b) Intrinsic Stacking fault with hcp region, (c) Extrinsic stacking fault, (d) hcp stacking [43].	30
Figure 2.24 Schematic view of twinning from an fcc crystal [52].	32
Figure 3.1 The chosen samples after (a) Impact tests (b) Hardness tests	34
Figure 3.2 Detector positions inside the chamber.	36
Figure 3.3 Shows the raw EBSD data collected (a) before and (b) after the background removal. Kikuchi lines are clearly seen after the correction.	37
Figure 3.4 Flowchart of TEM specimen preparation.	38
Figure 3.5 Examples for (a) BF imaging (b) DF imaging (c) SADP and (d) HRTEM imaging captured from the same region.	39
Figure 4.1 Hardness and impact toughness with respect to annealing time.	41
Figure 4.2 Fracture surfaces of (a) S0 and (b) S0.5.	42
Figure 4.3 Fracture surfaces of (a) S2 and (b) S4.	43
Figure 4.4 Fracture surfaces of (a) S8 and (b) S16.	43
Figure 4.5 Deeply etched specimens representing the (a), (b) S0 and (c), (d) S0.5.	45
Figure 4.6 Deeply etched specimens representing the (a), (b) S2 and (c), (d) S4.	46
Figure 4.7 Deeply etched specimens representing the (a), (b) S8 and (c), (d) S16.	47
Figure 4.8 SEM image of S16 embedded with an EBSD map.	47
Figure 4.9 (a) BF image representing the grain boundary precipitation observed in S16. (b) Closer look to a single precipitate observed in (a). Insets show the SADP.	48
Figure 4.10 HRTEM image showing the interface between the austenite grain and the precipitate in S16 specimen. The inset shows the FFT of the dashed region.	51
Figure 4.11 Dendrite-like macrostructures from (a) S0 and (b) S0.5.	52

Figure 4.12 (a) Dendrite-like macrostructure from S0.5 and (b) EBSD pattern of the area defined by dashed lines in (a).	53
Figure 4.13 (a) The region selected for the EDS line Analysis from the specimen S0.5 (b) Linear compositional change across the line shown in (a).	54
Figure 4.14 BSE images from the specimens (a) S1h (b) S4h (c) S16h (d) S16h showing the distribution of the precipitates.	56
Figure 4.15 (a) The change of percent area and precipitate size with the annealing time (b) Number of precipitates per $2500\mu\text{m}^2$ with different annealing times.	57
Figure 4.16 Intergranular cracks in (a) S8 (b) S16 and transgranular cracks in (c) S8 and (d) S16.	58
Figure 4.17 Optical microscope analyses for grain size measurement from (a) an equiaxed grain in S0 (b) an oriented grain in S0 (c) an equiaxed grain in S4 (d) an oriented grain in S16.	59
Figure 4.18 XRD patterns of S0 and S16.	60
Figure 4.19 (a) BF showing a crack and a white-band just next to each other (b), (c) BF of the white-band at higher magnification, (d) SADP showing the orientation of the white-bands.	61
Figure 4.20 HRTEM image at the tip of the crack in S0. The insets on the right hand side represent the FFT patterns collected from the regions shown in HRTEM.	62
Figure 4.21 BF images showing the alternating layers of white-band and austenite matrix. The EDS measurements were conducted from the labeled layers.	63
Figure 4.22 BF images of disappearing white-bands during in-situ heating.	65
Figure 4.23 Montages BF images of zigzag cracks observed in S0.5.	66
Figure 4.24 (a), (b) The zigzag cracks in S0.5 at lower magnification from TEM and SEM, respectively. (c), (d) same zigzag cracks at higher magnification from TEM and SEM, respectively.	67
Figure 4.25 (a) and (b) Zigzag patterns observed far from the very thin regions.	67
Figure 4.26 Stacking sequences of, (a) perfect lattice and, (b) intrinsic stacking fault and (c) extrinsic stacking fault [62].	68
Figure 4.27 The faulted region in S0.5 investigated through (a) BF, (b) SAEDP, (c), (d) and (e) HRTEM imaging.	70
Figure 4.28 BF image of S0.5 consisted of Shockley partial dislocations.	71
Figure 4.29 BF images of aligned dislocations from (a) S0.5 and (b) S8.	72

Figure 4.30 (a) The geometry of the dislocation nodes (b) Example of node diameter calculation from S0.5 [65].....	74
Figure 4.31 (a) and (b) show the dislocation distribution in S16.....	75
Figure 4.32 Dislocations observed in (a) S8 (b), (c) S16.....	76
Figure 5.1 Precipitate-free from S0 and precipitate-rich zones from S8.	80
Figure 5.2 (a) Pore filled with precipitates and (b) EDS line analysis.	81

NOMENCLATURE

BF	:Bright-Field
CBED	:Convergent Beam Electron Diffraction
DF	:Dark-Field
EBSD	:Electron Back Scattered Diffraction
EDS	:Energy Dispersive Spectroscopy
FFT	:Fast Fourier Transform
HRTEM	:High Resolution Transmission Electron Microscopy
PREN	:Pitting Resistance Equivalent Number
SADP	:Selected Area Diffraction Pattern
SEI	:Secondary Electron Imaging
SEM	:Scanning Electron Microscope
SFE	:Stacking Fault Energy
SFP	:Stacking Fault Probability
SSS	:Superaustenitic Stainless Steel
TEM	:Transmission Electron Microscope
TWIP	:Twinning Induced Plasticity
XRD	:X-Ray Diffraction
σ	:Sigma Phase
χ	:Chi Phase
K₁	: M ₂₃ C ₆ Carbide
K₂	: M ₇ C ₃

CHAPTER 1

INTRODUCTION

The main role of a metallurgical and materials engineer is to tailor the material properties in order to get best performance for a specific engineering application. In addition to performance related properties, the selected engineering material is expected to exist in bulk quantities with reasonable production costs. Steel, which can be simply named as iron–carbon alloy with considerable amount of some other alloying elements, satisfies these conditions better than any other engineering materials. The main constitute of steel, iron, is one of the most abundant element in Earth’s crust. This makes the cost of steel alloys being reasonable as compared to other alloy systems. Additional alloying elements, heat-treatment procedures and shaping processes may provide cutting edge properties to the steels. Consequently, steel has been accepted to be the most important engineering material for centuries [1].

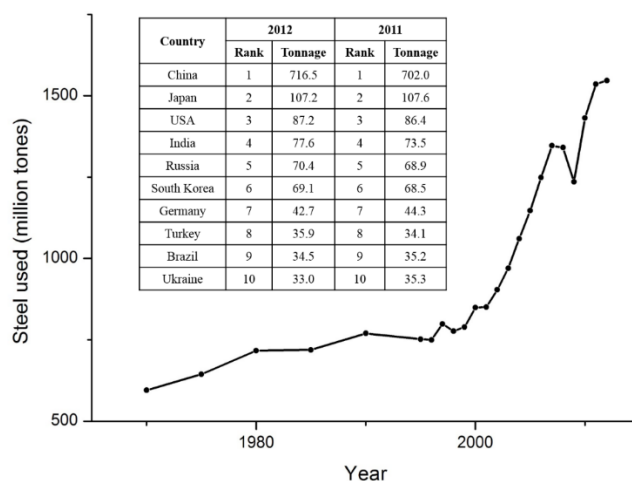


Figure 1.1 Graph showing the world steel consumption between 1970 and 2012. The table summarizes the total steel production of various countries in 2011 and 2012.

The world steel consumption can be seen in Figure 1.1. The sharp increase in steel consumption after early 2000s reveals that despite the progression in the smart and nano materials technology, steels keep their unique importance. The inset table in Figure 1.1 lists the total steel production of various countries in decreasing order. The top steel producer countries are China Japan and USA. Turkey has ranked as 8th on this list.

Primarily attributed to its broad and easy manageable properties, steel products have a very extensive area of applications. One can come across a steel product from submarine constructions to the skyscraper trusses or from kitchen appliances to cutting tools. Surely, the motivation of using these products may completely differ from each other. For instance, the main intention of using steel as a cutting tool is the hardness; on the other hand corrosion resistance is the motivation of using steel in salty water.

One major drawback of all steels used in various applications is *rusting*, the formation of iron hydroxide ($\text{Fe}(\text{OH})_3$) layer on the surface, when they are exposed to a corrosive environment like vapor or liquid solutions. This problem was partially solved by the invention of stainless steels for which 10.5% Cr element was added as an alloying element. This additional Cr results in a formation of very thin and coherent layer of stable chromium oxide, which hinders the contact between the steel and the corrosive environment. Stainless steels can be divided into 3 groups with respect to the stable matrix phase formed at room temperature. These are namely as ferritic stainless steels, martensitic stainless steels and austenitic stainless steels. There are also duplex stainless steels, a subclass of stainless steels which contain both ferrite and austenite as stable phase. Ferritic stainless steels are mainly low alloyed and low carbon stainless steels which have good ductility and formability. They are the cheapest stainless steel subgroup and mainly used for low quality kitchen appliances and exhaust systems. Martensitic stainless steels contain extra carbon to facilitate the martensitic phase transformation. They are usually chosen for their good hardness and wear resistance combined with high strength. Austenitic stainless steels contain nickel to stabilize austenite at room temperature. They are mainly used for high quality kitchen wares, piping systems and seawater applications. Although they are more expensive to produce, they exhibit the best corrosion resistance performance with respect to other steel type counterparts. Detailed information about the stainless steels can be found in the third chapter.

CN3MN Grade Super Austenitic Stainless Steel (SSS), which belongs to austenitic stainless steel class, is a special kind of high alloyed steel, used for mainly seawater and piping systems due to their exceptional corrosion resistance with good mechanical performance for both low and high temperature applications. As similar to other high alloyed steels, problem arises because of the precipitates formed along grain boundaries. The precipitates may cause to form a brittle network on the grain boundaries and results in embrittlement through an intergranular fracture mechanism. The mechanism of this embrittlement has been examined by many studies and different kind of precipitates has been characterized in details. On the hand, the fracture mechanisms where the precipitation is limited and the failure is mainly controlled by transgranular fracture, has not been clearly understood. It definitely requires further attention and detailed examination.

In this respect, the main purpose of this study is to investigate the failure mechanism for a CN3MN grade SSS upon short-term heat-treatment procedures. The relatively short annealing durations result in a formation of precipitates along the grain boundaries. Therefore, the main embrittlement is driven via transgranular fracture mechanism Homogenized and heat-treated samples, with different annealing times changing from 0 minute to 16 hours, were subjected to a detailed microstructural and structural characterization. The thesis plan is given as;

- In the *introduction* chapter, the background information about the scope of the study was stated and the outline of the thesis was presented,
- In the *literature review* chapter, after a brief introduction to the stainless steels, related studies based on intergranular and transgranular fractures of steels were summarized,
- In the *experimental procedures* chapter, the production technique of CN3MN and the characterization methods were stated,
- In the *results and discussion* chapter, the results of the experiments were explained and key points were discussed in terms of microstructural and crystallographic point of view,
- In the *conclusion and future recommendations* chapter, the conclusions of the study was derived and recommendations for future studies were given.

CHAPTER 2

LITERATURE REVIEW

2.1. Stainless Steels

2.1.1. An Introduction to Stainless Steels

As previously mentioned in the introduction chapter, the protection mechanism of stainless steels against rusting is the formation a protective chromium oxide layer on top of the surface. For this purpose, at least 10.5% Cr must be added as an alloying element to the steel. Other than Cr, other elements are added to stainless steels for various purposes. Therefore at this point, it may be useful to briefly explain the effects of the alloying elements added to the stainless steels.

Carbon, like in the other type of steels, increases hardness and hardenability in expense of toughness, formability and weldability. Mn addition promotes the shock resistance of steel. Also, it provides extra strength and hardenability to the steel. Moreover, Mn is a strong austenite stabilizer, which decreases the eutectoid temperature even at room temperature. Almost all steels contain Si because they are used for deoxidizing agent during steel production. They are also often added to stainless steels to get finer grain size. Si is also an austenite former agent and it triggers the austenite nucleation which suppresses the extensive growth of the grains. Cr is the main element which makes the steel “stainless”. Also, it is a strong carbide and nitride former, which hinders the dislocation motion in the steel, leading to loss of toughness and ductility, but increases the hardness. Ni is the most commonly used austenite former element. Almost all austenitic stainless steels contain Ni. Mo is also a strong carbide former element. Also, it hinders the high temperature embrittlement, therefore it is commonly used in high-

speed tool steels. Zr, Ti, Nb and Ta are even stronger carbide formers than Cr due to their higher carbon affinity, therefore there are used in stainless steels to prevent sensitization [3].

Up to here, the roles of alloying elements have been investigated mainly in terms of their contributions in mechanical and deteriorative performance. However, the effects of alloying elements are not limited with performance related properties, they also depict the possible stable and metastable phases present in the steel. In this respect, the thermodynamic background behind the stainless steels will be investigated in the next section.

2.1.2. Thermodynamics of Stainless Steels

The complete understanding of an effect of the alloying element would be impossible without an investigation through possible phase diagrams in a very wide range of temperature. The effect of alloying elements are classified into four groups regarding to the Fe-C phase diagram; namely as, open γ -field, closed γ -field, expanded γ -field and contracted γ -field, as-shown in Figure 2.1. The alloying elements which expand the γ -loop are known as austenite stabilizers, the ones which contracts γ -loop are known as ferrite stabilizers [4].

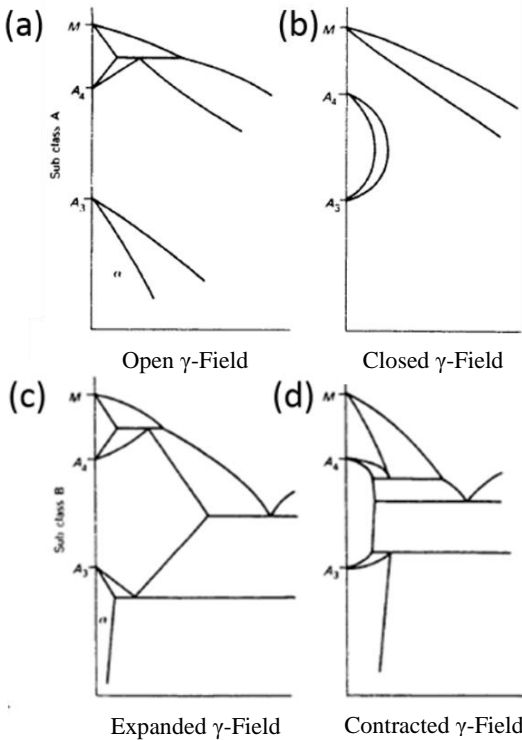


Figure 2.1 Classification of iron-alloy phase diagrams

However, things can be more complicated when the overall effects of alloying elements are taken into account. One practical way to determine what phase is present at room temperature in the case of multiple alloying elements are present, is to consult Schaeffler Diagrams. They represent the stable phases observed on the stainless steels by dividing the alloying elements into either ferrite or austenite stabilizers, and their amounts were used for the calculation of Cr-equivalent and Ni-equivalent numbers with the empirical formula below. They are x and y axes, respectively, on the diagram and the regions represent the stable phases at room temperature [5].

$$\text{Cr eq.} = (\text{Cr}) + 2(\text{Si}) + 1.5(\text{Mo}) + 5(\text{V}) + 5.5(\text{Al}) + 1.75(\text{Nb}) + 1.5(\text{Ti}) + 0.75(\text{W}) \quad (\text{Eq.2.1})$$

$$\text{Ni eq.} = (\text{Ni}) + (\text{Co}) + 0.5(\text{Mn}) + 0.3(\text{Cu}) + 25(\text{N}) + 30(\text{C}) \quad [5] \quad (\text{Eq.2.2})$$

where the compositions must be substituted in weight percentages. Another example of Schaeffler Diagram is given in Figure 2.2. Each region in this diagram show the predominance phases at room temperature. It should be noted that for a given Cr. eq number, as the Ni.eq number increase, the matrix phase has an increasing tendency to form austenite, or vice versa.

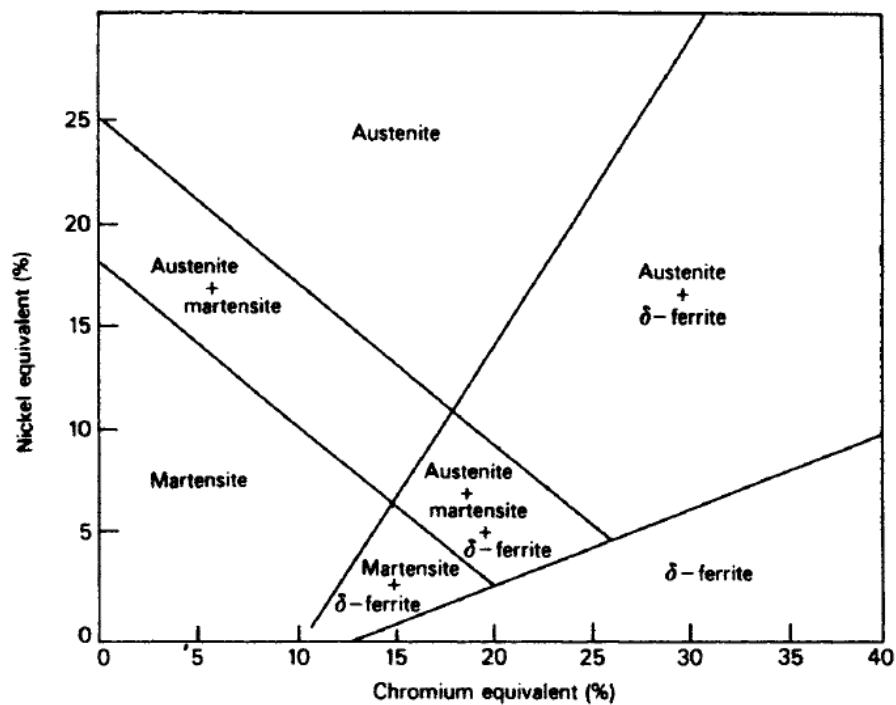


Figure 2.2 Schaeffler Diagram [5].

2.1.3. Classification of Stainless Steels

The resistance to corrosion strongly depends on the composition of the stainless steels. Figure 2.3 illustrates this situation clearly. In the Figure 2.3 (a), the behaviors of steels against sulfuric acid and nitric acid with different amount of Cr are shown. As the amount of Cr increases, the resistance to the corrosion against two different chemicals is also increased. Therefore it can be estimated that the steel grades with higher Cr content are more resistant to corrosion. This is also valid for high temperature conditions, as shown in Figure 2.3 (b). Another important point that can be inferred from Figure 2.3 (a) is that the effectiveness of stainless steels against different chemicals is completely different. For instance, for a high Cr ferritic stainless steel (~20 wt% Cr) the corrosion rate against dilute sulfuric acid is in the order of 10^5 , whereas the one against dilute nitric acid is only 500 mg/dm²-day. Hence, that steel grade should not be used in environments containing sulfuric acid, however, it can be safely used against nitric acid [6].

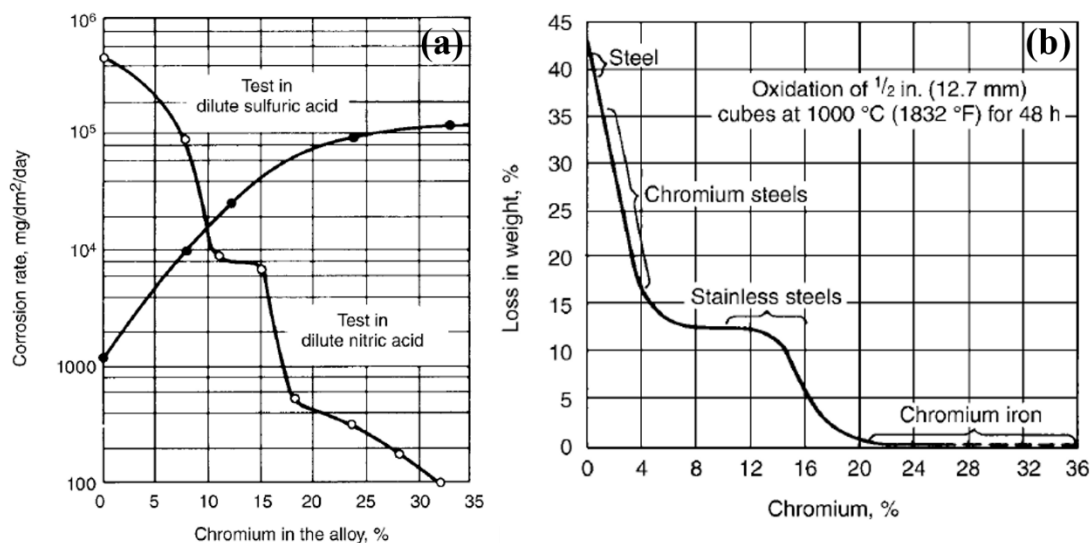


Figure 2.3 (a) The corrosion rate of steels with different chromium concentrations at room temperature (b) weight losses in the given experimental conditions for steels with different chromium concentrations [6,7].

In some other studies, it has been revealed that austenitic and duplex stainless steels exhibit good performances in sulfuric acid and they have been widely used in industry [8,9]. This seems to be contradicting with the previous example (Fig 2.3) but it actually shows the importance of matrix phase determining the deteriorative properties. Therefore, it is crucial to determine the corrosion resistance of stainless steels. Below,

ferritic, martensitic and austenitic stainless steels are investigated separately. The combined microstructure effects such as the duplex and precipitation-hardened stainless steels were also cited.

2.1.3.1 Ferritic Stainless Steels

As the name suggests, ferritic stainless steels have ferrite as their matrix phase. These steels can be thought as chromium and iron alloys in order to simplify the phase relationships. Below, Fe-Cr phase diagram is given representing the 400°C and 1800°C temperature range. At the top of the diagram, one can see the melting points of pure Fe and Cr. Also, there are solid and dashed lines, which show the liquidus and solidus, respectively. The large region in the middle part is labeled as alpha because the alloys within this composition range are all ferrite.

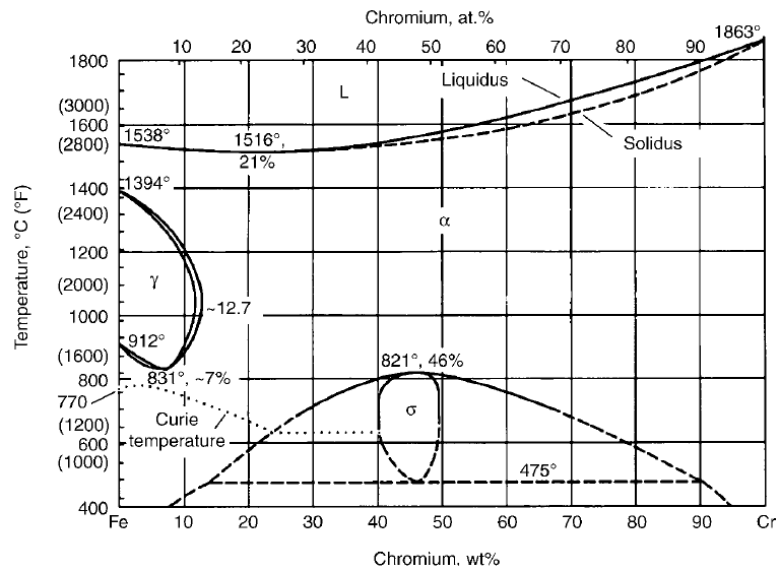


Figure 2.4 Fe-Cr Phase Diagram [10].

The looped region at the middle left shows austenite phase. Cr can stabilize the austenite phase at higher temperatures. The stability region is smaller than that of conventional Fe-C phase diagram due to the fact that Cr is a ferrite stabilizer. The sigma (σ) phase observed at the bottom, has a different crystal structure as compared to bcc-ferrite. The formation of sigma (σ) phase is highly unwanted. Its extensive brittleness deteriorates the mechanical properties. Therefore it must be strictly avoided in stainless steels. It should be noted that the phase boundary lines that bounds sigma phase are dashed. This means that the corresponding phase will not appear unless the alloy is kept at that temperature for very long or apply very slow cooling rates.

Although it is assumed that the system is consisted of only Fe and Cr, it is impossible to produce the steel without carbon. Even very small additions of C have significant effects on the phase diagrams. Therefore, it is more significant to investigate Fe-Cr-C ternary systems as compared to Fe-Cr binary systems. In the literature, Fe-Cr binary phase diagrams with fixed carbon content are more common. Figure 2.5 shows an example for such diagrams for 0.05 and 0.1 wt% C.

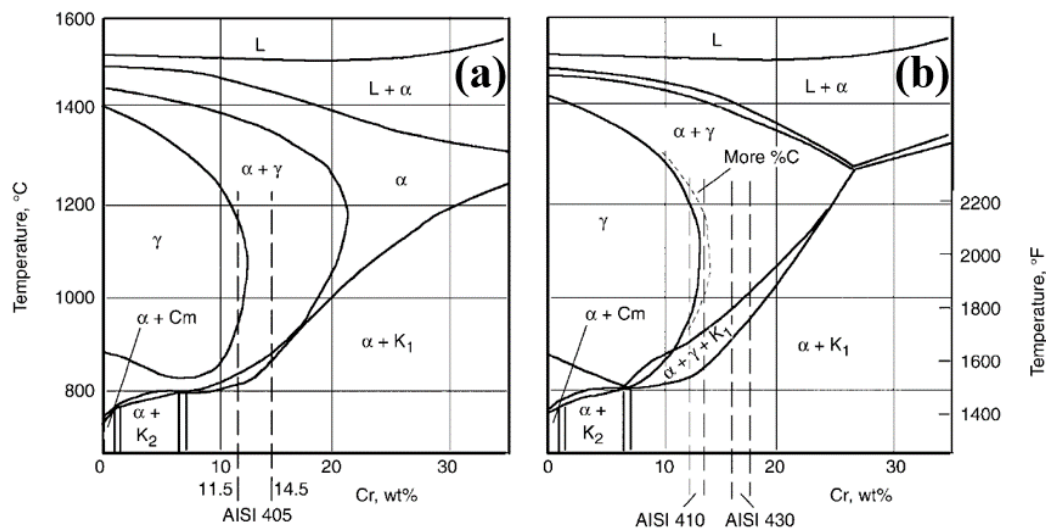


Figure 2.5 Fe-Cr phase diagrams with (a) 0.05 wt. % C and (b) 0.1 wt. % C [11].

There are two significant changes after small additions of C. The first one is the increase in austenite area. In the Fe-Cr phase diagram with 0.05 wt% C, austenite cannot form higher than 12.7% Cr at 1000°C, whereas after the addition of only 0.05%, this limit has been pushed to 20% Cr. The second important effect is the formation of carbides. Cr is a very strong carbide element (even stronger than iron carbide (cementite)). Many different type of carbide may be formed with different crystal structures than cementite. The most commonly observed carbides are denoted as K_1 and K_2 , which are called as $M_{23}C_6$ and M_7C_3 respectively [11].

The most widely used ferritic stainless steel grade is AISI 430 due to its formability and reasonable production cost. Some other grades have been evolved from AISI 430 for specific purposes. The evolution of ferritic stainless steels is summarized in Figure 2.6.

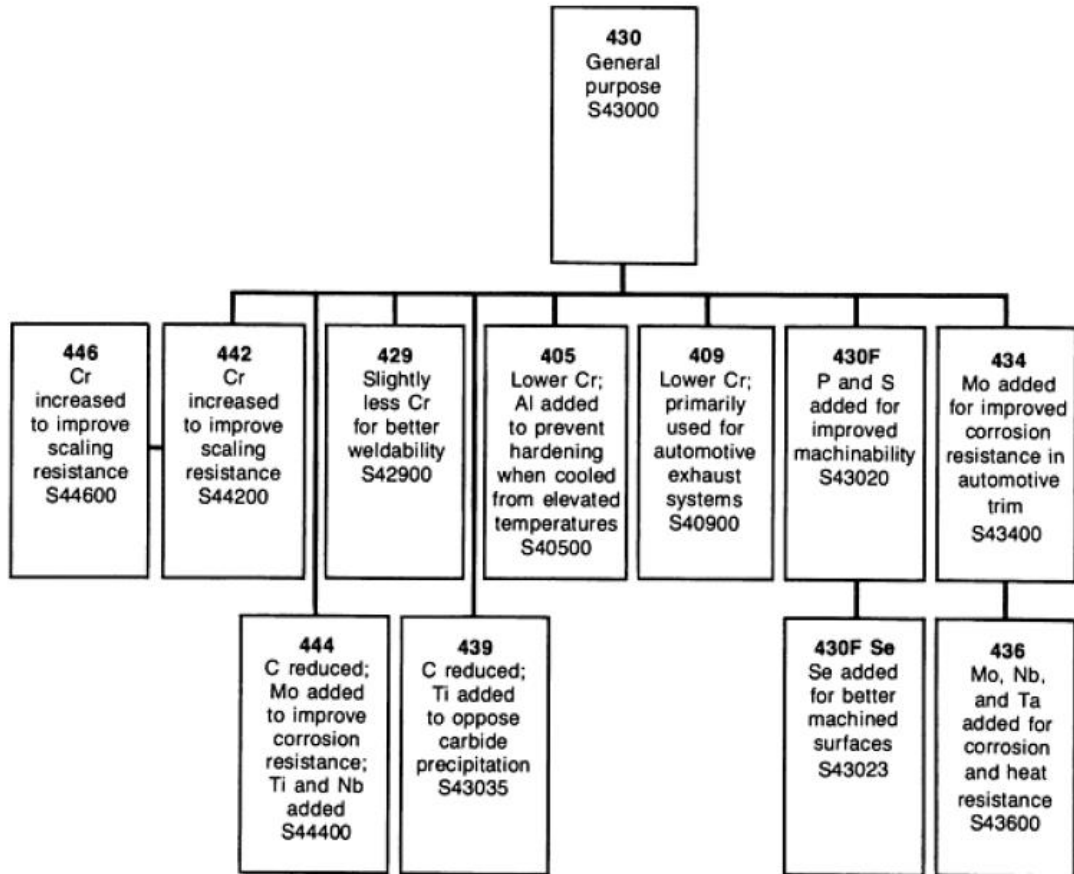


Figure 2.6 The evolution diagram of ferritic stainless steels [12].

2.1.3.2 Martensitic Stainless Steels

Martensitic stainless steels are the subgroup of stainless steels which contains mainly chromium and carbon as alloying elements. They have distorted bcc structure and exhibit ferromagnetic properties. Their resistance to corrosion protects only for the mild environments as compared to other stainless steel counterparts. Some martensitic stainless steels and their compositions can be seen in Table 2.1 [13]. It should be noted that all martensitic steels belong to 4xx family of stainless steels.

As the name suggests, these steels require heat-treatments to form martensite instead of ferrite at room temperature. The heat-treatments are almost the same as the plain carbon steels with additional constraints. For instance, K_1 and K_2 carbides dissolve more slowly than cementite, therefore longer austenitization duration may be required

to dispose the second phases. Secondly, thermal conductivity is much lower, therefore quenching must be applied in multiple steps [14].

Table 2.1 Examples of martensitic stainless steels and compositions [13].

AISI No.	%C	%Cr	Other (§)
410	0.15	11.5-13	-
431	0.20	15-17	1.25-2.5Ni
440A	0.65-0.75	16-18	0.75 Mo
440B	0.75-0.95	16-18	0.75 Mo
440C	0.95-1.2	16-18	0.75 Mo

§ All grades contain 1%Si and 1%Mn

The hardenability of stainless steels strongly depends on the chromium content [15]. As the Cr increases, the IT (isothermal transformation) curves are shifted towards right-hand side. This fact is illustrated in Figure 2.7. It should be noted that the nose temperature of pearlite starts at 60 seconds for ferritic stainless steel; whereas it is at 500 seconds for martensitic stainless steel. For this reason, slow cooling rates i.e. air cooling may be sufficient to obtain fully martensitic structure. However, in practice oil quenching is preferred because excess slow cooling may cause carbide precipitation, which deteriorates both the mechanical properties and the corrosion resistance [15].

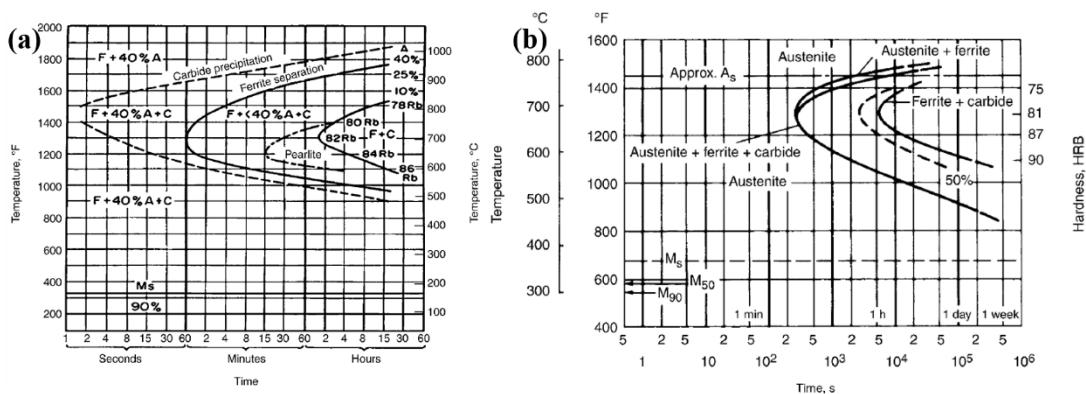


Figure 2.7 IT diagrams of (a) AISI 430 ferritic stainless steel austenitized at 1090°C
(b) AISI 410 martensitic stainless steel austenitized at 980°C [15].

The corrosion resistance of martensitic stainless steel is lower as compared to other stainless steel groups. The main reason is the presence of high amount of carbon needed to form martensite. As the amount of carbon increases, the possibility of carbide formation is enhanced. This results in formation of Cr rich precipitates. In other words, chromium atoms will be depleted from the matrix. If this depletion leads to a decrease more than 12% Cr from the matrix, these areas are prone to corrosion. This phenomenon is called as *sensitization*. Since these carbides are preferentially nucleated at grain boundaries, sensitization may be thought as the primary reason of intergranular corrosion [16].

Martensitic stainless steels are used for cutlery applications. The most common grade of martensitic stainless steels is AISI 410 and the other grades are evolved from this grade to enhance other specific properties. In Figure 2.8, the martensitic stainless steel family is summarized.

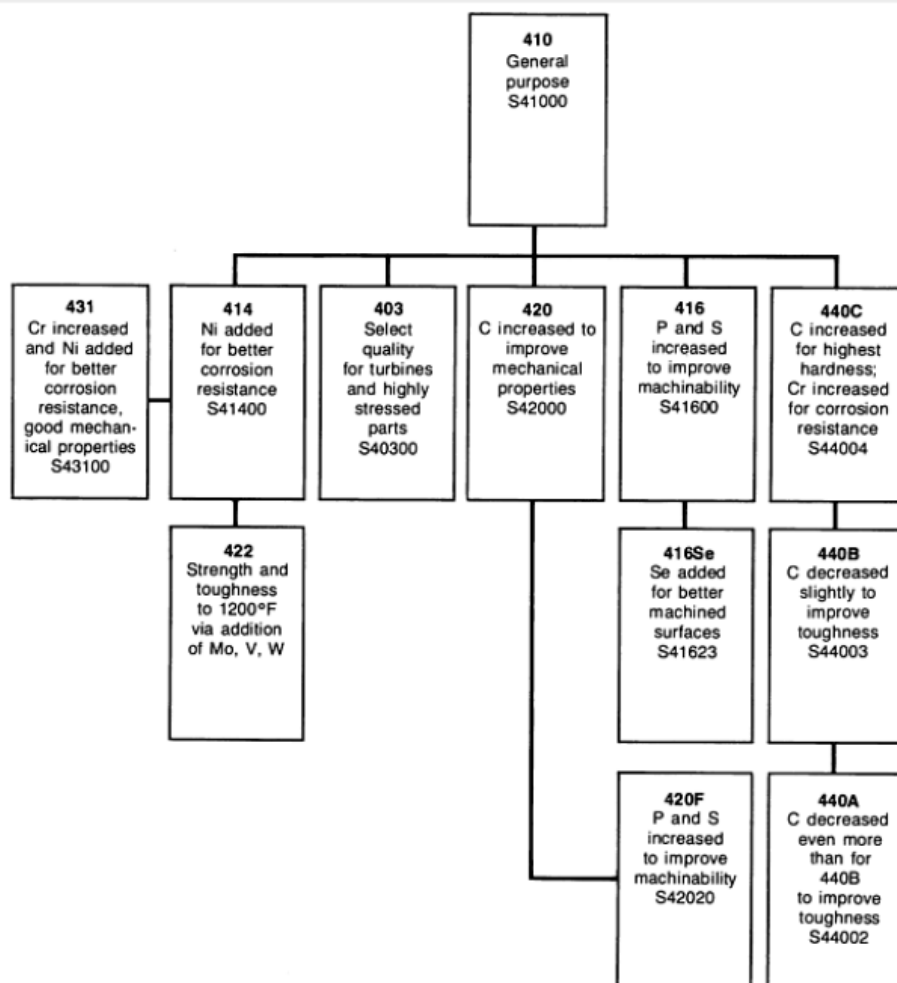


Figure 2.8 Family of martensitic stainless steel grades [12].

2.1.3.3 Austenitic Stainless Steels

Although austenite is stable at high temperatures in plain carbon steels, austenitic stainless steels contain austenite as matrix phase at room temperatures by the additions of large amounts of Ni. Both Ni and austenite have face-centered cubic structures. Nickel decreases the austenite to ferrite transformation temperature below the room temperature. Similar to ferritic stainless steels, carbon levels are kept at minimum to enhance the corrosion resistance.

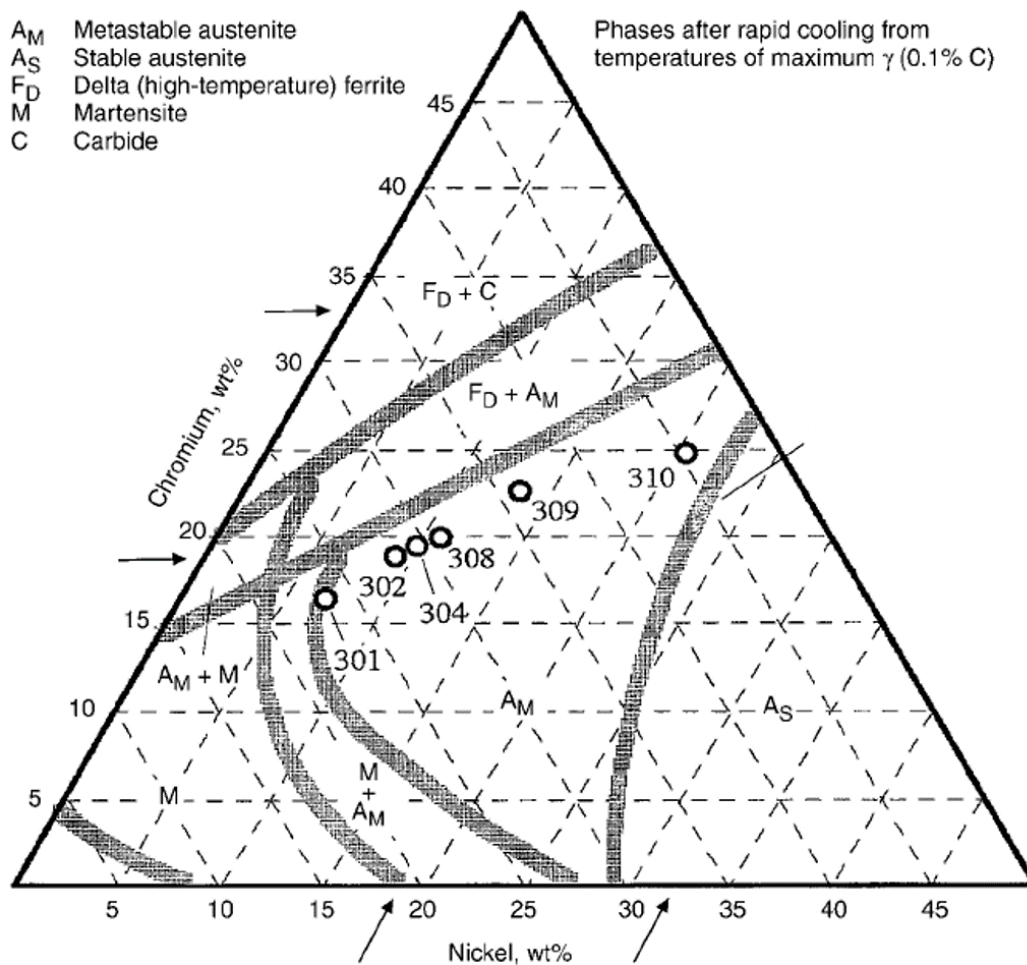


Figure 2.9 Fe-Cr-Ni phase diagram at 1100 °C and various austenitic stainless steel compositions implemented on the diagram [10].

Fe-Cr-Ni ternary system at 1100°C (Figure 2.9) reveals that as the Cr content increases, amount of Ni, which stabilize austenite phase at room temperature, also increases. The boundary just above the compositions determines the austenite-stable region and the slope of this line suggests that there is nearly a linear relationship between Cr and minimum Ni amount to stabilize austenite [10].

The austenitic stainless steels have the best corrosion resistance among the other stainless steels. The corrosion resistance of austenitic stainless steel can be further enhanced by reducing the %C amount in the steel, while increasing Cr and Ni and some other carbide formers to prevent sensitization. The main reason of sensitization is the precipitation of K_1 . Even a small change in carbon content has significant effects on the kinetics of precipitation. The nose of IT diagram of 18Cr/10Ni stainless steel is at around 70 hours in the steel containing 0.02%C, whereas it is at 1 minute in 0.08%C. Common austenitic stainless steel grades are given in Table 2.2. It should be noted that the overall carbon level is relatively low and the amount of strong carbide formers are immensely high [11,17].

Table 2.2 The compositions of selected austenitic stainless steels [11].

AISI No.	%Cr	%Ni	Max%C	Other
302	18	9	0.15	
304	19	9.3	0.08	
304L	19	10	0.03	
308	20	11	0.08	
309	23	13.5	0.2	
310	25	20.5	0.25	
316	17	12	0.08	2.5% Mo
316L	17	12	0.03	2.5% Mo
321	18	10.5	0.08	%Ti=5*%C
347	18	11	0.08	%Nb=8*%C

Note: All grades contain 2% Mn and 1%Si

Austenitic stainless steel family, as shown in Figure 2.10, is much greater than the other stainless steel types. The main reason is due to wide range of alloying elements used in these steels. Since austenitic stainless steels are not heat-treatable, the modifications of critical properties can be only done by changing the compositions. The family of austenitic stainless steel grades is summarized in Figure 2.10. It should be noted that there are two main grades; the first one is Ni-based and the second one is N and Mn based austenitic stainless steel [12].

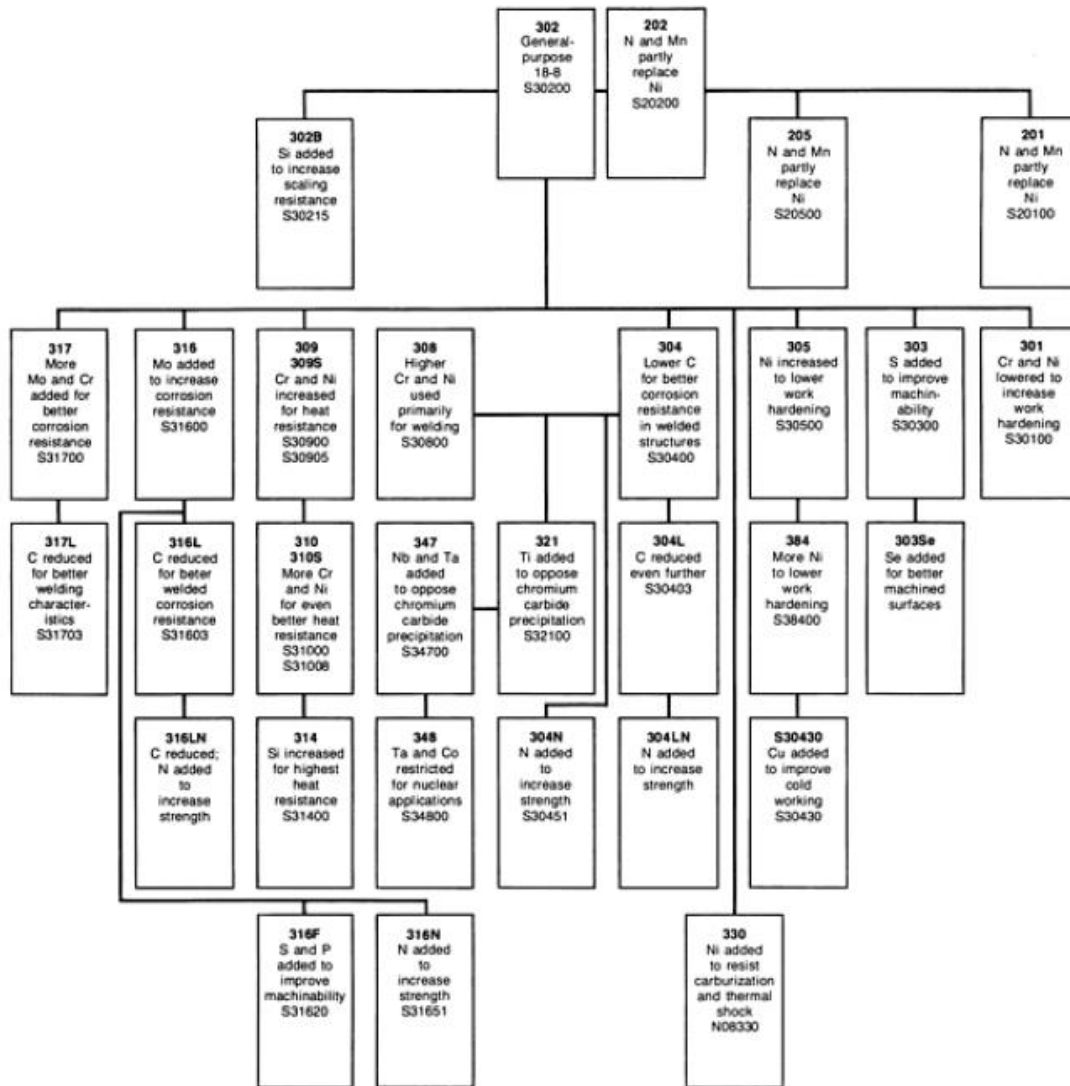


Figure 2.10 Family of austenitic stainless steels [12].

2.1.3.4. Other Stainless Steels

Apart from the stainless steels explained previously, there are some steel grades which contain either the combination of these types or some other secondary and ternary phases as precipitates. They are called as duplex stainless steels and precipitation-hardened stainless steels, respectively.

When the Fe-C phase diagram is taken into account, during the stabilization of austenite, there might be stable δ -ferrite and austenite region at room temperature. This type of stainless steels is called as duplex stainless steels [18]. These steels can be obtained only with the balanced amount of alloying elements of both austenite and ferrite stabilizers. The amount of ferrite and austenite phases is adjusted by proper

heat-treatment procedures. These stainless steels are mechanically stronger due to grain refinement (it may lead to super-plasticity at elevated temperatures) and excessive phase boundaries introduced to the system. Corrosion resistance of these steels can be categorized between ferritic and austenitic stainless steels [18].

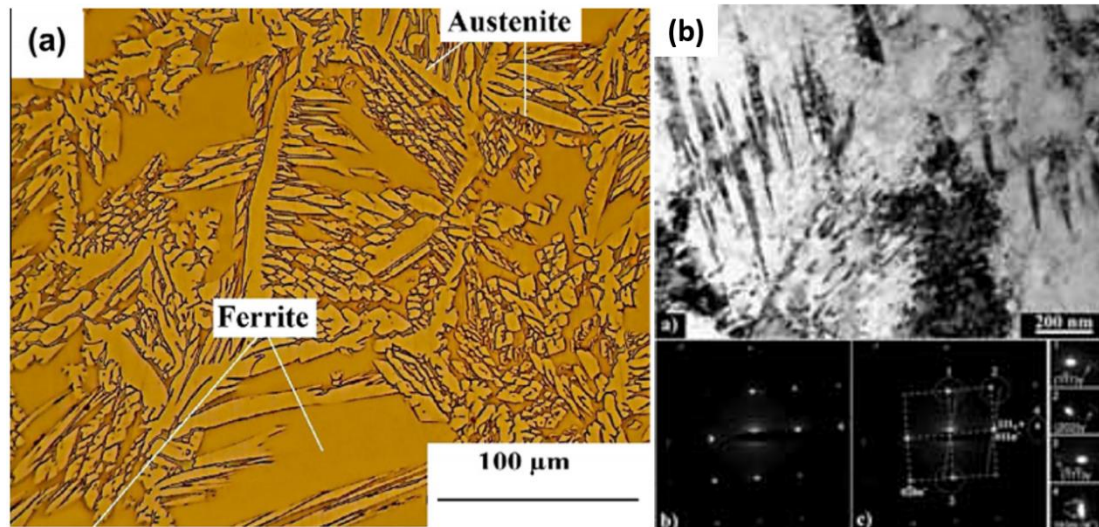


Figure 2.11 Examples for the microstructures of (a) duplex stainless steel [18] and (b) precipitation-hardened stainless steel [19].

As similar to the secondary hardening in tool steels, precipitation-hardened stainless steels contain small precipitates on the matrix, which can be either austenitic or martensitic. The main difference from secondary hardening is that the precipitates in these steels are not carbides. For instance, when 17-7 PH steel is heated to 540°C, Ni₃Al and NiAl precipitates form on the matrix. The corresponding grades are classified according to the composition and heat-treatment procedures [19].

2.1.4. Properties of CN3MN

CN3MN is a special kind of austenitic stainless steel which is commonly used in extreme corrosive environments and chlorine-containing media such as sea water systems, marine construction, oil wells and hot-pipe systems [20]. The major advantage of this grade is its superior resistance to pitting corrosion, which is a severe problem for many other stainless steel grades. A common index called Pitting Resistance Equivalent Number (30) (PREN₃₀) [20] is generally used to measure and compare resistance to pitting corrosion, and it is given as;

$$\text{PREN}_{30} = \% \text{Cr} + 3.3 \times (\% \text{Mo}) + 30 \times (\% \text{N}) \quad (\text{Eq.2.3})$$

The stainless steel grades, whose $PREN_{30}$ are greater than 45 take *Super* prefix to their classification. As given in Table 2.3, CN3MN satisfies this condition, hence this steel is known to be “Super Austenitic Stainless Steel”. The composition range can be seen in Table 2.3 according to the ASTM standards.

Table 2.3 Chemical composition range of CN3MN [21].

Element	Amount (Wt%)
Cr	20-22%
Ni	23.5-25.5%
Mo	6.0%-7.0%
Mn	<2.0%
Si	<1.0%
Cu	<0.75%
N	0.18%-0.26%
C	<0.03%
P	<0.04%
S	<0.01%
Fe	Balanced

2.2. Formation of Intermetallics

2.2.1. Common Types of Intermetallics in Austenitic Stainless Steels

Following the casting operation, the steels are usually exposed to heat-treatment operations in order to homogenize the steel and relieve the residual stress. During this post heat-treatment process, excess temperature rise may cause the formation of many precipitates due to the decomposition of austenite matrix to the various precipitates [20]. The nature of precipitates depends on several parameters such as alloying elements, matrix phase, the heat-treatment time and temperature. For instance, $M_{23}C_6$ carbide is observed in almost all kinds of stainless steels, whereas Cr-rich α' ferrite is mostly seen on ferritic and martensitic stainless steels [31]. In Table 2.4, the common precipitates observed in austenitic stainless steels were summarized and brief information are given about their formation temperatures and crystal structures. Among these precipitates, nitrides, sigma and Laves phases are commonly observed in CN3MN. In the following section, the studies conducted with CN3MN regarding to formation of these precipitates are summarized.

Table 2.4 Common precipitates observed in austenitic stainless steels [22-30].

Phase	Chem. Form	Structure	Temperature Range of Formation (°C)	Space Group	Lattice Parameter (nm)
α		bcc/bct		Im3m	0.286-0.288
α'		bcc/bct	300-525	Im3m	0.286-0.288
γ		fcc		Fm3m	0.358-0.362
σ	Fe-Cr-Mo	Tetragonal	600-1000	P4 ₂ /mnm	a=0.879 c=0.454
χ	Fe-Cr-Mo	bcc	700-900	I43m	0.892
R	Fe-Cr-Mo	Trigonal	550-650	R3	a=1.093 c=1.934
π	Fe-Mo-N	Cubic	550-600	P4 ₁ 32	0.647
Cr ₂ N			700-900	P31m	a=0.479 c=0.447
CrN		Cubic		Fm3m	0.413-0.447
M ₂₃ C ₆		fcc	600-950	Fm3m	1.056-1.065

2.2.1.1 Sigma Phase

Primarily attributed to its significant effects on many mechanical and corrosion resistance properties, sigma phase has been thoroughly investigated by many studies. It is a common agreement that sigma phase is responsible for degradation in toughness for many steel grades after even very short heat-treatment operations [31-33].

The nucleation of sigma phase depends on many parameters. According to Barcik [34], grain size and grain shape are the primary factors for the nucleation of the sigma phase. These sites create preferential nucleation sites for sigma phase. This was also confirmed by Schwind *et.al* with computer simulations [35]. Furthermore, they showed that grain size is a more critical parameter compared to grain shape for enabling the nucleation to commence [35].

Koutsoukis *et.al.* proposed that decomposition of austenite matrix to the sigma phase occurs initially at triple junctions and grain boundaries [36]. This is revealed in Figure 2.12. The corresponding TEM studies have indicated that the sigma phase is nucleated and growth along a grain boundary. Formation of such precipitates inside grains requires prolonged heat-treatments [36].

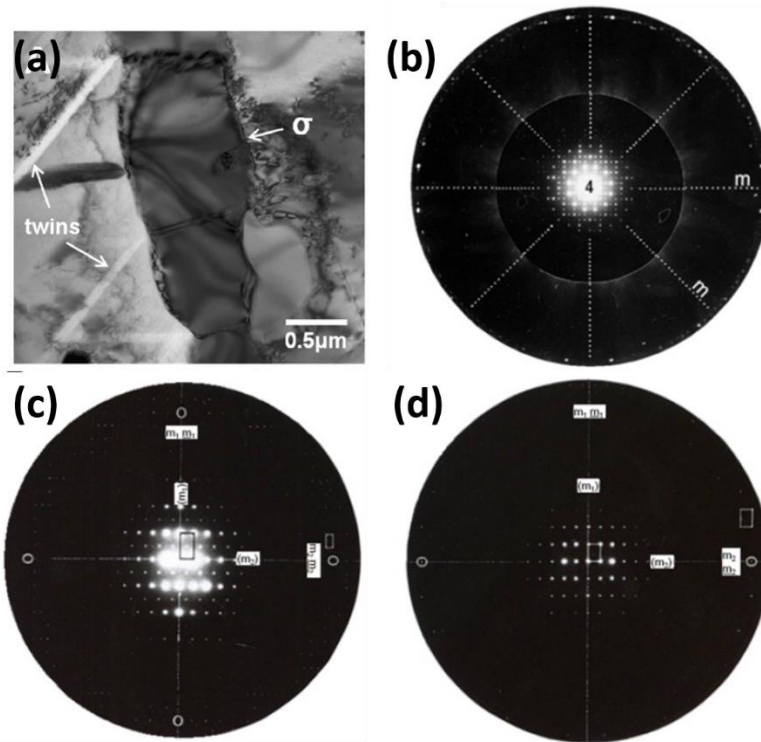


Figure 2.12 (a) BF TEM image of intergranular sigma particle (2000h, 750°C), Diffraction patterns along (b) [001], (c) $\bar{1}11$ and (d) [011] zone axes [36, 37].

In another study, the space group of sigma phase was solved as $P4_2/mnm$ (No:136) by Koutsoukis *et.al*. This structure is tetragonal with lattice parameters of $a=8.799 \text{ \AA}$ and $c=4.544 \text{ \AA}$ [36]. After investigating many sigma particles, they concluded that there was no definite orientation relationship between the precipitates and austenite matrix. The EDS analyses taken from large sigma particles revealed that these precipitates are rich in Cr and Mo and they contain less Fe as compared to the matrix [36-37].

2.2.1.2 Laves Phase

Laves phase is one of the most common intermetallics observed in the austenitic stainless steels. It can exist in both intergranular and intragranular fashion in a well-dispersed mode in the matrix. After long annealing times such as 100 hours at 950°C, it transforms into sigma phase. It is elusive to conduct a crystallographic analysis due to its highly faulted structure [36].

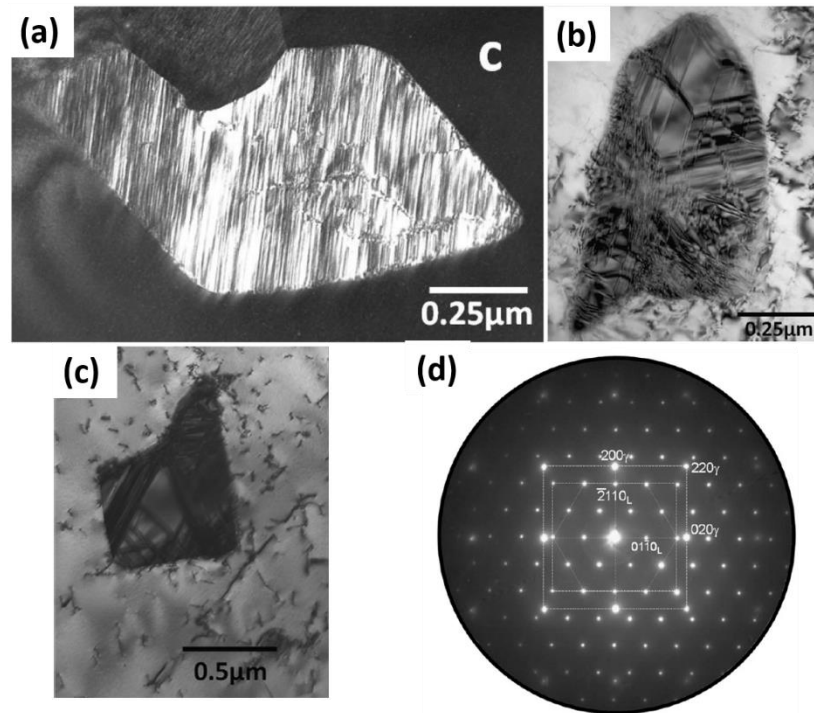


Figure 2.13 (a) DF image of intergranular Laves particle (240 hours, 950°C) (b) BF image of transgranular Laves particle along with defects parallel to each other (c) BF image a fault-free Laves phase (d) SADP from the particle in (c).

In the Figure 2.13 (a) and (b), this faulted structure of Laves phase can be clearly seen. The diffraction contrast in the DF image revealed parallel twins throughout the particle. Koutsoukis *et.al* conducted one of the rare crystallographic analysis and concluded that the orientation relationship between the particle and the matrix is $[200]_{\text{matrix}} \parallel [\bar{2}110]_{\text{Laves}}$. They observed that the most common crystal structure of the Laves phase is hexagonal, with the exception of some rare cubic Laves phase. The morphology of these particles can be polyhedral, plate-like or even needle-like representing the variety of possible shapes for intragranular Laves phase [37].

Phillips *et.al* conducted kinetic analysis on CN3MN steels [38]. They monitored the Laves to sigma solid-state phase transformation and they calculated volume and number densities of sigma and Laves precipitates upon different heat-treatments. Their results are summarized in Figure 2.14. It is clear that there must be very long heat-treatments in order to observe even a few amount of these precipitates. Although the overall precipitate content was low, they calculated 65% grain boundary coverage after annealing 60 minutes at 872°C, which would be sufficient to build a brittle network

on the grain boundaries despite the sluggish kinetics of precipitation [38-39].

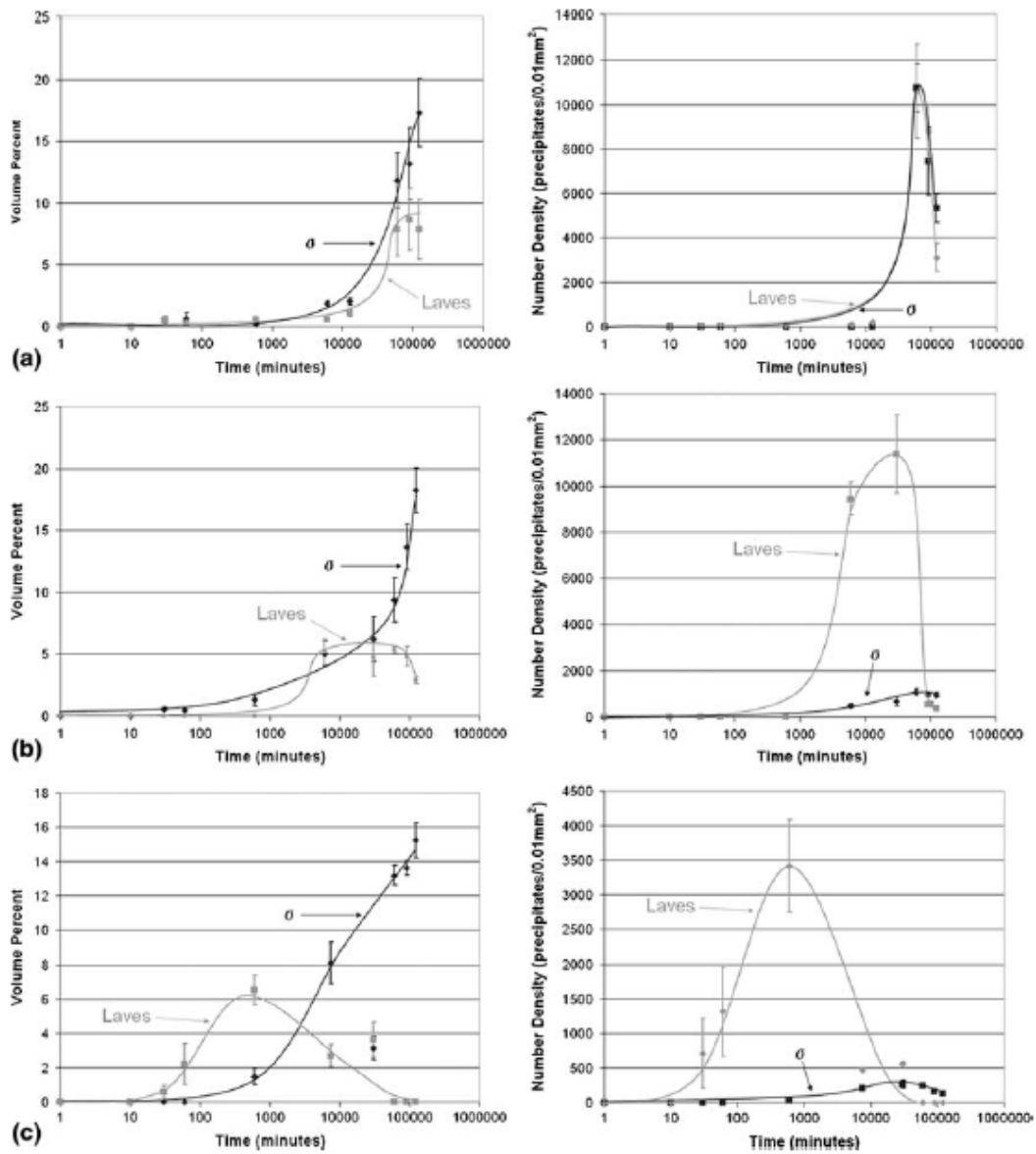
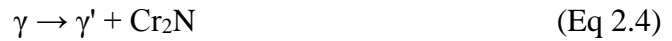


Figure 2.14 Number and volume densities of precipitates from annealed samples [38].

2.2.1.3 Nitrides

Addition of nickel into austenitic stainless used in bio-materials is not preferred because of the well-recognized toxic effects of Ni. Therefore, in order to enhance mechanical properties and stabilize austenite at room temperature with lower Ni, excess nitrogen is used in the stainless steels [31]. Addition of nitrogen to the austenitic stainless steels is a well-known process due to strong austenite stabilization effect [40].

The introduction of N to the system causes to form nitride precipitates within the steel. The most common nitride precipitate is Cr₂N. When the steel with excess nitrogen is heat-treated between 700-1000°C, the following reaction cause to form discontinuous cellular Cr₂N precipitates:



where the γ is the super saturated matrix and γ' is the N-depleted austenite [31].

Vanderschaeve *et.al* revealed that Cr₂N nucleates at grain boundaries and growth takes place towards inside the grain for the steels containing 0.9% N. They also observed that intragranular nitrides only in the pre-strained samples [41]. However, Shankar *et.al* observed intragranular precipitates with lower N-containing steels. They proposed that when the amount of N reached critical values, there would be certain lattice distortion, which pushes the N atoms to the grain boundary. If the N content is low, that kind of diffusion is not taken place [42].

Feng *et.al* also found similar results to previous studies [40]. Figure 2.15 shows cellular precipitation initiated at grain boundary and grown towards the matrix. It should be noted that even after 48-hour aging at 800°C, intragranular precipitates are not seen and the precipitate content is relatively low. According to these results, they have been concluded that the formation kinetics of these nitrides are extremely slow [40].

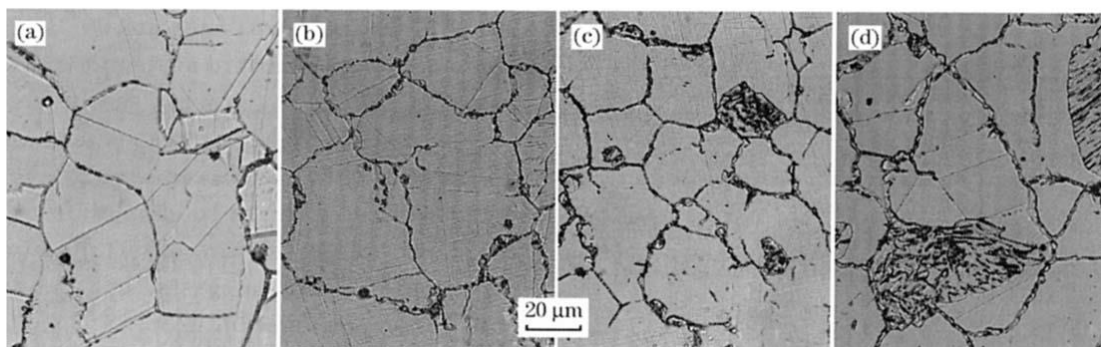


Figure 2.15 Microstructures of the samples exposed to heat-treatments at 800°C for (a) 1 hour, (b) 4 hours, (c) 12 hours, (d) 48 hours [40].

2.2.2 Effects of Precipitates on the Mechanical Properties

It would be very difficult to determine the effects of a single type of precipitate on the mechanical properties because different type of precipitates with diverse mechanical properties can be formed simultaneously. Therefore, the studies on literature generally aim to clarify overall effects of the precipitation to the mechanical properties.

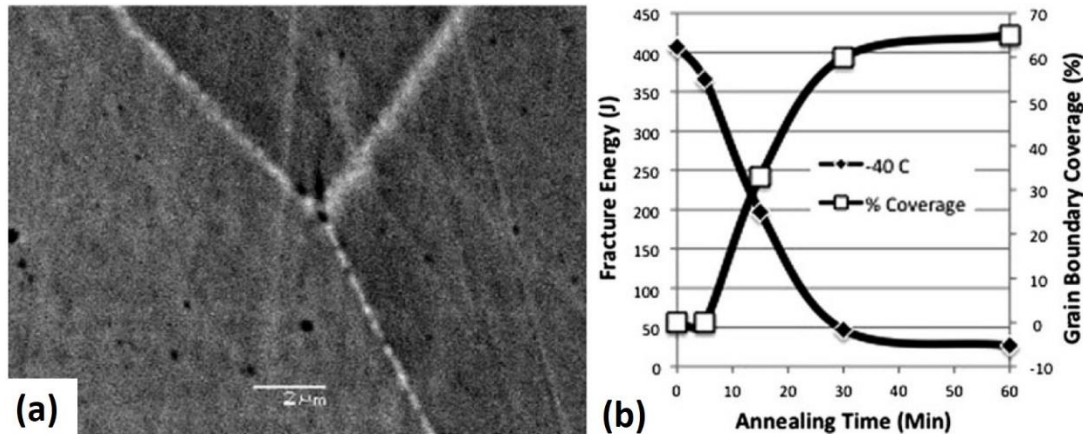


Figure 2.16 (a) BSE image of 30-min-annealed sample at 872°C (b) Impact strength as a function of time-at-temperature for an 872°C heat-treatment [39].

Muller *et.al* showed that the Mo and Cr contents were higher at the grain boundaries than the austenite matrix according to the Auger studies conducted from the specimens shown in Figure 2.16 (a). It was clear that the grain boundaries were rich in precipitates. The amount of precipitation directly affects the overall impact toughness of the steel as shown in Figure 2.16 (b). The grain boundary coverage and fracture toughness of the steel was found to be inversely related [39].

2.3. Crystallographic Defects in Steel

In the following sections, defects commonly observed in steel are described. These defects play an important role in determining the active fracture modes in steels. Examples of studies regarding to defect and mechanical properties are briefly described below.

2.3.1. Dislocations

Dislocations are one of the most important line defects as they are responsible for plastic deformation by the phenomenon called *slip*. If there are not any obstacle for

dislocation movement, dislocations can move easily during the application of forces, which explains why the real crystal can be deformed much more easily as compared to conceptually perfect crystals [43].

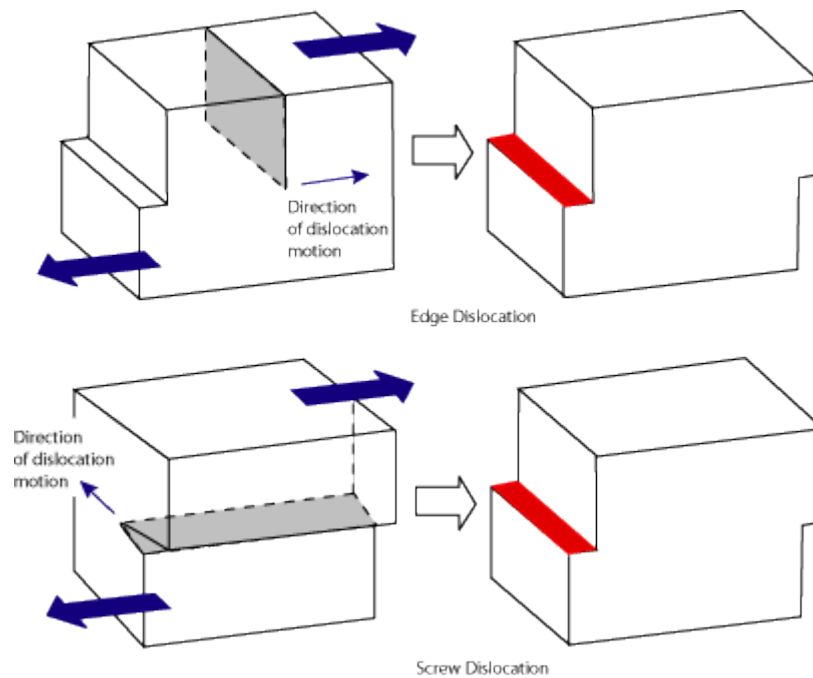


Figure 2.17 Geometrical representations of edge and screw dislocations [43].

There are two main types of dislocations, namely as edge dislocation and screw dislocation as shown in Figure 2.17. All points in the crystal which are coincident across the slip plane have been displaced by the same amount and direction. This amount of displacement is known as Burger's vector (\vec{b}) [43].

Edge dislocation can be represented by a simple geometry. According to Figure 2.17, the unslipped RHS region and slipped LHS region are separated by the dislocation line, which is always perpendicular to the slip vector for edge dislocations. Edge dislocations can slip towards a direction perpendicular to this line. Moreover, they can move vertically by the addition or subtraction of an atom from the extra half plane. This phenomenon is called as *climb* and since it requires the diffusion, it is slower than slip and it is not common at low temperatures [43,44].

Frank partial has a Burgers vector normal to the $\{111\}$ plane of the fault and the magnitude of the vector is equal to the change in spacing produced by one close-packed layer, i.e. $\vec{b} = 1/3 \langle 111 \rangle$. The Frank partial is an edge dislocation and since the Burgers vector is not contained in one of the $\{111\}$ planes, it cannot slip easily. Such dislocations are called as *sessile*, unlike the *glissile* Shockley partial. In Figure 2.20, the stacking sequences of the Shockley and Frank partials can be seen. It should be noted that right hand side (RHS) is the stacking sequence of unslipped matrix and left hand side (LHS) is the stacking sequence of the slipped region [43,44].

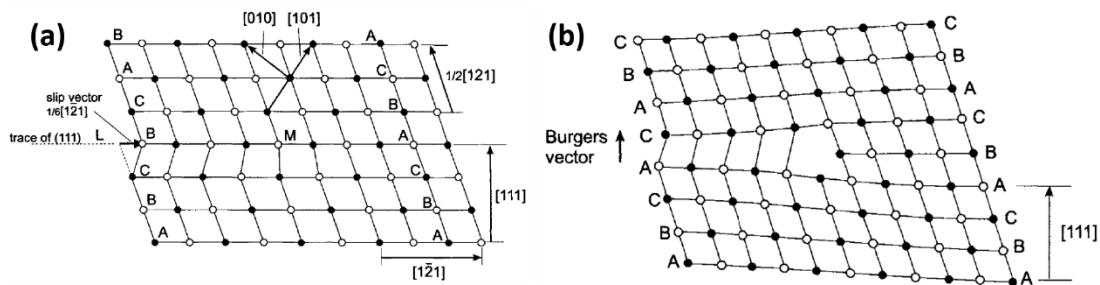


Figure 2.20 Schematic drawings of (a) Shockley and (b) Frank partials with intrinsic stacking fault [44].

Marinelli *et.al* [45] studied the dislocation structure within the SAF2507 duplex stainless steel mainly on the austenite phase. They found that the steel grade formed well-developed dislocation cell structure on the austenite matrix due to their high stacking fault energy. They also confirmed that the formation and impingement of slip bands at the grain boundaries led to the cracking, as shown in the Figure 2.24 [45].

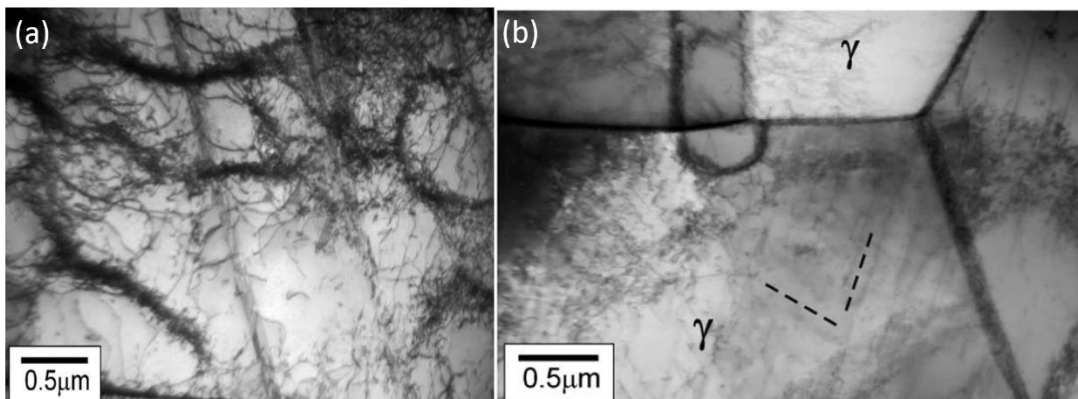


Figure 2.21 (a) Ladder-like structure developed within a twin of an austenitic grain (b) interaction of slip band with a high angle grain boundary [45].

Idrissi *et.al* [46] conducted a complete TEM study on nanocrystalline TWIP steels in order to find out dislocation and twin structures. In Figure 2.22(a), dislocations are aligned parallel to each other pointing out $[1\bar{1}0]$ direction, which is the intersection of two slip plane (111) and $(\bar{1}\bar{1}1)$.

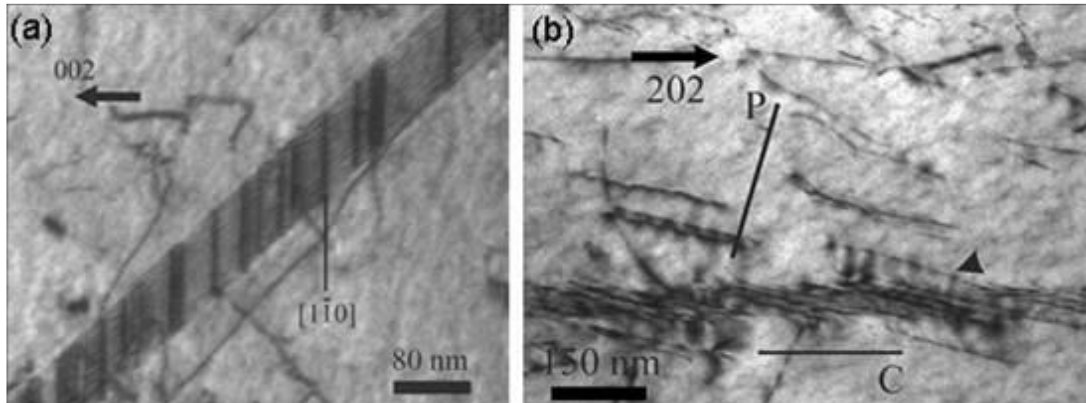
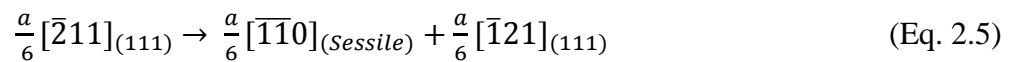


Figure 2.22 (a) Straight sessile dislocations parallel to the $[110]$ direction
(b) Dissociated Shockley Partial [46].

They offered that these dislocations were formed by a mechanism which was consistent with the previous findings. According to this mechanism these dislocations are formed by the dissociation of the Shockley partials into one sessile and one Shockley partial dislocation with the following reaction:



The Figure 2.22(b) showed Frank partial dislocation with a Burgers vector of $a/3[[\bar{1}\bar{1}1]$ This process included the dissociation of a perfect dislocation into a Frank-Sessile Dislocation and a Shockley partial [46].

2.3.2 Stacking Faults

Stacking faults, as the name suggests, are the deviations in the perfect ordering of the atoms within the structure of the material [43]. They can be divided into two groups with respect to their formation dynamics; (i) stacking faults based on the subtraction and (ii) addition of a layer between the perfect stacking. If the subtraction exists, it is called as intrinsic stacking fault, whereas in case of the addition of a layer, it becomes an extrinsic stacking fault [44].

As an example for an intrinsic stacking fault, consider the slip on the $\{111\}$ plane in fcc crystals can be considered. After the slipping between the A and B layer, the stacking sequence become ABC-AC-AB, which contains perfect hcp stacking sequence within the fcc lattices. For an extrinsic stacking fault, Wagner [47] found a ABC-ACB-CA stacking sequence after the deformation processes and named it as twin stacking fault. The schematic drawings of their model can be seen on the Figure 2.23 [43].

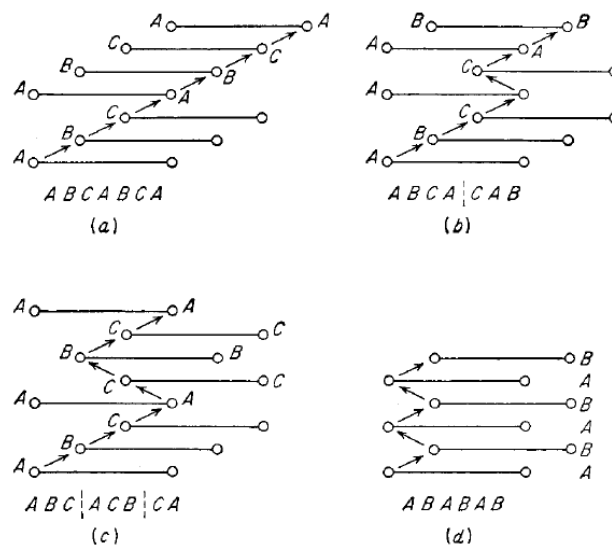


Figure 2.23 Schematic drawings of (a) fcc stacking sequence, (b) Intrinsic Stacking fault with hcp region, (c) Extrinsic stacking fault, (d) hcp stacking [43].

At this point, it may be useful to define the term *extended dislocation*, which is the hcp region separated by two partial dislocations. Since these dislocations are parallel and in close proximity, they tend to repel each other. However, this force is balanced by the surface tension of the stacking fault which is known to be *stacking fault energy* [43]. Stacking fault energy determines the width of the stacking fault and whether or not a stacking fault will form [43-44].

There are several studies aimed to determine stacking fault energy of the stainless steels [48-50]. Many of them are based on the empirical formulas depending on the composition of the steels. Some of these formulas are listed as examples:

Schramn *et.al*: $SFE = -53 + 6.2x\%Ni + 0.7x\%Cr + 3.2x\%Mn + 9.3x\%Mo$ [46] (Eq.2.6)

Rhodes *et.al*: $SFE = 1.2 + 1.4x\%Ni + 0.6x\%Cr + 7.7x\%Mn - 44.7x\%Si$ [47] (Eq.2.7)

Pickering *et.al*: $SFE = -25.7 + 2x\%Ni + 410x\%C + -0.9x\%Cr - 77x\%N - 13x\%Si - 1.2x\%Mn$ [48] (Eq.2.8)

Stainless steels are known to have relatively low stacking fault energies as compared to many conventional metallic alloy systems. A comparison between different metallic alloys is given in Table 2.6.

Table 2.6 Stacking fault energies of various alloy systems [43].

Metal	Stacking Fault Energy (mJ/m² or erg/cm²)
Brass	<10
303 Stainless Steel	8
304 Stainless Steel	20
310 Stainless Steel	45
Silver	~25
Gold	~50
Copper	~80
Nickel	~150
Aluminum	~200

2.3.3 Twins

Twinning is a secondary type of deformation mechanism in FCC crystals by which a part of crystal oriented such a way that the twinned and untwinned regions are the mirror image of each other [43]. Figure 2.24 shows the representative atomic movements during twinning in an FCC metal.

They are commonly occur when the slip system of a material is somehow restricted or critical resolved shear stress is increased so that twinning stress become lower than that of slip. That is why fcc crystals do not exhibit deformation twinning, but bcc and hcp systems exhibit twinning commonly. Twin make coherent boundaries, therefore their interfacial energy is relatively low. Similar to slip, the orientation of the twins

depends on the crystal structure. Table 2.7 shows examples of twin systems in different cubic systems [44].

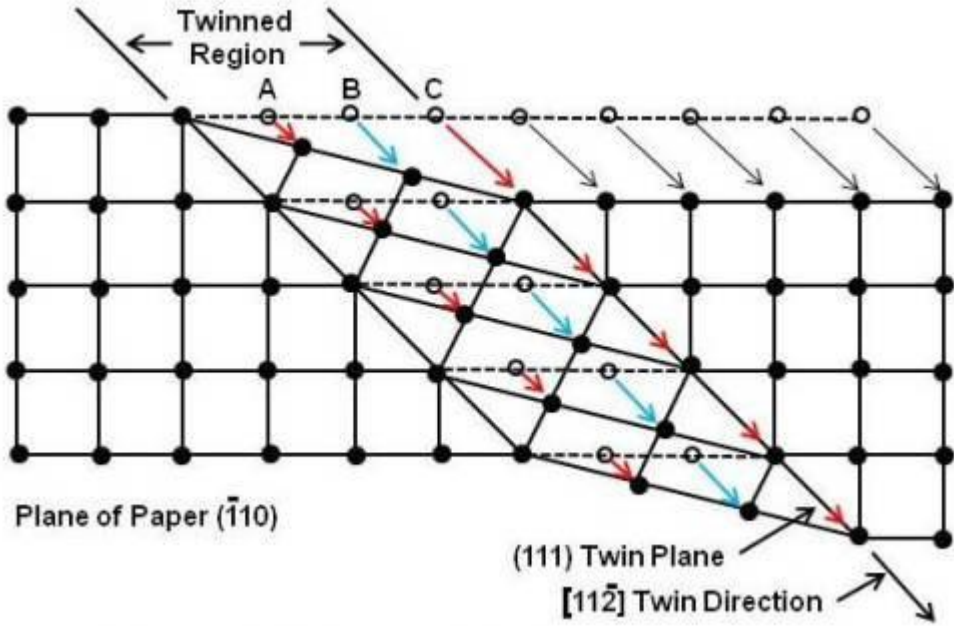


Figure 2.24 Schematic view of twinning from an fcc crystal [52].

Table 2.7 Twin systems in different cubic systems [43].

Crystal Structure	Examples	Twin System
bcc	Ta, α -Fe	(112) [111]
hcp	Zn, Cd, Mg, Ti	(10 $\bar{1}$ 2) [$\bar{1}$ 011]
fcc	Ag, Au, Cu	(111) [112]

CHAPTER 3

EXPERIMENTAL PROCEDURE

In this chapter, background information on production and heat-treatment of the CN3MN specimens and experimental procedures regarding to mechanical and microstructural analyses were given in details.

3.1. Production and Heat-Treatments of the Samples

Steel samples were obtained under as-cast conditions from a foundry which is in active cooperation with Steel Foundries Society of America. Wrought steel pieces are typically smaller in size and can be heat-treated and cooled rapidly in order to avoid embrittlement, on the other hand, cast superaustenitic stainless steels are large and cooling rate is much slower and inhomogeneous. Therefore, several regions in superaustenitic stainless ingot suffer from embrittlement. In order to mimic this embrittlement behavior, specimen from superaustenitic stainless ingots were solutionized (austenitization), quenched and heat-treated for short-period of times. Previous studies have shown that isothermal annealings above 900°C for less than 30 mins results in embrittlement.

The specimens were cut and encapsulated under Argon atmosphere before the heat-treatments. The austenitization process was conducted at 1205°C for 2 hours and followed by water quenching. Subsequently, these samples were annealed at 927°C up to 16 minutes at Iowa State University. For the long annealing times, these as-homogenized samples were annealed at 927°C for 1, 4 and 16 hours at Middle East Technical University. No encapsulation was applied to these specimens. Table 3.1 shows the codes of the samples.

Table 3.1 The annealing durations and the given specimen codes for CN3MN.

Time	0sec	30sec	1 min	2 min	4 min	8 min	16min	1hour	4hours	16hours
Sample	S0	S0.5	S1	S2	S4	S8	S16	S1h	S4h	S16h

3.2. Mechanical Analyses

Charpy impact testing and hardness measurements were conducted at room temperature to the CN3MN test specimens. Specimens for Charpy impact tests having dimensions of 5x5x55 mm were prepared by electrical discharge method according to ASTM E-23 with the title of Standard Test Methods for Notched Bar Impact Testing of Metallic Materials [53]. Tests were conducted using a Tinius Olsen Charpy Impact Test Machine at Materials Science and Engineering Department of Iowa State University, IA, USA. Charpy impact tests were repeated at least 5 times for each specimen.

The hardness tests were conducted with Wilson-Wopert Hardness Machine at Middle East Technical University and reported in Rockwell B scale. Indentations were taken from the underside regions of Charpy test specimens which have not been subjected to any plastic deformation. At least 10 individual hardness measurements were collected from each specimen and the average values were reported with the corresponding standard deviations.

Figure 3.1 (a) shows the fracture surfaces after the Charpy-impact tests and Figure 3.1(b) shows the specimen surfaces after the hardness tests.

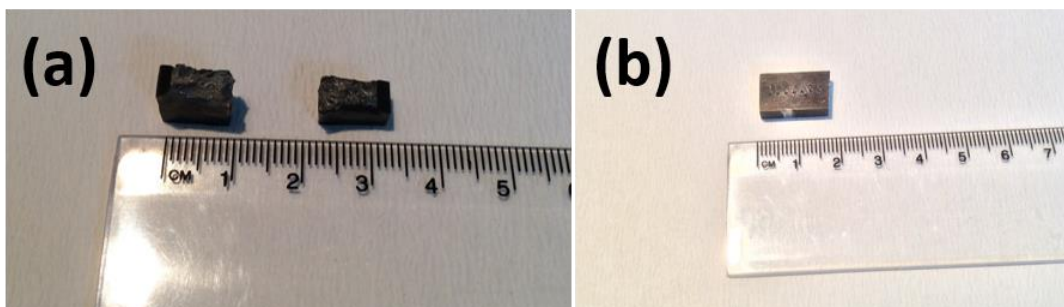


Figure 3.1 The surface of the specimens after (a) Charpy-Impact (b) Hardness tests

3.3. Structural Analyses

Structural analyses were mostly conducted using X-Ray diffraction techniques (XRD) with a Rigaku D/Max-2000 PC Diffractometer. All the specimens used in XRD experiments have a surface finish. In order to minimize the unwanted instrumental contribution, the divergence and receiving slits were set to be 1.2 and 0.3 mm. The XRD data were collected between 20° and 100° with a step size of 0.02°.

3.4. Microstructural Analyses

3.4.1. Metallographic Sample Preparation

All the samples were exposed to conventional metallographic sample preparation. The CN3MN specimens were grinded manually with the emery papers of 120, 200, 400, 600, 800, 1200 and 2000 mesh sizes. Then, these specimens were polished with diamond paste. Finally, the samples were etched with Marble's Reagent for 15-25 seconds and dried. The etchant contained 10 gr CuSO₄ in 50 ml HCl and 50 ml water.

3.4.2. Optical Microscope Analyses

Optical microscopy was mostly used for grain size measurements. After metallographic sample preparations, optical micrographs were captured by Nikon Optiphot-100 optical microscope. Grain size measurements were conducted by using Clemex Vision Professional software, which worked in a synchronization with the optical microscope. Since the grains were highly oriented, the linear markings for the grain size measurement were taken towards both longitudinal and transverse directions to get best statistical approach.

3.4.3. SEM Analyses

The microstructural characterizations were conducted by FEI NanoSEM 430 Field Emission Scanning Electron Microscope (SEM). Specimens for scanning electron microscopy analyses were prepared by the same procedure described in 3.4.1. SEM images were collected in secondary and back-scattered modes using Everhart-Thornley Detector (ETD), Low Voltage High Contrast Back Scatter Electron Detector (VCD), respectively.

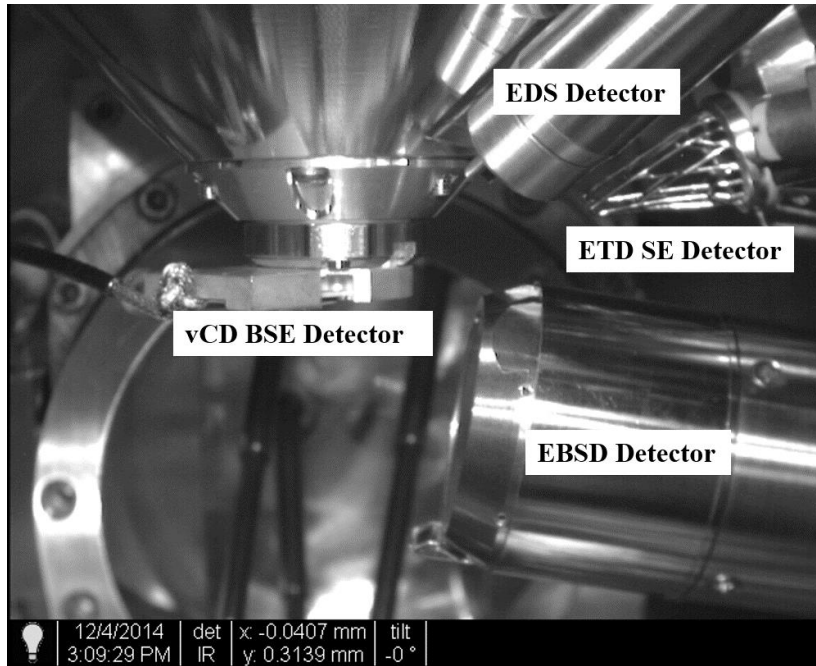


Figure 3.2 Detector positions inside the chamber.

EDS (Energy Dispersive X-Ray Spectroscopy) studies were conducted using EDAX SSD Apollo10 Detector and EDAX Genesis Version 6.0 Analysing Software adapted to FEI NanoSEM 430 Field Emission Scanning Electron Microscope (SEM). Conventional EDS data were collected at larger spot sizes and the collection times were set to the 60 live seconds. For the linear analyses, the composition lines were divided into 200 individual collection points and the dwell time was set to 1000 μ s. During the elemental mapping, dwell time were kept at 100 μ s due to long data collection times, but in order to get better contrast, high number of frames were used such as 8 or 16.

3.4.4. EBSD Analyses

Specimen preparations for Electron Back Scatter Diffraction (EBSD) studies were conducted by electropolishing using Struers LectroPol-5 electropolisher. The surface of CN3MN specimens were polished under 30 V for 10 seconds within a acidic solution of 5% perchloric acid and %95 ethanol.

For EBSD data collection, the surface of the sample must be tilted by 70° in order to increase the signal to noise ratio. This can be achieved by either tilting the whole stage or using a suitable holder with the required geometry. Data were collected with a largest aperture under 20kV acceleration voltage. A background removal was applied

to all data sets as shown in Figure 3.2. After background removal, the Kikuchi pattern can be clearly seen. The point group symmetry of the investigated phases were introduced to analyses software for crystallographic analyses.

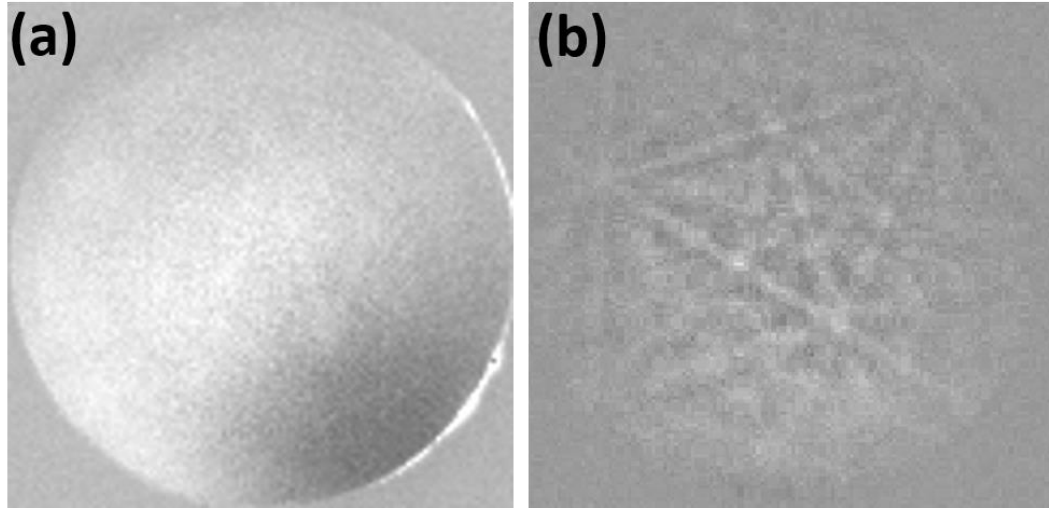


Figure 3.3 Shows the raw EBSD data collected (a) before and (b) after the background removal. Kikuchi lines are clearly seen after the correction.

3.4.5. TEM Analyses

The major effort on microstructural investigation was given to transmission electron microscopy (TEM) analyses of the CN3MN specimens under different heat-treatment conditions. Specimens for TEM have to be thin enough for electron-transparency. As a rule of thumb, 100 and 10 nm thicknesses are required for conventional and high-resolution TEM, respectively. In order to satisfy the thickness requirements, a laborious specimen preparation work should be conducted. The TEM specimen preparation routine followed in this study is summarized in the Figure 3.3. Representative sections with 400-600 μm thicknesses were cut from the bulk samples. They were further grinded to a thickness about 200 μm (Step 1) and punched to obtain 3 mm-diameter standard TEM disks (Step 2). TEM disks were further thinned down to 90 μm (Step 3) by mechanical grinding. At this point, the samples became ready for dimpling. Dimpling process was continued until an ultimate thickness of 10 μm was reached. Finally, the samples were exposed to final perforation (Step 5) by electropolishing using 33% nitric acid and 67% methanol solution. Ion milling has been also tried as an alternative technique. All specimens were cleaned against

hydrocarbon based contaminations using Fischione Model 1010 Plasma Cleaner before being inserted in TEM.

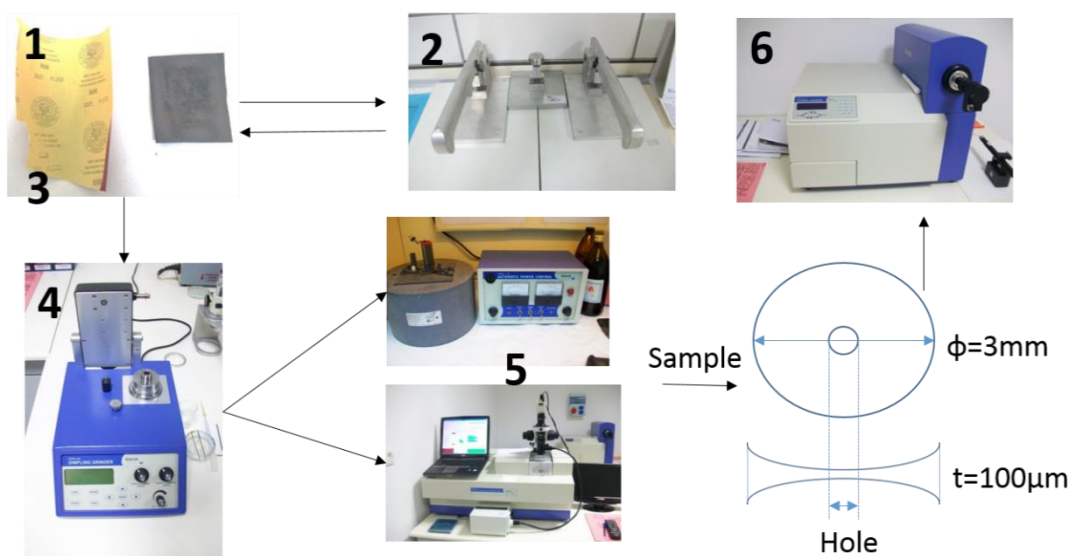


Figure 3.4 Flowchart of TEM specimen preparation.

A detailed TEM analyses were conducted using JEOL JEM 2100F (200kV-FEG) through a combined techniques of bright-field (BF) and dark-field imaging, selected area electron diffraction (SAED), convergent beam electron diffraction (CBED), high-angle annular dark-field (HAADF) and high-resolution electron microscopy (HRTEM). EDS analyses were conducted using Oxford Instruments INCA X-sight Model 6498 LN2 Cooled Detector and INCA Analyser Software adapted to TEM. EDS mapping on TEM was performed in scanning transmission electron microscopy mode. Examples for BF, DF, SADP and HRTEM images are shown in the Figure 3.5.

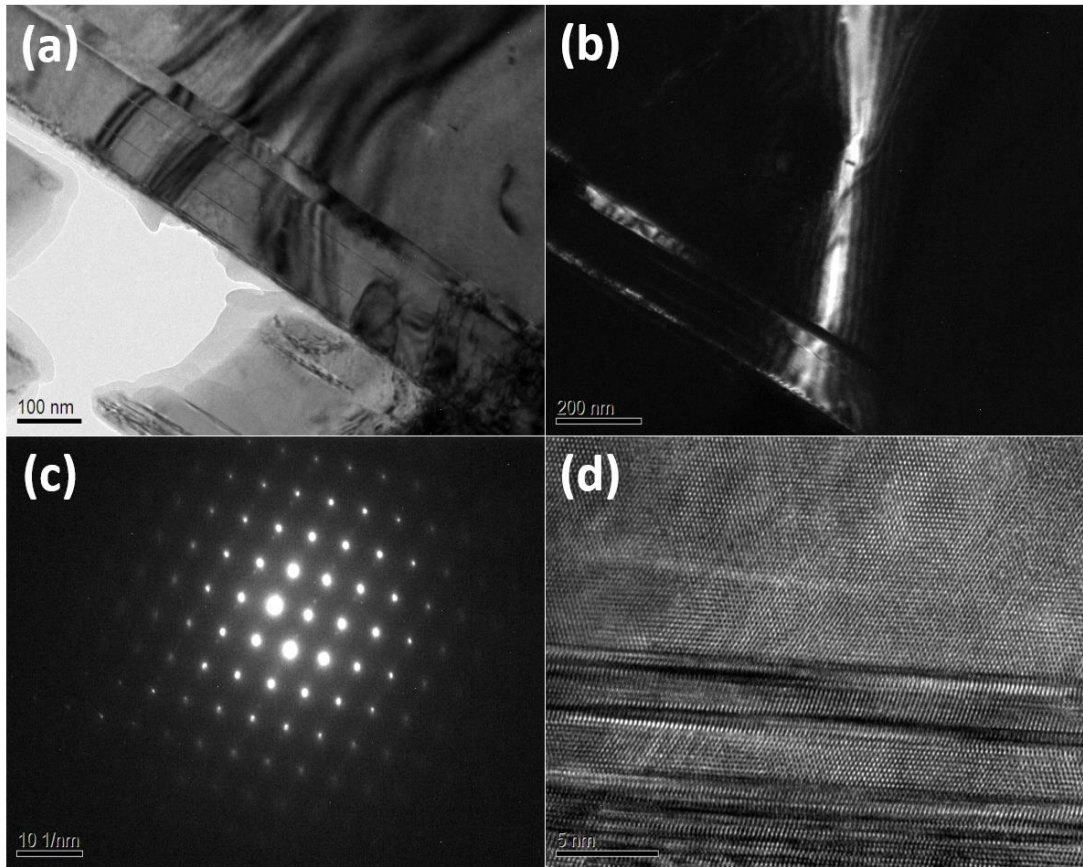


Figure 3.5 Examples for (a) BF imaging (b) DF imaging (c) SADP and (d) HRTEM imaging captured from the same region.

The in-situ TEM studies were conducted using JEOL 4000FX (300 kV-LaB₆) at Ernst-Ruska Electron Microscopy Center in Julich, Germany. Specimens were prepared with exactly the same procedure applied for room temperature experiments. A GATAN double tilt-heating specimen stage was used for in-situ experiments. Specimens were heated from room temperature to predetermined critical temperatures (850-950 °C) and isothermally hold to monitor the structural changes. Details of TEM experiments are given in the “Results and Discussion” chapter.

CHAPTER 4

RESULTS AND DISCUSSION

4.1 Stages of Embrittlement

The mechanical behavior of steels with different annealing times at 927°C were examined by hardness and Charpy impact tests. The corresponding results are shown in Figure 4.1. The axis on the left hand side shows the hardness in Rockwell B scale and the one on the right hand side shows the impact toughness in terms Joules.

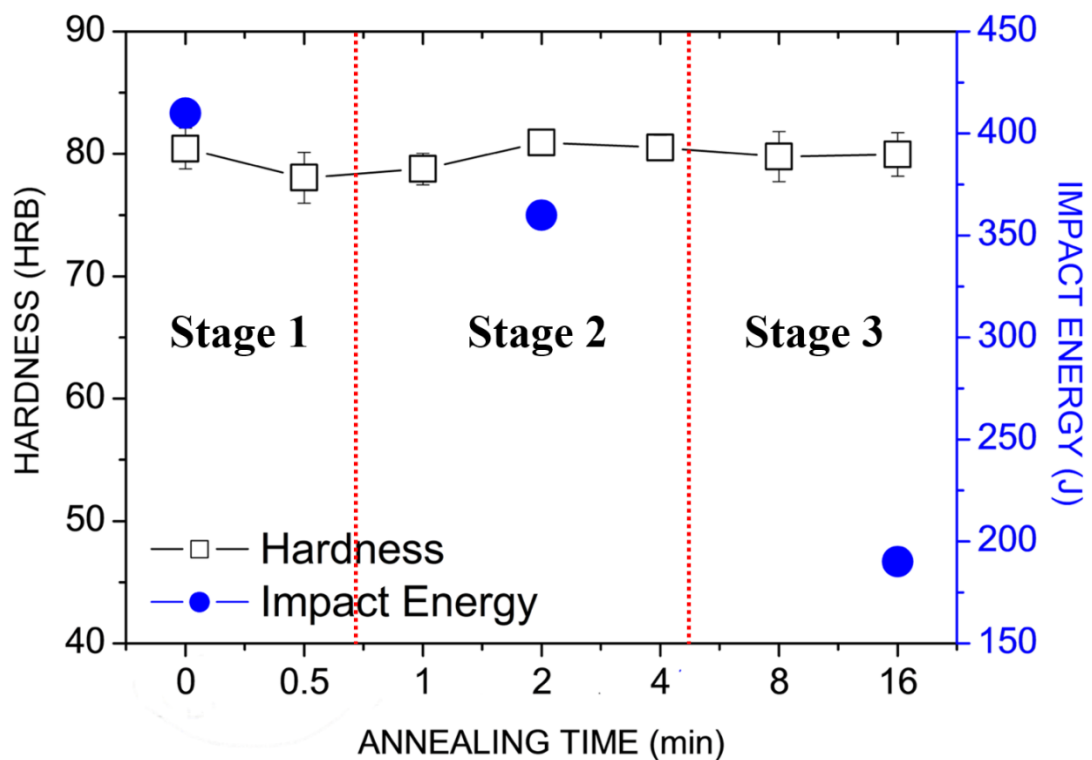


Figure 4.1 Hardness (HRB) and impact toughness (J) with respect to annealing time.

It is clear seen from the Figure that that the change in hardness value is almost kept constant with respect to annealing time. The highest hardness was observed for sample S2 with an average value of 82, whereas the lowest one was observed at S0.5 with an average value of 78. The overall hardness remains the same at an average value of 80 HRB. This result is an implication that the austenite matrix does not exhibit a drastic change or phase transformation throughout the annealing operations and stays as austenite throughout the experiments.

The permanence in the hardness is not true for the impact toughness. Even after very short annealing times such as 30 seconds or 1 minute, the impact toughness starts to drop. After 16 minutes of annealing, the impact toughness value drops to less than half of the as-homogenized state. The impact toughness for the specimen S0 is about 420 J whereas; it is only 180 J in specimen S16. The trend in the toughness drop is not the same for all annealing times. According to failure analyses conducted under SEM, it seems that there are three stages before the impact toughness drops to its lowest values. In the first stage, the fracture seems to be perfectly ductile. Figure 4.2(a) and Figure 4.2(b) show the fractographs from the specimens S0 and S0.5, respectively, representing the first stage of the embrittlement. The fractographs exhibit all characteristics of a ductile fracture. The fractured samples have cup-and-cone structure and the angle with the horizontal axis is nearly 45°. Their surfaces are matt and dull unlike the shiny surfaces commonly observed after the brittle fracture. SEM reveals that fracture surfaces are full of dimples, which are characteristic features of the ductile fracture.

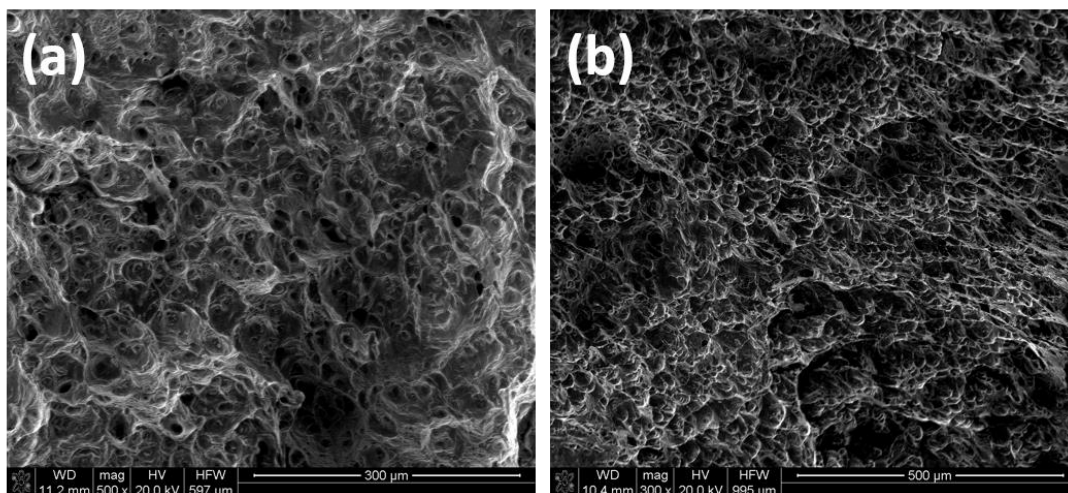


Figure 4.2 Fracture surfaces of (a) S0 and (b) S0.5.

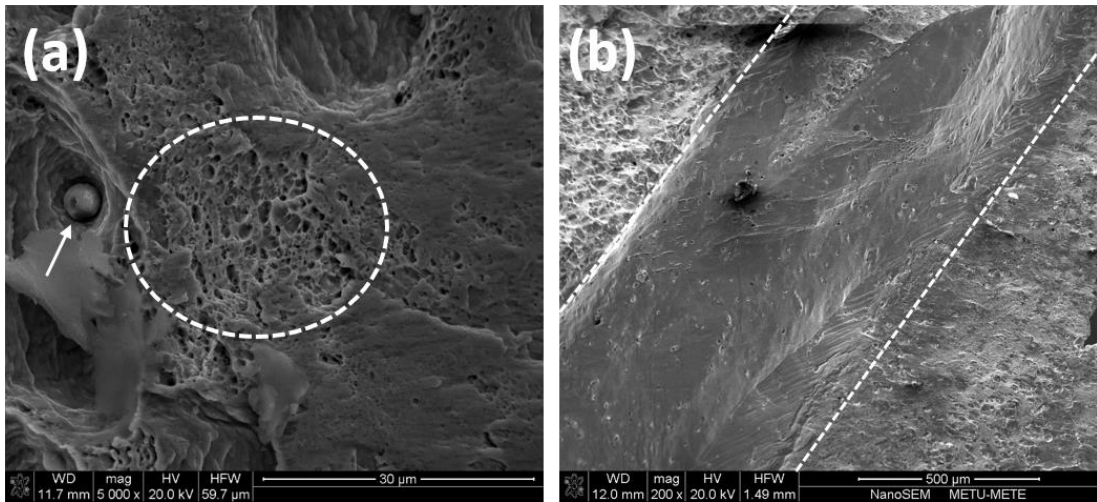


Figure 4.3 Fracture surfaces of (a) S2 and (b) S4.

Figure 4.3(a) and Figure 4.3(b) show the fracture surfaces of the samples from S2 and S4, respectively. These samples exhibit an intermediate state between ductile and brittle behavior. Figure 4.3(a) shows regions of dimples and smooth areas which are the characteristic features of ductile and brittle fracture, respectively. The encircled area in Figure 4.3(a) shows the dimples and the arrow shows the fractured piece which is entrapped inside a dimple. It should be noted that the remaining regions are smooth and have brittle characteristics. The area shown by the dashed lines in Figure 4.3(b) indicates a cleavage plane representing the brittle regions and the rest have ductile features. The area covered by brittle regions is more than the ductile regions in the second stage of embrittlement.

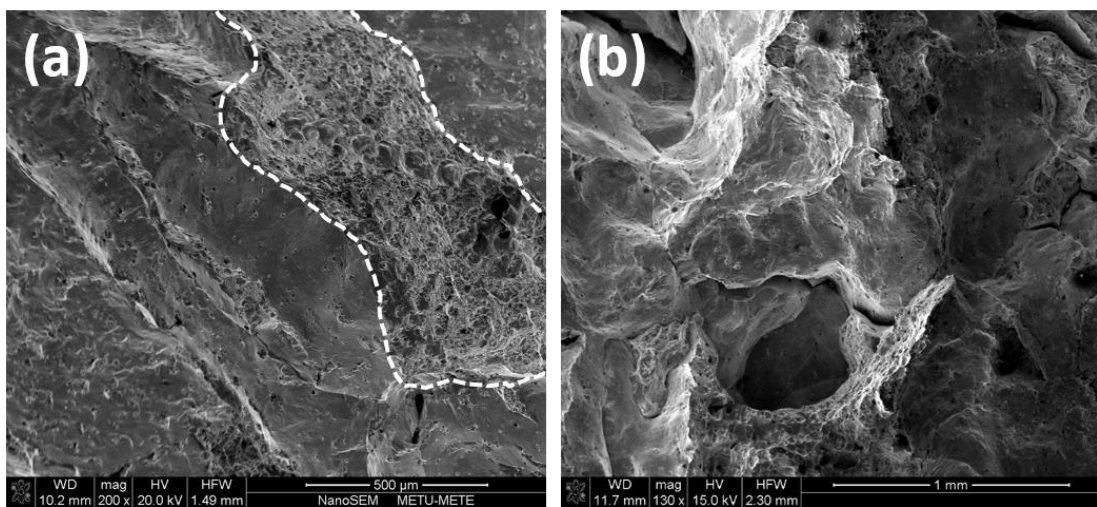


Figure 4.4 Fracture surfaces of (a) S8 and (b) S16.

The third stage of the embrittlement exhibit almost fully brittle behavior. The Figure 4.4 (a), representing S8 condition, shows that features of brittle failure dominate the overall fracture surface. Figure 4.4 (a) shows a single small ductile region trapped between the brittle regions. Figure 4.4 (b) shows the specimen under S16 condition at lower magnification (X130). This specimen exhibits only brittle fracture characteristics. The fracture surface is smooth and bright and lacking of any cup-and-cone structure. Most of the cracks exist along the grain boundaries inferring that the cracks propagate in an intergranular manner.

To sum up the initial fractography results, it can be concluded that isothermal annealing of CN3MN superaustenitic steel at 927 °C for relatively short duration (i.e. 16 minutes) results in sharp decrease in impact toughness while keeping the hardness values the same. The underlying reasons for such a drastic change in impact toughness will be analyzed in details in the following chapters.

4.2 Intergranular Embrittlement

4.2.1 Microstructures

As it was previously explained in the literature review part, the formation of precipitates is almost inevitable in the superaustenitic stainless steels. The relatively high annealing temperature used in this study may even promote the precipitation. On the other hand, the annealing durations are shorter as compared to conventional heat-treatment procedures. Therefore, whether or not short-term annealing at high temperatures causes any grain boundary precipitation, heat-treated specimens was examined using scanning electron microscopy. Specimens for grain boundary analysis were polished and deeply etched in Marble's reagent. Figure 4.5 (a) and (b) shows specimen S0 exhibiting a triple junction and a grain boundary. The grain boundaries are clean and free of any precipitation. However, just after a very short annealing of 30 seconds, the precipitates started to form along the grain boundaries, as shown in Figure 4.5 (c) and Figure 4.5 (d). These two figures were obtained from specimen S0.5. It should be noted that after this short annealing, the precipitates are high in number, but small in average size. The average size after 30 seconds annealing was found to be on the order of 400 nm and number density was calculated as around $20 \mu\text{m}^{-1}$.

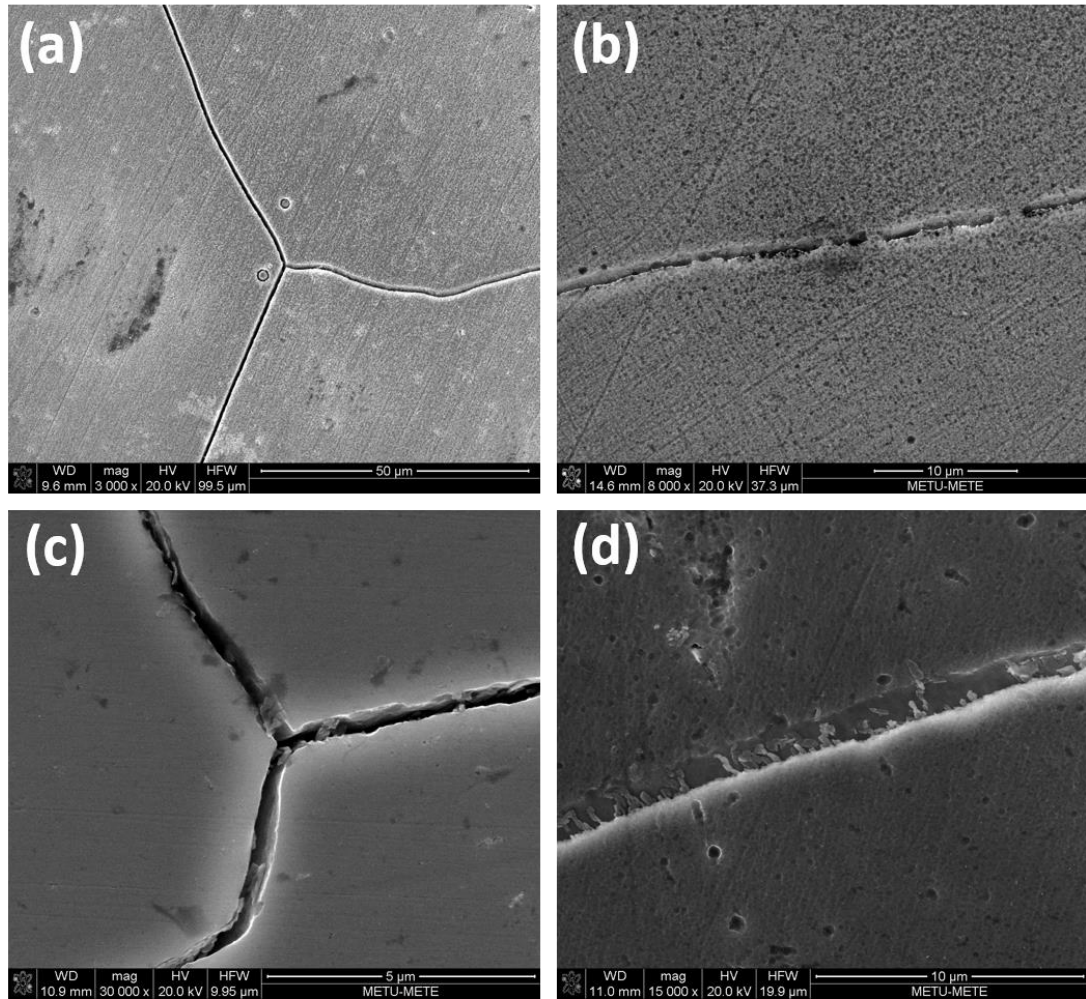


Figure 4.5 Deeply etched specimens representing the (a), (b) S0 and (c), (d) S0.5.

The representative microstructures from specimen S2 are shown in Figure 4.6(a) and (b). The number of the precipitates is considerably increased to $36 \mu\text{m}^{-1}$ after two minutes of annealing. The average size of the precipitates is still the same with S0.5 condition. Therefore, it can be concluded that precipitates with sluggish growth kinetics tend to nucleate more along the grain boundaries. The precipitates in the specimen S4 showed an abrupt coarsening of precipitates. The average size of the precipitates after 4 minutes of annealing was found to be $0.99 \pm 0.15 \mu\text{m}$. The grain coarsening decreases the average number density of intergranular precipitates to the $10 \mu\text{m}^{-1}$. A grain boundary network is started to form as it can be inferred from the Figure 4.6 (c). Figure 4.6 (d) clearly reveals that the precipitates tend to form along the grain boundary rather than settling within the grains.

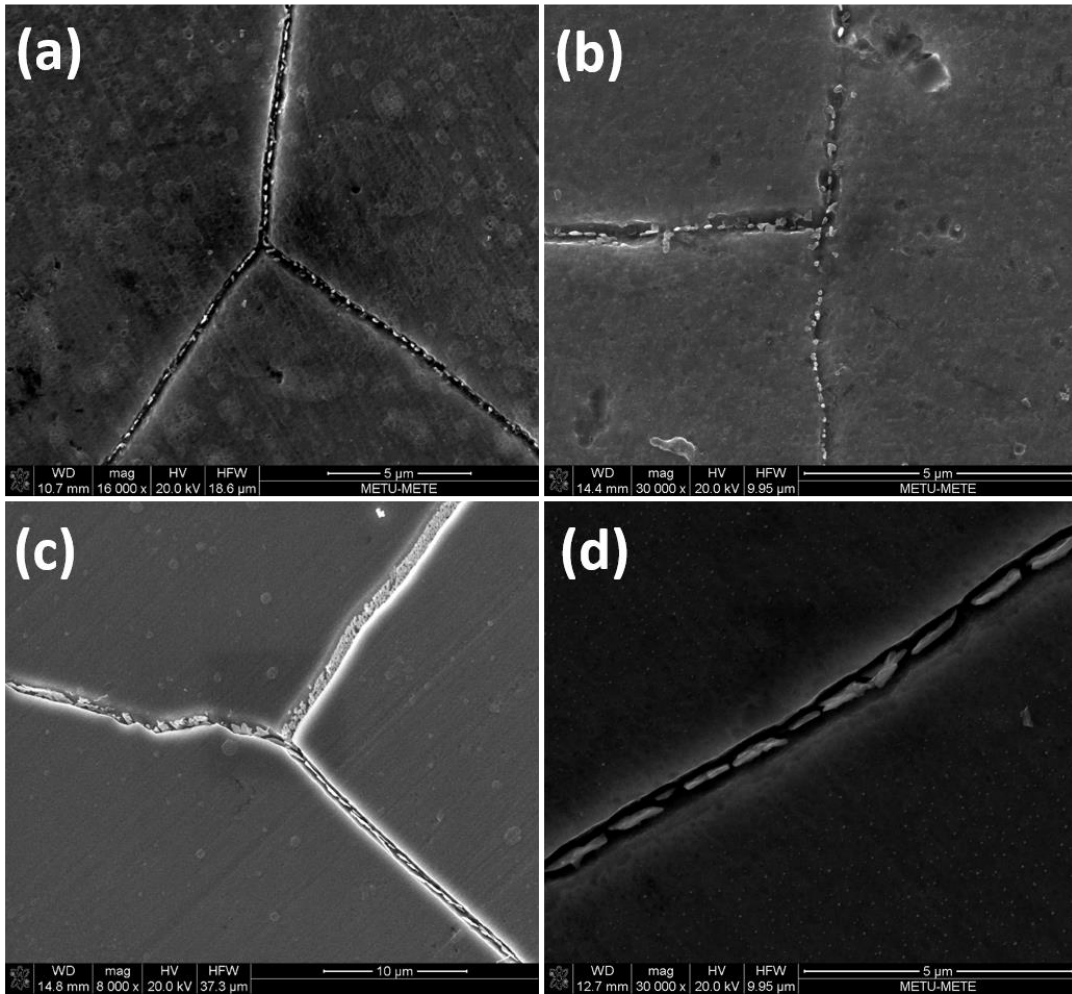


Figure 4.6 Deeply etched specimens representing the (a), (b) S2 and (c), (d) S4.

Grain boundary coverage by the precipitates increases in volume percent after 8 and 16 minutes of annealing. Figure 4.7 (a) and (b) shows the precipitates in S8 condition at a lower and higher magnifications. It is clearly seen that grain boundary is almost completely covered by precipitates. Therefore, any calculation about the size and number density of the precipitates could not be conducted. Figure 4.7 (c) and (d) were captured from S16 specimen. Although the grain boundary is fully covered by precipitates after 16 minutes annealing, no intragranular precipitates were observed in any of these specimens within the limitation of FEG-SEM. This is further proved by the use of EBSD along a triple junction grain boundary. Figure 4.8 shows the SEM images of 16 minute heat-treated specimen embedded with an EBSD pattern. EBSD displays the junction point of three grains with three different crystallographic orientations. The small size of these precipitates makes difficult to conduct a crystallographic analyses using EBSD on the grain boundaries however, it is clearly

revealed that the precipitates observed after isothermal heat-treatments are nucleated and grown along the grain boundaries.

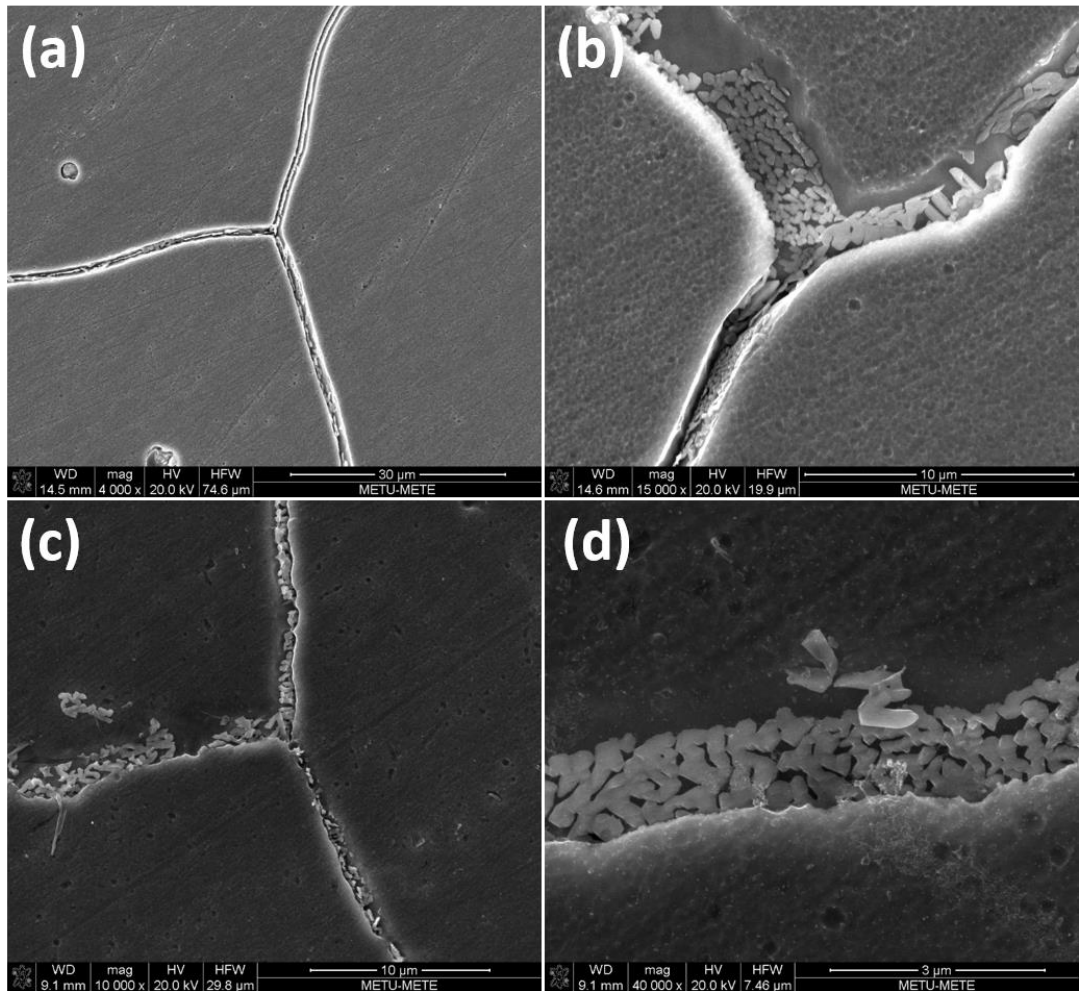


Figure 4.7 Deeply etched specimens representing the (a), (b) S8 and (c), (d) S16.

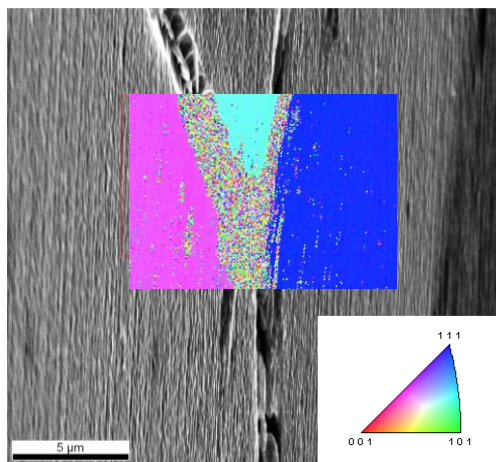


Figure 4.8 SEM image of S16 embedded with an EBSD map.

4.2.2 Structural Analyses of Precipitates

According to the SEM and EBSD analyses, isothermal annealing of CN3MN at 927 °C for relatively short durations result in the formation of grain boundary precipitation. As it was explained in literature review chapter, the impact toughness of the certain steels is extremely sensitive to small amounts of precipitation. This shows that impact toughness of highly alloyed steels, i.e. CN3MN, may be less dependent upon total precipitation volume percentage than the nature of the precipitates. Therefore, this grain boundary precipitation observed in relatively short heat-treatments is well deserved to be investigated in details. Since the sizes of these precipitates are too small to investigate them under SEM, further TEM studies were conducted. The short term heat-treatments makes TEM analyses difficult, since secondary phases were not observed in significant amounts in TEM foils. Another complication was resulted because of the large grain size of the cast material. In that case, it was difficult to find grain boundaries to examine. However, after much searching nanoprecipitates were found along grain boundary regions as shown by the bright-field (BF) images shown in Figure 4.9 for 16 minute heat-treated specimen.

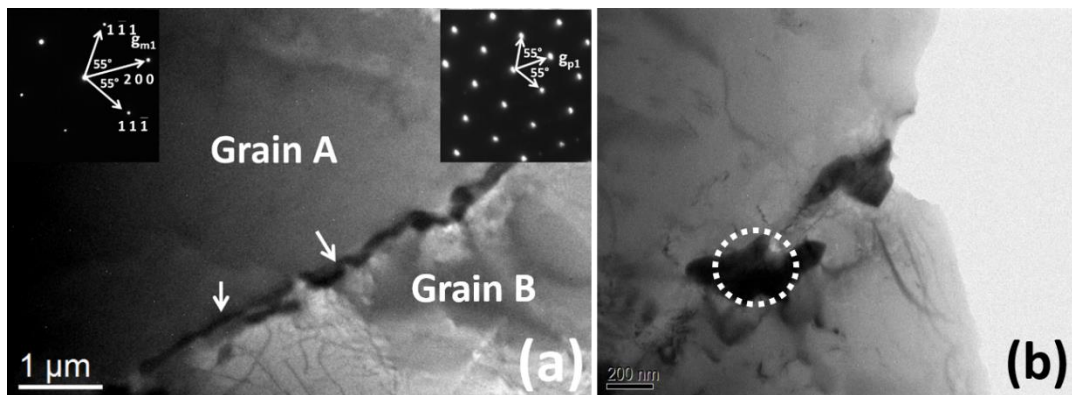


Figure 4.9 (a) BF image representing the grain boundary precipitation observed in S16. (b) Closer look to a single precipitate observed in (a). Insets show the SADP.

The Figure 4.9 (a) and (b) show the grain boundary precipitation under TEM. The size and morphology of these precipitates are in good agreement with the SEM observations. The selected area electron diffraction patterns (SADP) collected from the austenite matrix along $\langle 011 \rangle$ zone axis and the precipitates are shown in upper right and left insets of Figure 4.9 (a), respectively. A detailed analysis of electron diffraction was performed from the precipitates. Electron diffraction studies suggest

that one type of precipitate dominates the grain boundary precipitation after 16 minutes. The common secondary phases observed in austenitic stainless is given in Table 2.4. The interplanar spacing and their angular relationship measured from grain boundary precipitates could not be matched with any of the expected secondary phases for stainless steels tabulated in Table 2.4. The list of measured interplanar spacing is given in Table 4.1. It should be noted because of the small size and low volume percentage, Bragg reflections could not be collected from these precipitates using X-ray diffraction analysis. EDS results collected from the austenite grains and the precipitate encircled in Figure 4.9 (b) are given in Table 4.2. Grain A and B represent on this table the grains on the left and right hand side of the encircled precipitate. The chemistry of the austenite grains are good agreement with ASTM standards. Likewise the interplanar spacing, the chemistry of these precipitates could not be matched either with any of the known precipitates.

Table 4.1 List of interplanar spacing calculated from SADP patterns at various zone axis

Interplanar Spacing (Å)
6.6
5.7
2.6
2.3
2.1
1.6

Table 4.2 The composition defined by ASTM Standards and the results of the EDS measurements collected from the regions shown in Figure 4.9(b).

Area	Si	Cr	Mn	Ni	Mo	Fe
ASTM	<1.0	20.0-22.0	<2.0	23.5-25.5	6.0-7.0	Balanced
Grain A	1.0±0.1	20.8±0.2	1.1±0.1	24.0 ±0.1	6.7 ±0.2	46.5±0.3
Grain B	1.0±0.0	20.6±0.0	1.2±0.0	24.1±0.1	6.8±0.2	46.4±0.2
Precipitates	6.2±0.3	22.5±0.4	0.6±0.1	23.3±0.4	33.3±0.5	14.3±0.2

The composition of the precipitates is far more different than the austenite matrix. The precipitates are highly enriched by Si, Cr and Mo, but deficient from the Fe and Mn. This may indicate formation of a new structure within this particular steel. One intriguing observation is that the diffraction data collected from precipitates have a similar angular relationship with the fcc-austenite phase. For example, the angular relationship between the SADP collected from precipitate in Figure 4.9 and the neighboring austenite matrix is exactly same along $\langle 110 \rangle$ direction. The interplanar spacing values, on the other hand, are quite different but still related to each other. The interplanar spacing between 002 planes in austenite is approximately one third of the distance over the same orientation in the precipitate. If a cubic structure is assumed for the precipitate based on the angular relationship observed in electron diffraction, the lattice parameter would become approximately 10.8 Å. The same relationship is also observed in high-resolution TEM (HRTEM) data.

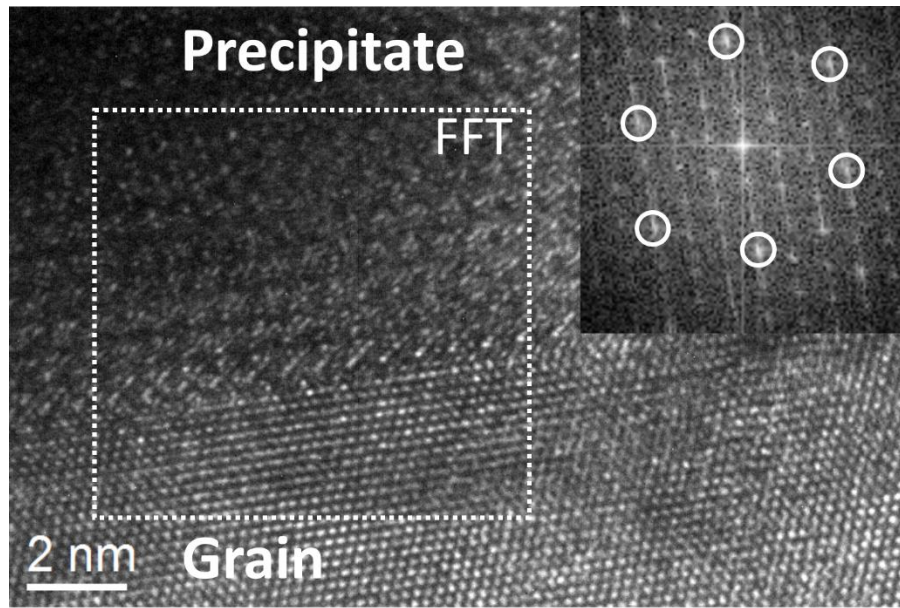


Figure 4.10 HRTEM image showing the interface between the austenite grain and the precipitate in S16 specimen. The inset shows the FFT of the dashed region.

Figure 4.10 shows the HRTEM image collected from the austenite and precipitate interface. Austenite crystal is oriented along $\langle 110 \rangle$. The fast-Fourier transform calculated from the dashed region shows bright spots matching with austenite phase (circled in the inset) and several faint spots corresponding to the precipitate. These bright reciprocal spots are shared by these two phases indicating a strong the epitaxial relationship between the austenite and precipitate. If a cubic structure is assumed to be correct, the crystallographic relationship between these grains become $\langle 001 \rangle_{\text{austenite}} // \langle 001 \rangle_{\text{precipitate}}$. The relatively short reciprocal vectors reveal that the precipitate should have larger lattice parameter. The lattice parameter calculated using FFT agrees well with the SADP results. As previously mentioned in literature review chapter, the intermetallic compounds σ , χ , and Laves dominate in terms of overall volume percent of precipitation studies of the cast superaustenitic steel. On the other hand, the precipitates formed in short-term annealing in this study do not match either of these phases. Currently, detailed crystallographic information (i.e. Space Group) of these precipitates is missing and further efforts are needed to solve this structure. The origin of these precipitates is discussed in the following chapter.

4.2.3 Origin of the Precipitates

The precipitation observed after short-term annealing process is more than expected. Muller *et.al* studied the grain boundary precipitation in CN3MN grade steels and found that after annealing 60 minutes at 900°C, the linear percentage of precipitation on the grain boundaries is around 65% [39]. However, the samples studied on this study exhibit a widespread precipitation along the grain boundaries even after 8 minutes. The underlying reasons for the fast precipitation are investigated in different aspects.

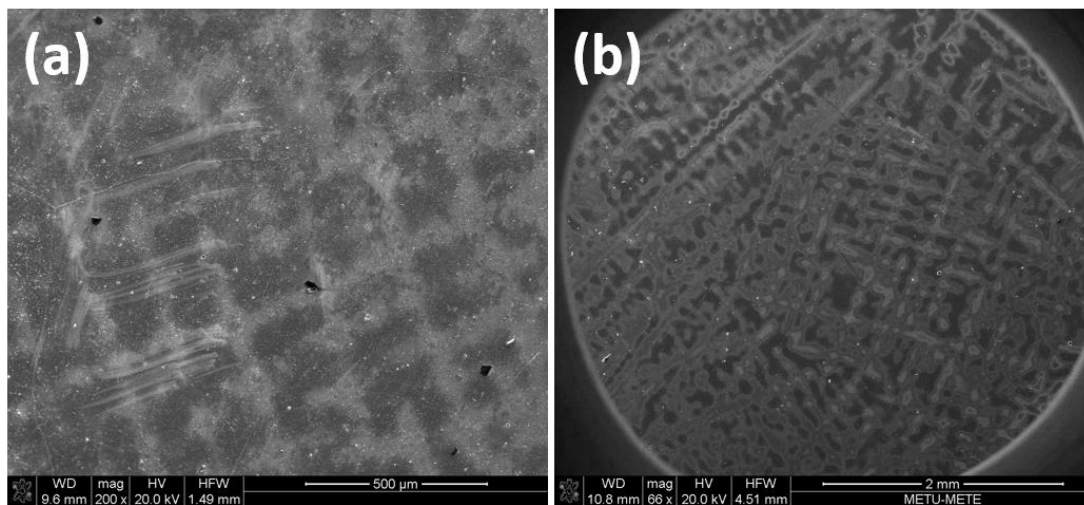


Figure 4.11 Dendrite-like macrostructures from (a) S0 and (b) S0.5.

When the CN3MN specimens were investigated at relatively low magnifications, a dendrite-like macrostructure appear throughout the samples in a very homogeneous manner as shown in Figure 4.11 (a) and (b). These are probably from the early production steps during the casting operation. The reason why they called as dendrite-like is that they differ from dendrites based on a very fundamental aspect. The formation of dendrites is a crystallographic phenomenon. Dendrites prefer definite crystallographic orientation for their growth. For example, Al dendrites, which is a face-centered cubic material, grows only $\langle 100 \rangle$ direction, whereas body-centered tetragonal Sn dendrites grow on $\langle 110 \rangle$ direction [54]. If these structures were dendrites, they must have also grown on well-defined crystallographic orientations and they would have been visible on EBSD analysis. The dendrite-like region shown in Figure 4.12 (a) was exposed to the EBSD and the results were given in Figure 4.12 (b). According to the EBSD pattern, except the noise and dead pixels, the region consist of only one crystallographic orientation, indicating no dendritic

macrostructure. Therefore, the formation of these structures does originate from well-oriented dendrites.

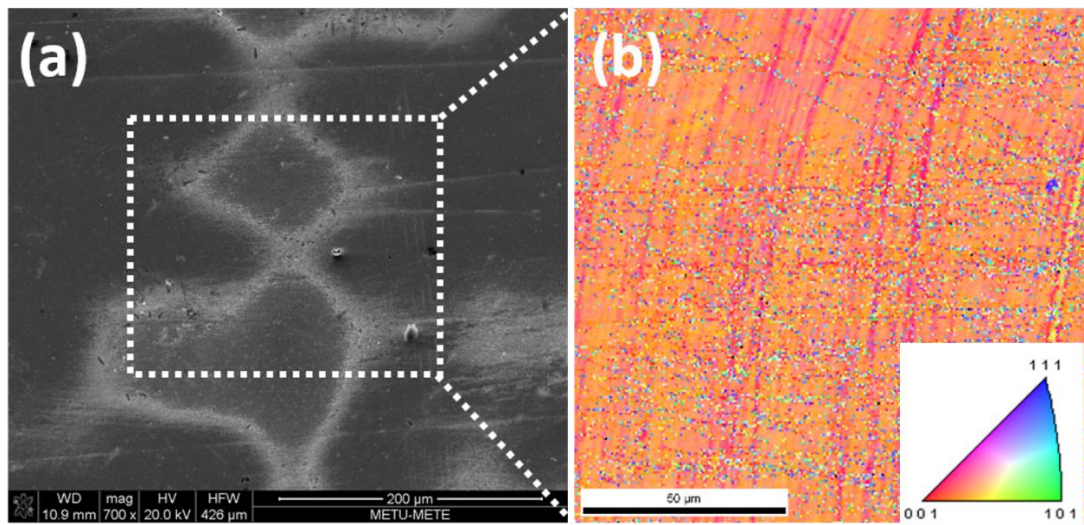


Figure 4.12 (a) Dendrite-like macrostructure from S0.5 and (b) EBSD pattern of the area defined by dashed lines in (a).

Another possibility of having contrast variation on etched specimens is the local compositional heterogeneities. Since all the alloying elements, more or less, affect the corrosion resistance, the etching process must occur at different rates in the areas with different compositions. Being fast and sensitive at low magnification, EDS line analysis is very useful tool to check the local compositional differences. Figure 4.13 (a) and (b) shows the EDS line scan analysis across the dendrite-like region.

The Figure 4.13(b) reveals that the specimen is not homogeneous in terms of chemical composition. According to the line scan analysis, white contrast regions contain more Fe and less Cr. But the real difference comes due to Mo content. If the very small change in Cr is neglected, it is possible to claim that gray regions are Mo-rich and Fe-deficient. The white regions are just the opposite in terms of Fe and Mo. The interesting point is that segregation occurs in such a way that the change in the composition between the white and gray areas are similar to the ones between the matrix and the precipitates as can be seen in Table 4.2

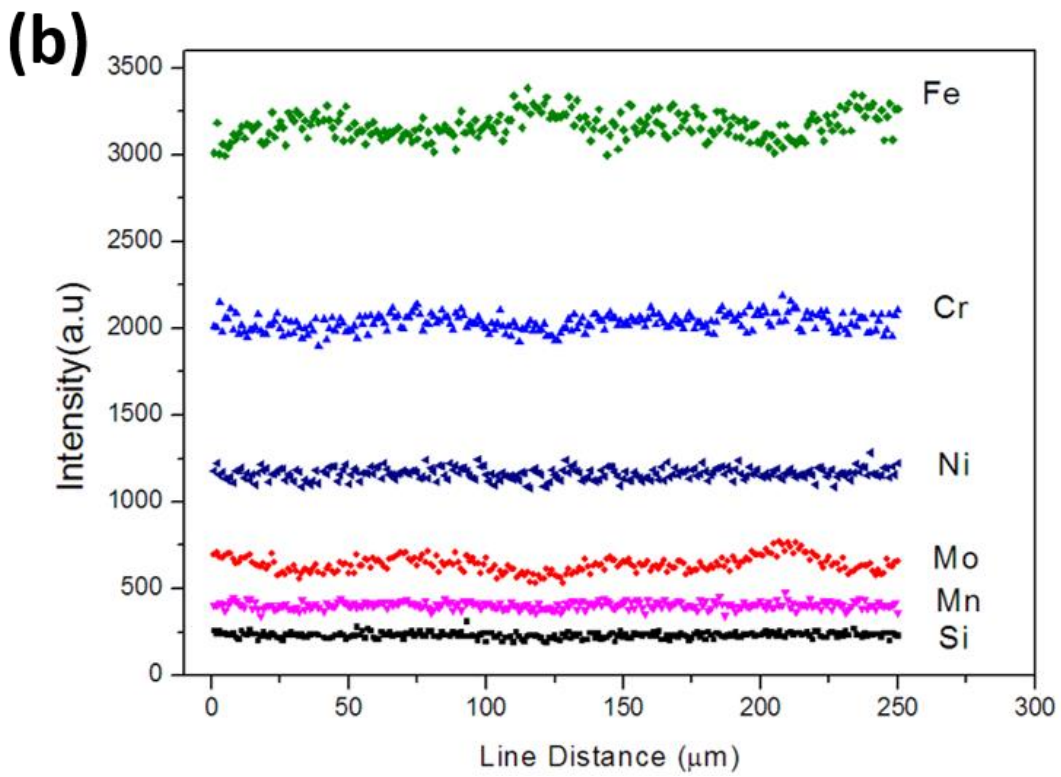
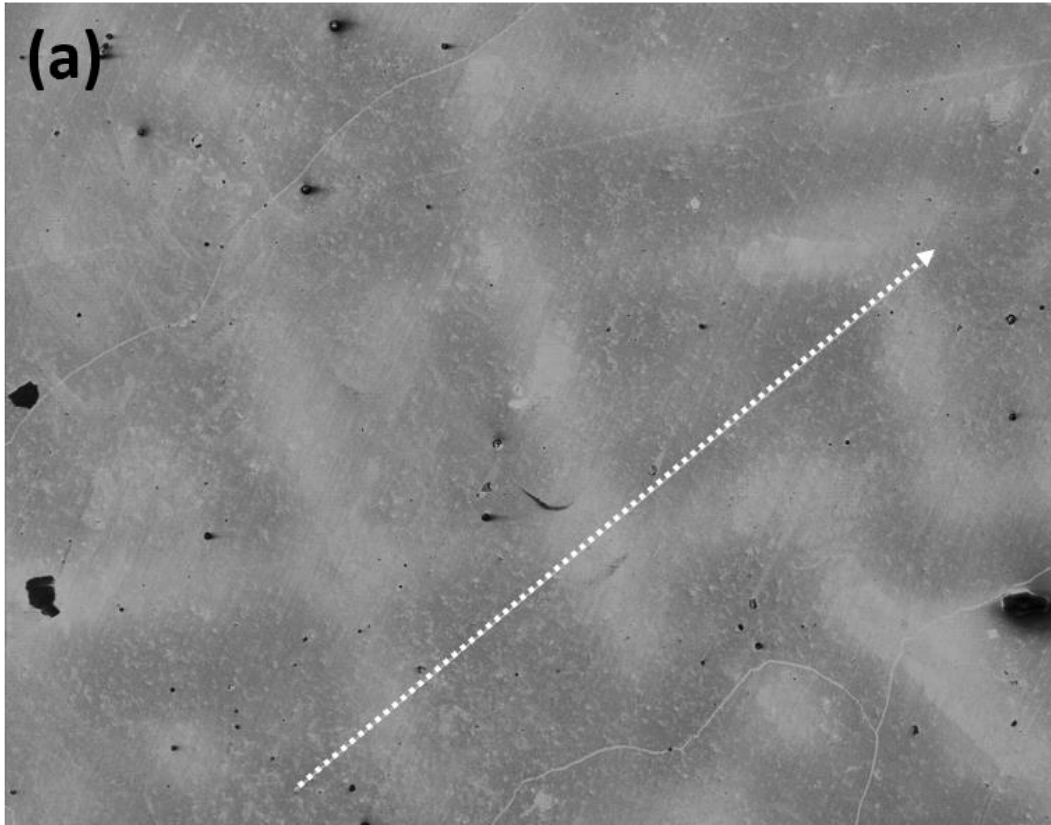


Figure 4.13 (a) The region selected for the EDS line Analysis from the specimen S0.5 (b) Linear compositional change across the line shown in (a).

The insufficient homogenization heat-treatment may cause chemical segregation in superaustenitic stainless steel. Since Mo has much larger atomic radius than the other alloying elements [1], its diffusion during the homogenization must be slower than the other elements. The Mo rich regions constitute energetically favorable regions for Mo rich precipitates to nucleate and grow. It should be noted that the precipitates reported on the literature (Laves and σ) and the one described in this study are rich in Mo. Therefore, these inhomogeneities may facilitate the formation of Mo-rich precipitates upon isothermal heat-treatments. The studies in the literature mainly include the very long term anneals as cited in the literature review chapter [36-40]. In order to compare the behavior of the precipitation in this study with the ones in the literature, a new series of specimens were heat-treated with the annealing times starting from 1 to 16 hours. The resultant microstructures can be seen in the Figure 4.14. According to BSE images, there are two kinds of precipitates; needle-like and brighter Laves phase and square-like and dull sigma phase. The compositions coming from EDS measurements are summarized in the Table 4.3. It should be noted that the Laves and sigma phases are nucleated and grow not only at the grain boundaries but also within the austenite grains. Similar studies stating that Mo distribution eases the formation of Laves and sigma phase have been reported in the literature [38]. Figure 4.15 (a) and (b) shows a statistical analysis indicating the percent area covered by the precipitates (both Laves and sigma) and number of the precipitates for a given area. When these results are compared with the ones in the literature, a remarkable difference is seen in terms of the number density and percent area of the precipitates. For a comparison, Figure 2.14 (c) is taken for comparison as the composition and the annealing parameters are similar with the ones used in this study. After 16 hours annealing, the percent area covered by the precipitates is given as 1.8% for Figure 2.14 (c) whereas it is 8% in this study. The number density calculated from Figure 2.14 (c) is 15000 mm^{-3} , whereas it is 71000 mm^{-3} in this study. The precipitation seems to be enhanced for CN3MN used in this study. It is clear that the inhomogeneous distribution of Mo triggers the formation of precipitates. These results are also in good agreement with the previous results. Both the nucleation and the growth kinetics are much more enhanced by the reasons mentioned above.

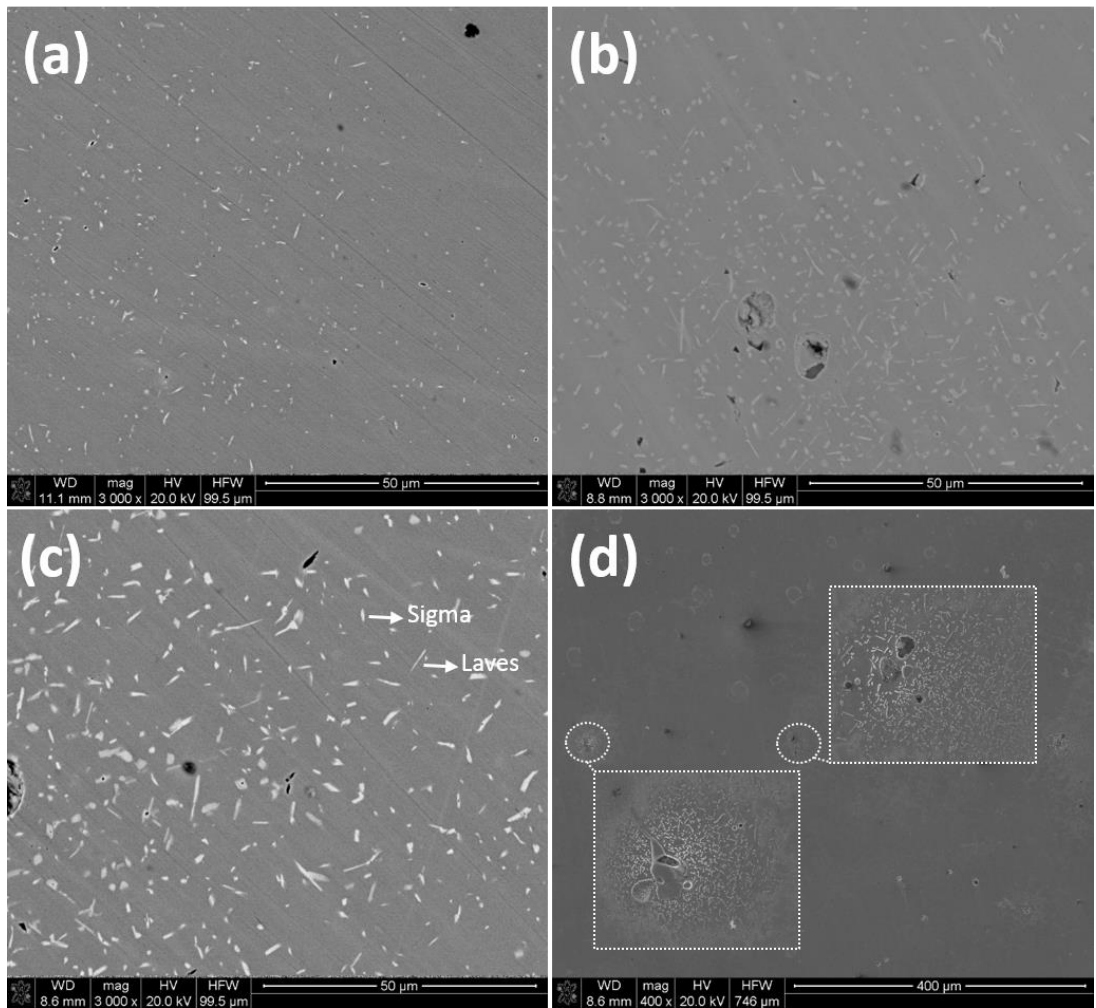


Figure 4.14 BSE images from the specimens (a) S1h (b) S4h (c) S16h (d) S16h showing the distribution of the precipitates.

Table 4.3 EDS measurements of precipitates.

Phases		Si	Mo	Cr	Mn	Fe	Ni
LAVES	Average	3.30	34.82	15.04	0.82	32.05	13.97
	Std. Dev.	0.24	3.02	0.69	0.14	1.56	1.06
SIGMA	Average	6.21	36.31	19.15	0.64	15.22	22.48
	Std. Dev.	0.24	2.30	0.24	0.15	2.34	0.40

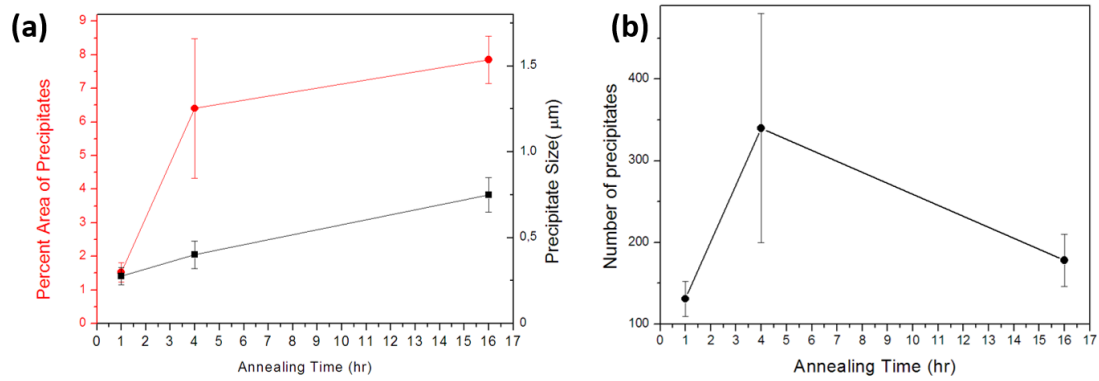


Figure 4.15 (a) The change of percent area and precipitate size (μm) with the annealing time (b) Number of precipitates per $2500\mu\text{m}^2$ with different annealing times.

4.3 Transgranular Embrittlement

So far, the abnormal embrittlement observed in short-term annealing of CN3MN was correlated to intergranular fracture due to the network of precipitates forming along the grain boundaries. The rapid precipitation is related to Mo-rich micro-segregation regions which constitute energetically favorable regions for Mo-rich precipitates and certain slip bands which act as nucleating sites for the precipitates. However, detailed SEM fracture surface analyses revealed that in addition to intergranular, transgranular fracture is also an active mechanism for short-term heat-treated CN3MN specimens. An example for this can be seen in Figure 4.19. In Figure 4.16 (a) and (b), intergranular crack propagates along the grain boundaries and the individual grains are shown. In Figure 4.16 (c) and (d), on the other hand, cracks are parallel to each other and they extend as step-like cleavage planes. In these cases, cracks preferred a definite crystallographic orientation rather than grain boundaries. Since there was no grain boundary failure involved in the fracture, the fracture type is pure transgranular.

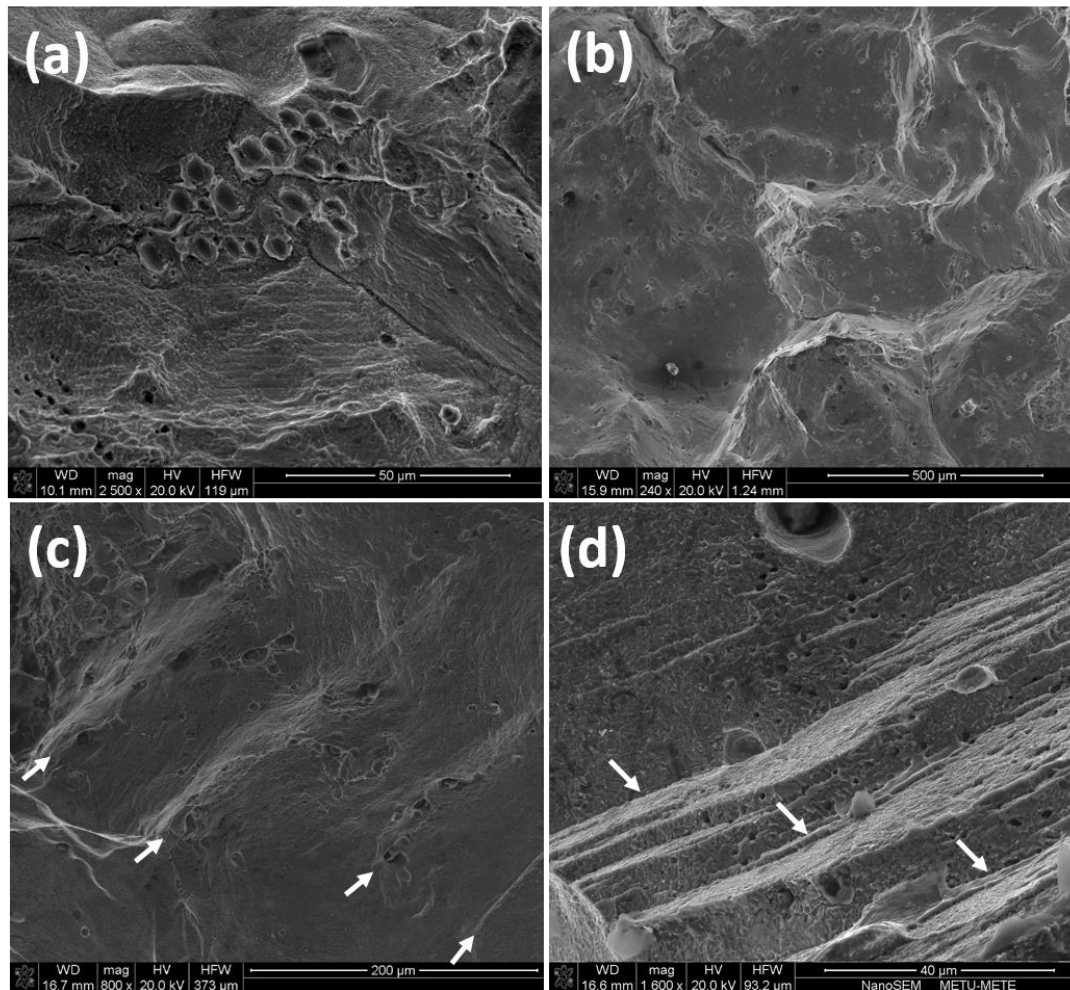


Figure 4.16 Intergranular cracks in (a) S8 (b) S16 and transgranular cracks in (c) S8 and (d) S16.

There are several reasons to expect transgranular fracture in addition to intergranular one in CN3MN grade steel. First of all, CN3MN have relatively large grains so the area covered by grain boundary is quite small as compared to the grains themselves. As the grain sizes increase, the possible sites for precipitation will decrease. The small network of precipitate (as compared to individual grains) will have minor effect decreasing the impact toughness of the specimens. The grain size measurements from the selected specimens are shown in Figure 4.17 and the values are tabulated in Table 4.4. Because of the large size of the grains, measurements were conducted using optical microscopy. At a first glance, the standard deviation seems to be large with respect to the average grain size. This is due to the highly oriented grains formed during the casting operation. The measurements were taken from both longitudinal and transverse direction of the growth direction of the grains. It appears that there is no a

direct relationship between the grain size and annealing time for short-term heat-treatment. As it is seen from the micrographs, the grain sizes are very large as compared to conventional steel grades. Such large grain size means restricted grain boundary area on which the precipitates can grow. Therefore, it can be concluded that this precipitation network cannot be the mere reason of the embrittlement after short-term annealing of CN3MN superaustenitic stainless steel.

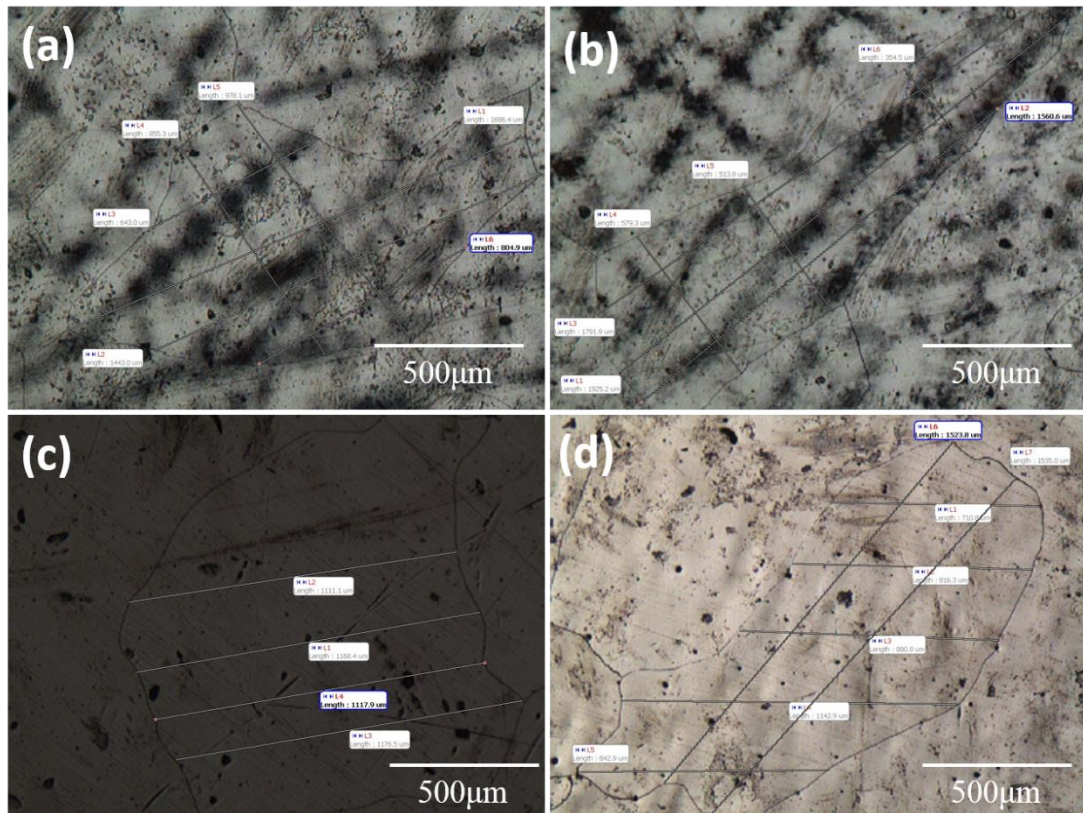


Figure 4.17 Optical microscope analyses for grain size measurement from (a) an equiaxed grain in S0 (b) an oriented grain in S0 (c) an equiaxed grain in S4 (d) an oriented grain in S16.

Table 4.4 Average grain sizes for selected specimens.

Specimen	S0	S4	S16
Average Grain Size (μm)	1048	766	948
Standard Deviation (μm)	518	324	304

The Figure 4.18 shows the XRD patterns of the heat-treated specimens. Since the specimen is in the bulk form having oriented grains, intensities are in strong influence of preferred orientation. The lattice constant of the specimens calculated by XRD analysis is approximately 3.61 Å which is close to the one calculated using SADP. It should be also noted that all the Bragg peaks belong to the austenite phase. There are no peaks which belong to the precipitates or any other second phases even for S16 specimen. This seems to be relatively low to cause any embrittlement; transgranular fracture should be cooperating with intergranular fracture.

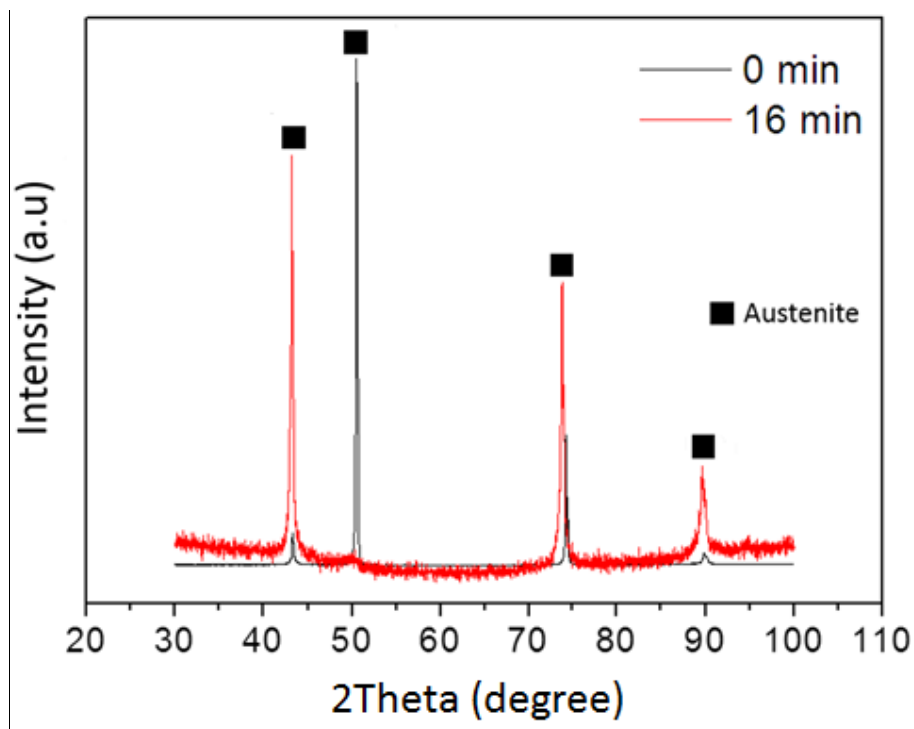


Figure 4.18 XRD patterns of S0 and S16.

For transgranular embrittlement to occur cracks must propagate through the grains. This can be achieved by the existence of crack propagation sites. In this study, two different crack propagation sites were determined, namely, the white-band and the stacking-faults. In the following sections details of transgranular embrittlement will be discussed in details.

4.3.1 White-Bands

In specimen S0, some strange white contrast has been observed within the austenite grains using BF imaging. To our best knowledge, such a structure in stainless steels has not been reported in the literature. These structures will be called as “white-bands”

throughout the text. Figure 4.19 (a) and (b) show examples of white-bands in S0 condition. The cracks already formed within these regions can be clearly seen from BF images. Upon the stress applied during thin foil specimens, cracks initiated and propagated through these white-bands. All the white bands on Figure 4.19 positioned at the tip of the cracks. Another important point is the white bands are parallel to each other. The orientation of these white bands can be estimated from SADPs. According SADP analyses (Figure 4.19 (d)), white bands are found to align themselves towards $\langle 110 \rangle$ direction.

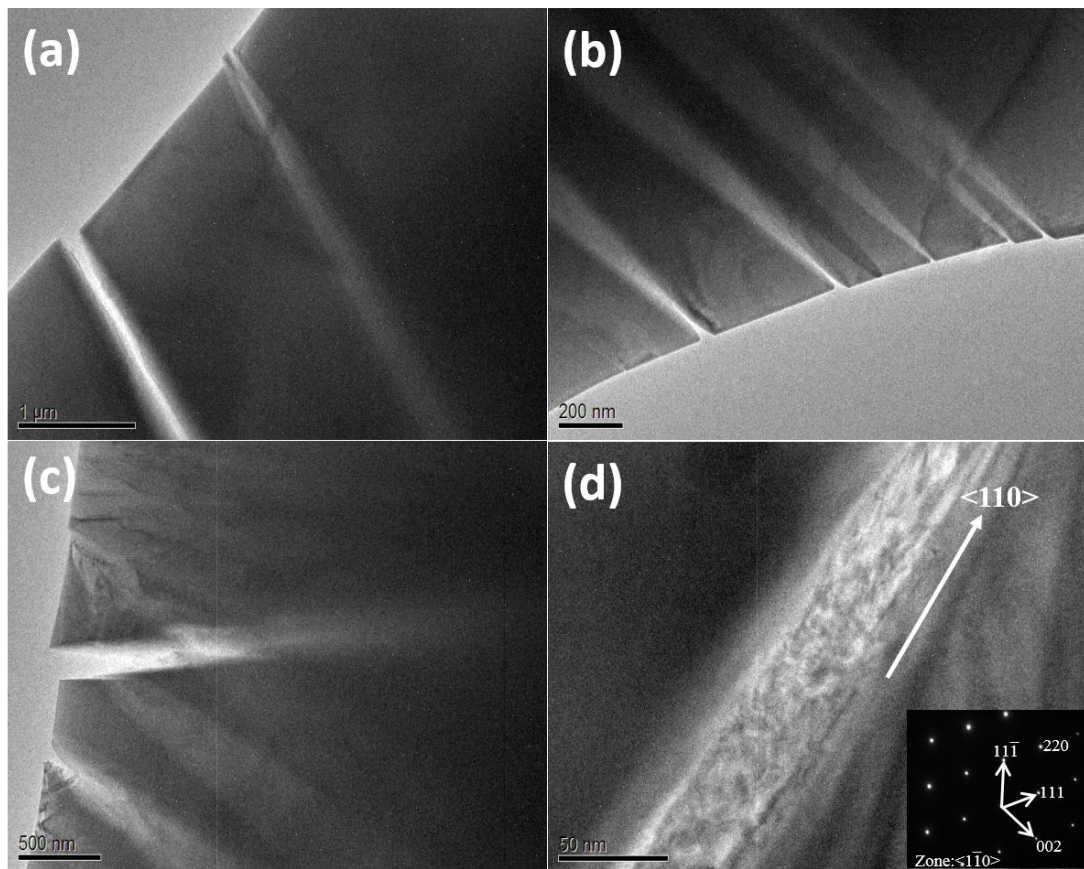


Figure 4.19 (a) BF showing a crack and a white-band just next to each other (b), (c) BF of the white-band at higher magnification, (d) SADP showing the orientation of the white-bands.

The structure of these white-bands was further investigated under HRTEM. Figure 4.20 shows the lattice imaging of a crack being propagated through a white-band region. When the morphology of the tip and edge of the crack are examined in more details, the lattice seems to be broken and no long-range order can be observed. The structure just near the crack, in other words, in the white band, is disordered. This is

also verified by taking the FFTs of different areas from the HRTEM image. The regions where the FFT patterns were collected can be seen on the Figure 4.20 and the corresponding FFT patterns were illustrated as insets on the right hand side of the same figure. The FFT pattern of the Region 1 is from just outer the white band. SADP matches well with the austenite phase.

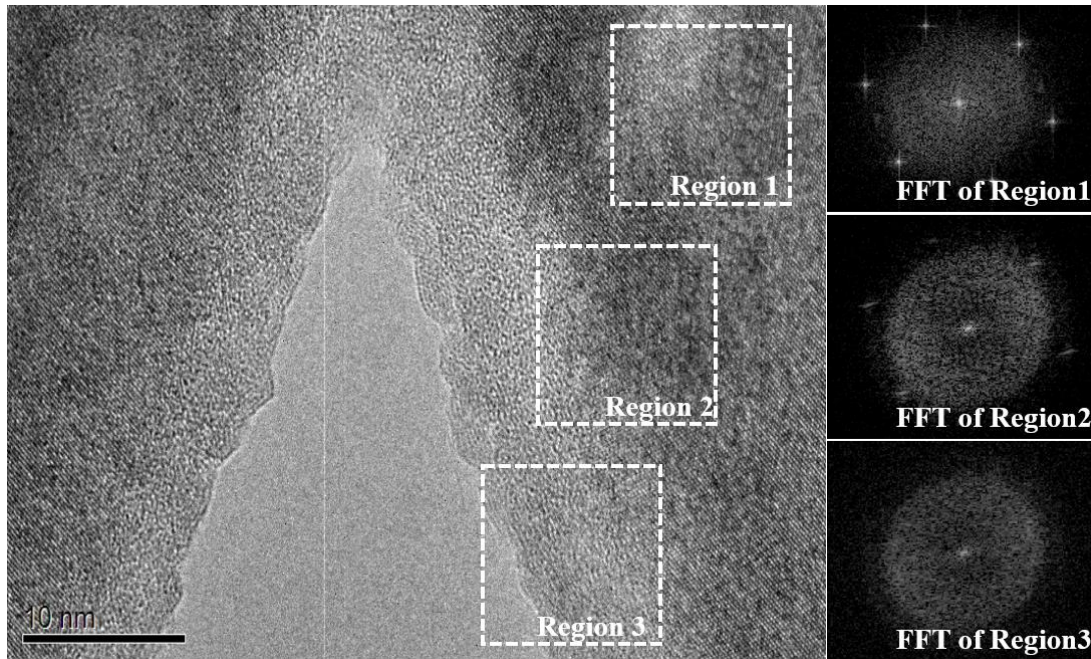


Figure 4.20 HRTEM image at the tip of the crack in S0. The insets on the right hand side represent the FFT patterns collected from the regions shown in HRTEM.

At region 2, the spots representing the austenite phase in FFT are fainter. FFT representing region 3 is lack of any crystal reflections instead there is an amorphous hump indicating a disordered structure around the crack. This is an intriguing observation stating that crack propagates in a disordered matrix. There is possibility that these regions might be resulted from TEM specimen preparation as electropolishing can create disordered regions in the thinnest areas. However, in this study disordered regions are only seen in white-bands. This shows that the disordered structure might be related to some structural aspects rather than being a specimen preparation anomaly. EDS analysis in TEM indicates Ca within the white-bands which is missing in austenite matrix. The EDS analyses were collected from the alternating layers of white-band shown in BF images in Figure 4.21. The EDS results are tabulated in Table 4.5. For the vast majority of the steel grades, Ca is not used as alloying element. Instead, they can be contaminated by addition of Ca-based fluxes during steel

making processes. Alumina inclusions form as deoxidation products in the aluminum-based deoxidation of steel. Alumina has a melting point of more than 2000 °C, hence, these alumina inclusions do not melt and keep their solid phase during steelmaking. The addition of calcium to steel decrease the melting point of these products to nearly 1300 K due to the formation of eutectics and congruently melting phases and it helps the secondary liquid phases pass to the slag. [61]. Ca, in the oxide form, is a very powerful glass forming compound. Moreover, CaO is one the most stable oxide according to the Ellingham Diagrams. Although the dissolved oxygen in the steels is on the order of ppm, this Ca can bound to these oxygen atoms and make CaO. This phase can act as glass former and disrupt the atomic arrangement in very local regions over 10-20 atomic distances and under very high localized stress (because of the quenching).

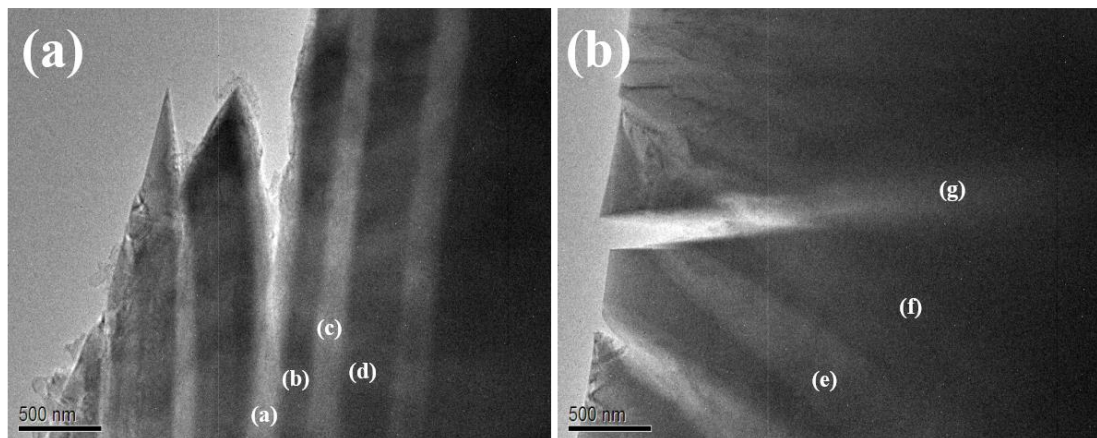


Figure 4.21 BF images showing the alternating layers of white-band and austenite matrix. The EDS measurements were conducted from the labeled layers.

Table 4.5 EDS measurements from the regions shown in Figure 4.24 (wt%).

	Fe	Cr	Mo	Si	Ni	Mn	Ca
Region (a)	45.55	19.31	7.53	0.37	24.93	1.21	1.10
Region (b)	46.18	19.47	7.59	0.45	25.21	1.10	0
Region (c)	45.51	19.68	7.29	0.33	24.83	1.21	1.15
Region (d)	46.58	19.49	7.36	0.39	25.26	0.92	0
Region (e)	44.60	21.02	10.11	1.07	21.86	0.84	0.5
Region (f)	42.60	22.04	17.26	0.21	16.03	1.86	0
Region (g)	43.38	21.62	12.98	0.53	19.28	1.41	0.79

Another interesting point is that these white-bands have been never observed at specimens other than S0. It can be inferred that these structures disappear after heat-treatments. To check whether this is true or not, in-situ heating was applied to the specimen under TEM in order to see the change in real time. One of the set of samples can be seen in Figure 4.22. In Figure 4.22 (a) a single white-band is shown by the arrows in S0 specimen. This specimen was kept at 927°C for 9 minutes. The white-band gradually disappears as seen from Figure 4.22(b) to Figure 4.22(d), respectively.

This can be explained by the diffusion of Ca atoms and revealing the stress concentration during the high temperature annealing processes. As previously mentioned, these white-bands are only observed in S0 condition. They do not cause an abrupt decrease in toughness since S0 has the highest impact energy according to Charpy impact tests (Figure 4.1).

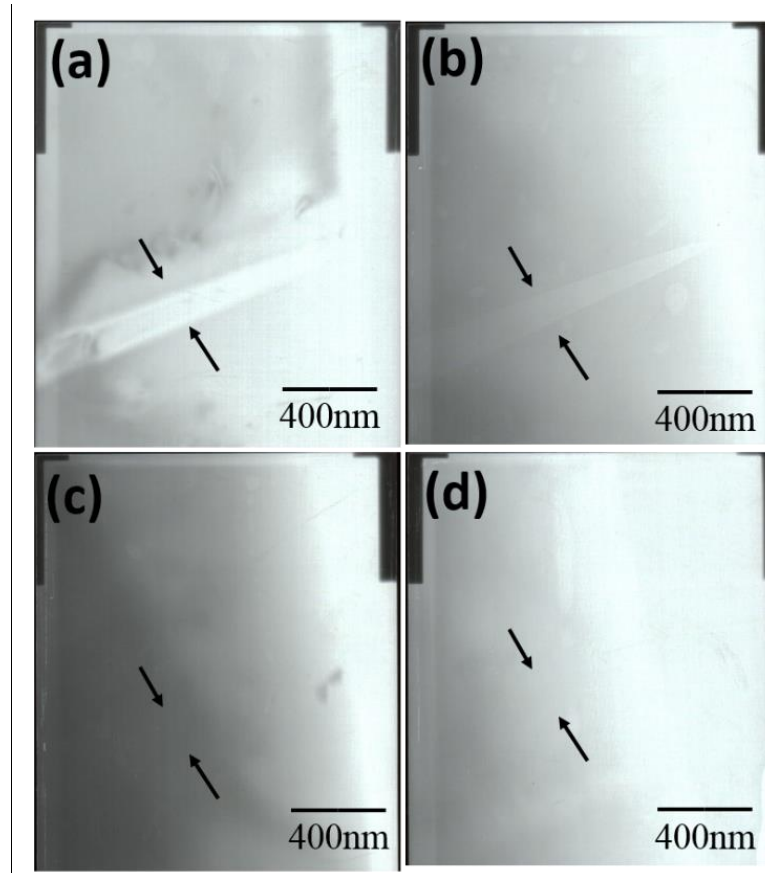


Figure 4.22 BF images of disappearing white-bands during in-situ heating.

4.3.2 Stacking-Faults

Except from S0, all other conditions contain a certain type of zigzag cracks. As it is illustrated in the montaged BF images in Figure 4.26, the cracks always propagate on definite a crystallographic orientation which makes an angle of 60° to each other. When the orientation of the cracks was analyzed with the SADP, it was found that the cracks propagated along the $\langle 110 \rangle$ family of directions. This is the active slip direction in fcc materials. Since those crack are absent in S0, it appears that the matrix structure itself is being strained in some manner as to produce a more brittle structure after the heat-treatment process. Therefore, it can be concluded that some mechanism must hinder the dislocation motion and makes the structure brittle.

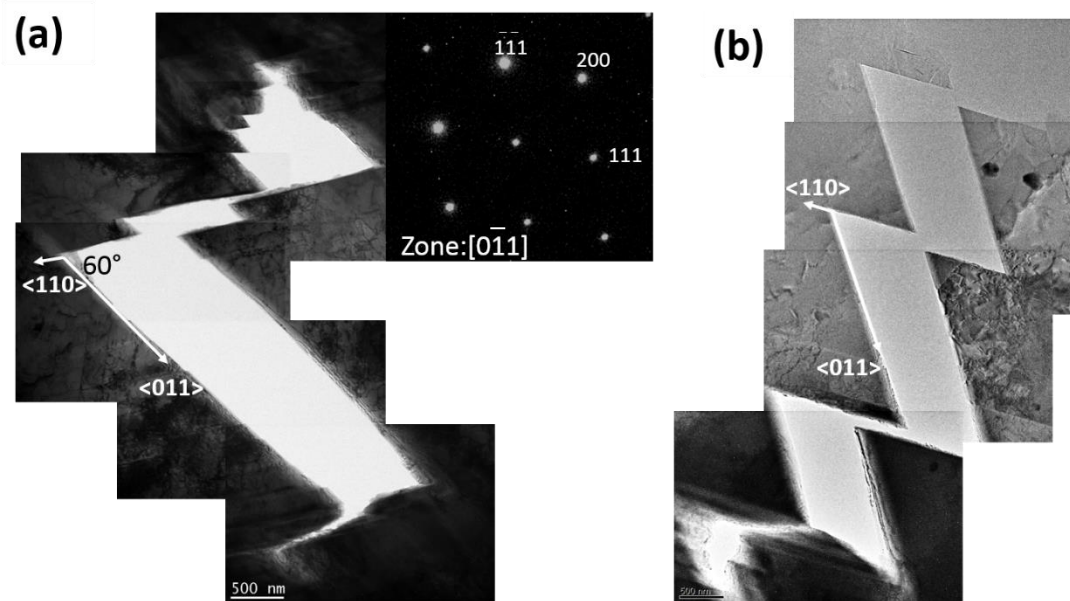


Figure 4.23 Montages BF images of zigzag cracks observed in S0.5.

Similar crack propagation can be also seen in SEM images of TEM thin-foil specimens. Figure 4.23 shows the SEM images corresponding to zigzag crack growth in S0.5. While these cracks definitely resulted during TEM specimen preparation they are only observed in brittle specimens around the defected regions within the grains.

The Figure 4.24 (a) and (c) represent the BF images of zigzag cracks and 4.24(b) and (d) shows their secondary electron (SE) images of the same regions under SEM. It is clear from Figure 4.24(b) that these two cracks are interconnected to each other. Probably, upon a small stress the crack will propagate. These patterns are not localized just near the cracks, but they are spread throughout the specimen as illustrated in the Figure 4.25 (a) and (b). Those cracks are at least 5 microns far away from the electron transparent region. Another important point is that zigzag directions make an angle of 60° , as similar with the cracks shown in Figure 4.23 and Figure 4.24.

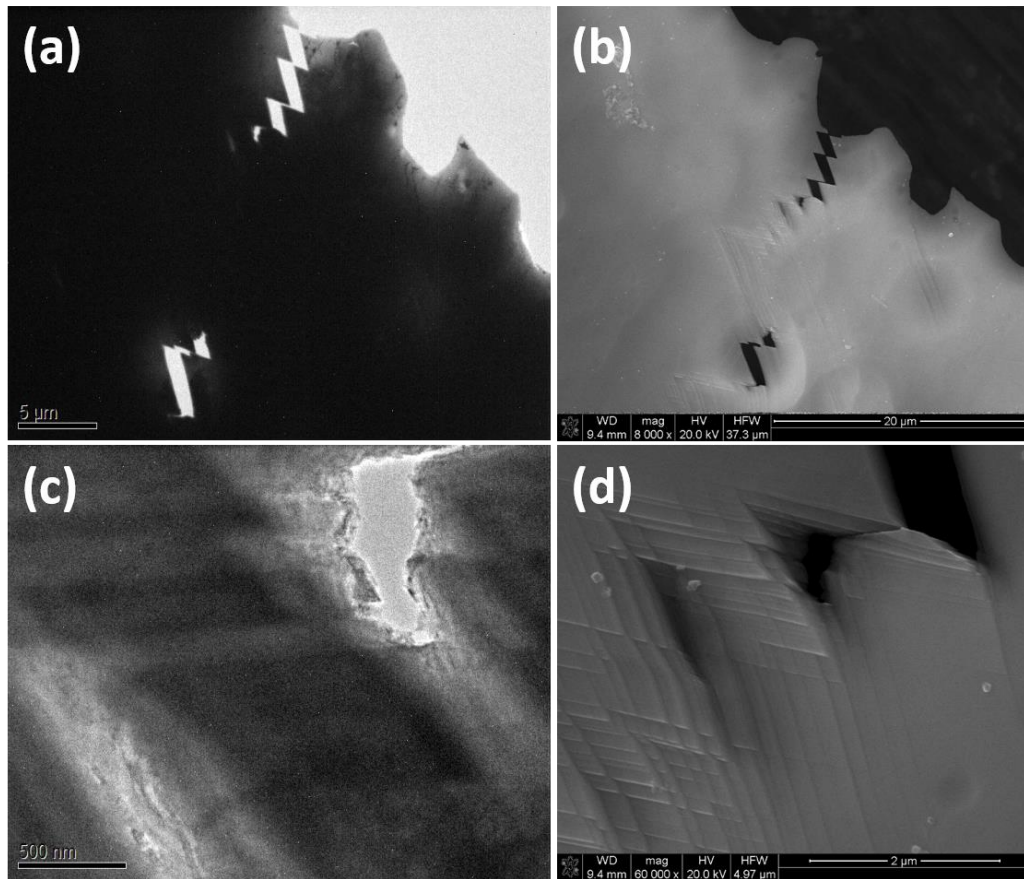


Figure 4.24 (a), (b) The zigzag cracks in S0.5 at lower magnification from TEM and SEM, respectively. (c), (d) same zigzag cracks at higher magnification from TEM and SEM, respectively.

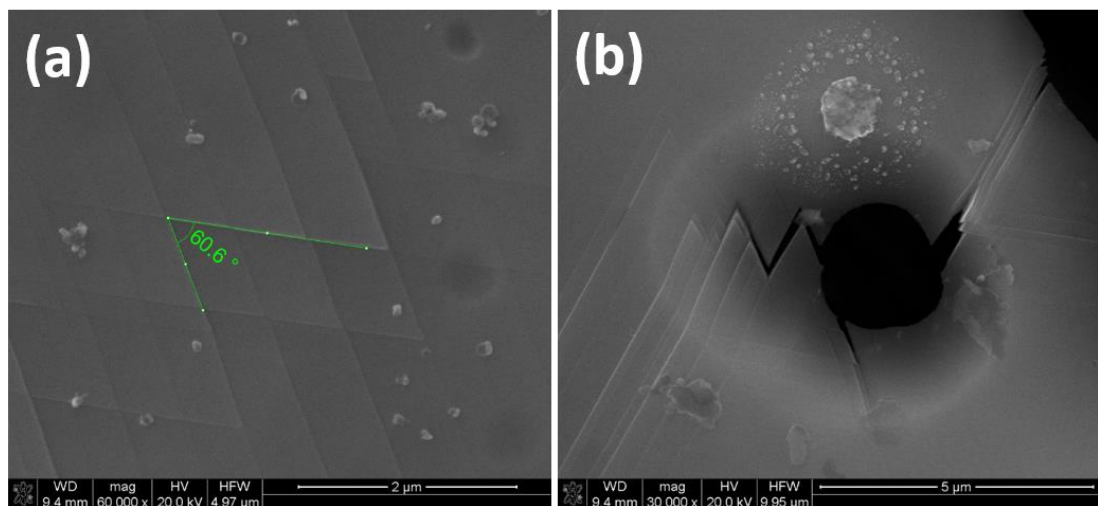


Figure 4.25 (a) and (b) Zigzag patterns observed far from the very thin regions.

At this point, it might be useful to mention the stacking sequences in FCC crystals. Figure 4.26 shows the stacking sequences of fcc crystals in {111} planes in different conditions. In the Figure 4.26 (a) reveals the perfect lattice with no defects, which exhibits ABCABC stacking. The Figure 4.26(b) shows an intrinsic SF when one of the atoms from the A layer is missing. As a result, a local BCBC stacking occurs. This stacking sequence also belongs to the HCP structures. Figure 4.26(c) shows an extrinsic SF which causes Shockley partial dislocation when the extra atom from the C layer is introduced to the system. [43,44,51]

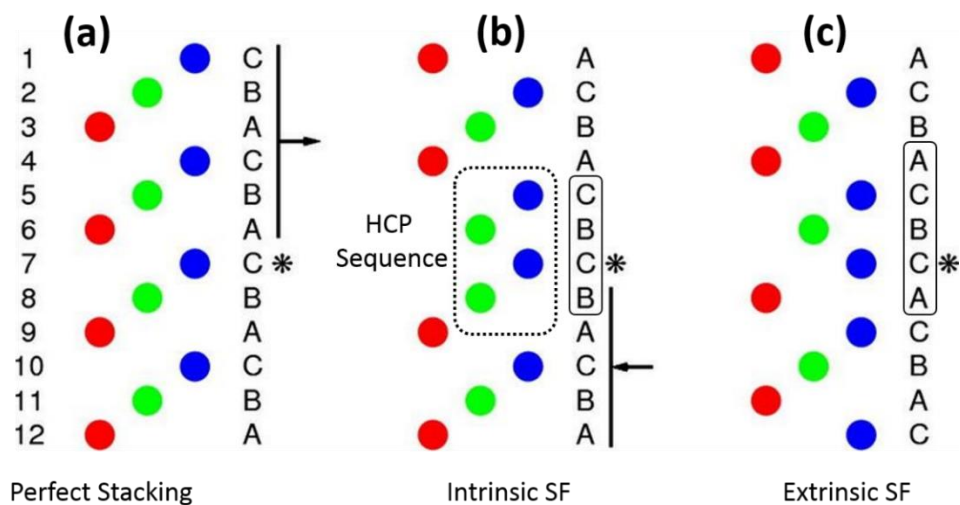


Figure 4.26 Stacking sequences of, (a) perfect lattice and, (b) intrinsic stacking fault and (c) extrinsic stacking fault [62].

Figure 4.27 (a) and (b) show BF and SADP of the region expected to be failed by transgranular zigzag cracks, respectively. The composite SADP pattern revealed a twin-like microstructure. The reflections of the austenite and twinned regions (circled in figure) indicate a twin boundary across (111) planes. Figure 4.27 (c) and (d) show these twin-like structures under HRTEM conditions. A detailed HRTEM analysis of these zigzag twins revealed sub-nanometer wide stacking-fault like imperfection within the matrix. The corresponding FFTs from the austenite matrix and twinned regions match well with the SADP. The most intriguing observation is that the relationship between these stacking-faults and the crack pattern observed in Figure 4.27. It seems that the transgranular fracture follows these stacking-faults observed within the grains. This is also confirmed during our TEM specimen preparations such

that TEM foils cracking of the foil is almost always associated with these defects. Figure 4.27 (e) shows the stacking-faulted regions at a much higher magnification. The dashed lines showed the lines where the stacking sequences were disrupted. HRTEM image shows that the conventional ABCABC stacking sequence changes to the ABCBCABC within the faulted region along the $\langle 111 \rangle$ direction. BCBC stacking sequence is the same as the stacking sequence of HCP structure. These structures are called as ϵ -martensites [57]. The HCP structure is more brittle than the FCC because of the very limited active slip systems at room temperature. Therefore, it is appropriate to say that the majority of transgranular cracks are formed within the brittle hcp-sites inside the tough fcc-austenite matrix.

If the dislocation movement in an alloy is somehow inhibited, the twinning could be the active deformation system. Now the question becomes why twins would prefer to exist within the matrix. In literature, it is known that twinned regions would form whenever the overall stacking-fault energy of the matrix is relatively low [1,49,52]. In order to check whether or not this is true for CN3MN, the corresponding stacking-fault energy was calculated with different techniques.

SFE is an important parameter in physical metallurgy which shapes the deformation characteristics and the microstructure. When the stacking fault energy is low, the probability of a material to exhibit cross-slip or climb becomes difficult. This is due to high energy requirement of wider partial dislocations (i.e. low SFE) for cross-slip as compared to the material with high SFE [43, 49, 64]. If the cross-slip is inhibited, material can fracture in brittle manner.

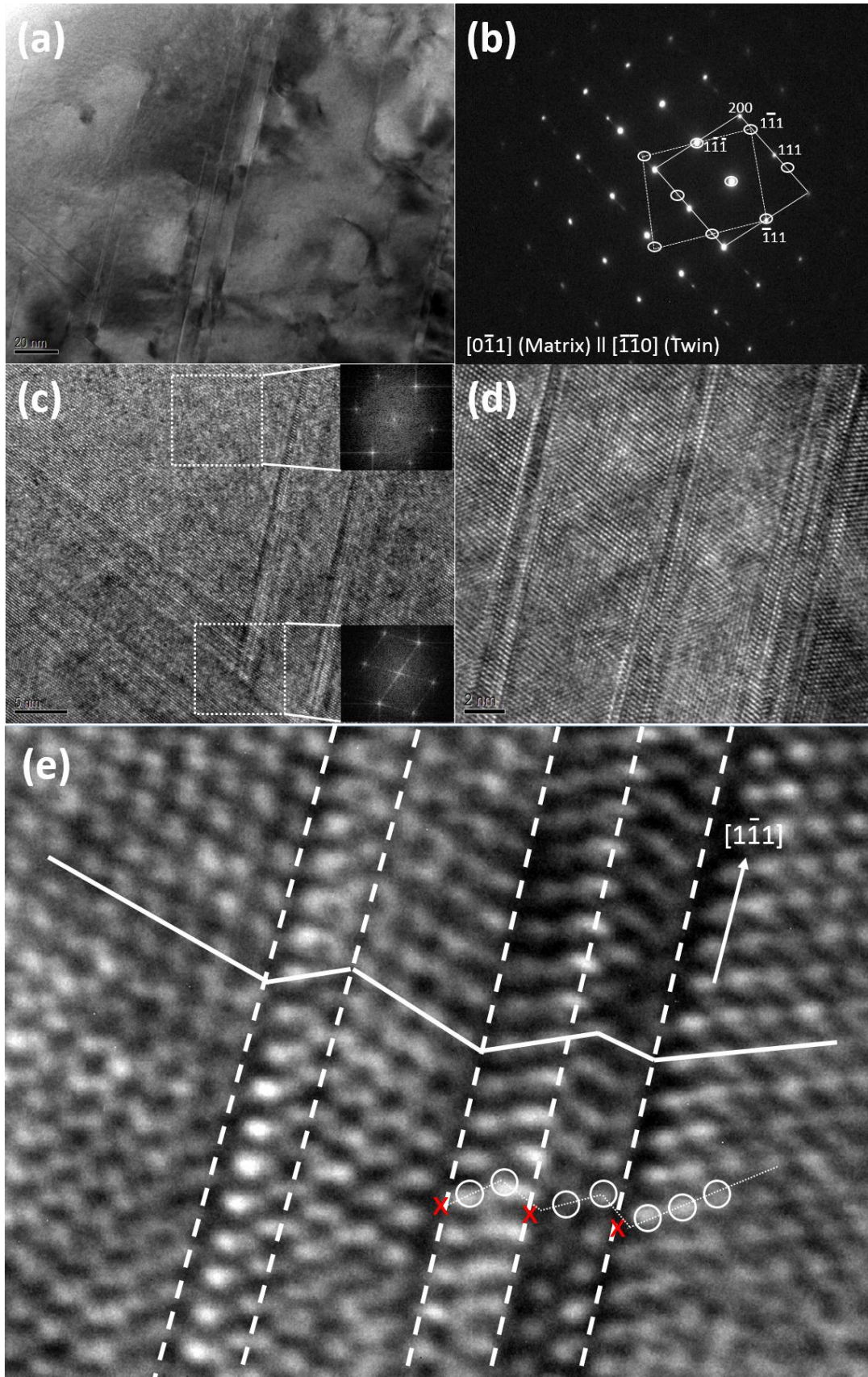


Figure 4.27 The faulted region in S0.5 investigated through (a) BF, (b) SAEDP, (c), (d) and (e) HRTEM imaging.

If a partial dislocation dissociates into two or more partial dislocations, a stacking-faulted region was formed between the partials. Therefore, for this structure to be stable, the SFE of the material should be small. This investigation was conducted to prove that the CN3MN steel has very low SFE.

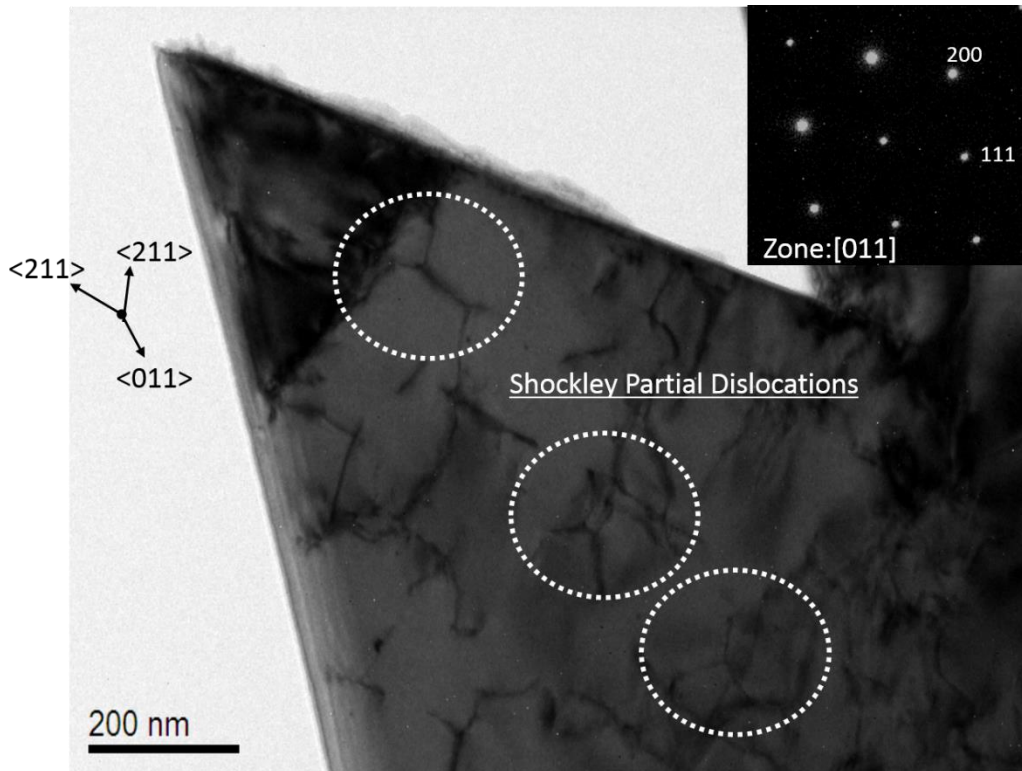


Figure 4.28 BF image of S0.5 consisted of Shockley partial dislocations.

Figure 4.28 showed the typical microstructures evolved in specimen S0.5. It is clear that many dislocations are split into partials. Although a detailed crystallographic analysis should be conducted, the dissociation mechanism can be roughly determined as Shockley partial dissociation due to measured direction vectors. These had no significant effect into embrittlement because they were glissile dislocations and they could move easily upon stress or deformation [44].

However, this is not the case for the condition shown in Figure 4.29. This was an extreme case when the SFE reached to very low values. When the cross-slip is suppressed, dislocations cannot glide towards different planes in the slip systems. Since their movement is limited, they act as sessile dislocations and they made these regions quite brittle. Figure 4.31 (a) and (b) is a nice example for that because

dislocations position themselves at the tip of the crack and they would be preferential crack propagating site upon applying a stress.

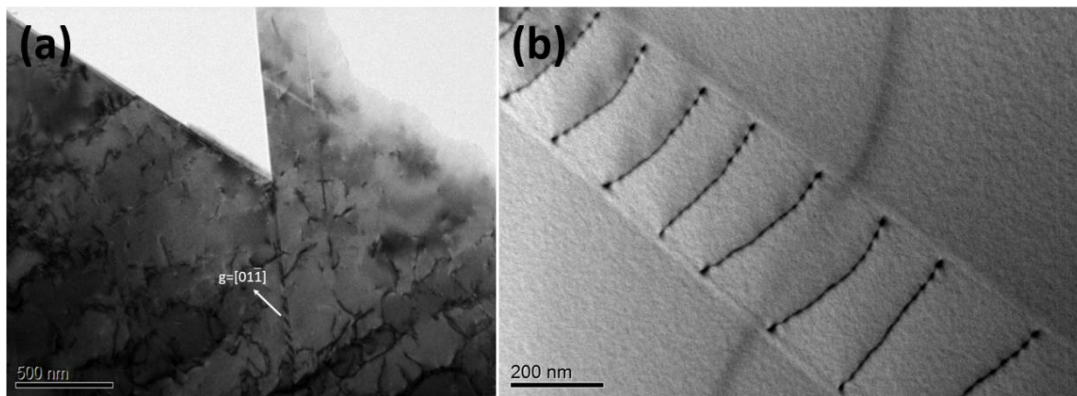


Figure 4.29 BF images of aligned dislocations from (a) S0.5 and (b) S8.

There are many approaches in order to determine the stacking-fault energies in stainless steels. The first approach is based on the compositional parameters. SFE are calculated using the amount of alloying elements. Various empirical formulas and corresponding SFE values for CN3MN are listed in Table 4.6.

According to the Table 4.6, there is remarkable deviation between the results from different studies. Indeed when the composition of CN3MN is substituted into Pickering's approximation, the SFE is found to be negative. One major reason for that is these relationships are only valid for very narrow range of composition. The second reason is that these formulas, except Dai, do not include the interactions between different alloying elements. Finally these formulas do not consider local compositional inhomogeneities and strains which can cause deformation at those regions.

Table 4.6 SFE (mJ/cm²) of CN3MN formulas based on chemistry.

	Equations	Results	Ref
Schramm	$-53 + 6.2*\%Ni + 0.7*\%Cr + 3.2*\%Mn + 9.3*\%Mo$	174	[48]
Rhodes	$1.2 + 1.4*\%Ni + 0.6*\%Cr + 7.7*\%Mn - 44.7*\%Si$	29	[49]
Brofman	$-25.7 + 2*\%Ni + 410*\%C + -0.9*\%Cr -77*\%N - 13*\%Si -1.2*\%Mn$	48	[31]
Pickering	$-25.7+(2*\%Ni)+(410*\%C)-(0.9*Cr)-(77*\%N)-(13*\%Si)-(1.2*Mn)$	-10	[50]
Dai ($\gamma^0=39mJ/m^2$)	$=39+(1.59*\%Ni)-(1.34*Mn)+(0.06*\%Mn^2)-(1.75*\%Cr)+(0.01*\%Cr^3)+(15.12*\%Mo)-(5.59*\%Si)-(60.69*((\%C+1.2*\%Ni)^(0.5)))+(26.27*(\%C+1.2*\%N)*((\%Cr+\%Mn+\%Mo)^(0.5)))+(0.61*(\%Ni*(\%Cr+\%Mn))^(0.5))$	156	[65]

Another approach of calculating SFE is to use XRD patterns. The peak positions stacking fault probability (SFP) need to be calculated for this approach. Silgado *et.al* [66] offered Equation 4.1 and 4.2 where 2θ is the Bragg reflections, in order to calculate SFP. They concluded that the shifts between the diffracting planes from ideal positions come from the stacking faults.

$$(2\Theta_{(200)} - 2\Theta_{(111)})_{CW} - (2\Theta_{(200)} - 2\Theta_{(111)})_{AN} = \frac{45\sqrt{3}}{\pi^2} * SFP * [(\tan\Theta_{(200)} - \tan\Theta_{(111)})] \quad (\text{Eq.4.1})$$

SFE in superaustenitic stainless steel can be calculated as [66] ;

$$\gamma = 17800 \frac{\langle \epsilon^2 \rangle}{SFP} \left(\frac{mJ}{m^2} \right) \quad (\text{Eq.4.2})$$

where SFP is the stacking fault probability, $\langle \epsilon^2 \rangle$ is mean microstrain square. Since XRD results from bulk specimens are used, there might have been errors due to the strong preferred orientation. The preferred orientation has effects on the full width at half maximum (FWHM) of the peaks and since the micro-strain term included the peak breadths, it would make significant errors. Secondly, subtraction of instrumental broadening from the original XRD pattern has prone to additional errors. Therefore, in this study, TEM was used instead of XRD because the easiness of interplanar spacing calculations. The parameters used in calculation are given in Table 4.7. After making

the calculations, the SFE was found to be 29.5 mJ/m² in CN3MN steel. This is a quite low value which facilitates the formation of twins and stacking-faults.

Table 4.7 Parameters used in the SFE calculations.

	CW (S16)	Anneal (S0)
d_spacing (111)	1.923 Å	1.916 Å
d_spacing (200)	1.658 Å	1.633 Å
SFP	0.00805	
ε²	1.33E-05	
SFE(wrt (111))	29.5mJ/m ²	

Another technique for calculation of the SFE is direct measurements of radius of the dislocation nodes. Figure 4.30 showed the geometry of a simple dislocation nodes. Since the radius of the node determined the forces and interactions of the dislocations with the matrix, the force balance must be dependent on this radius [67]

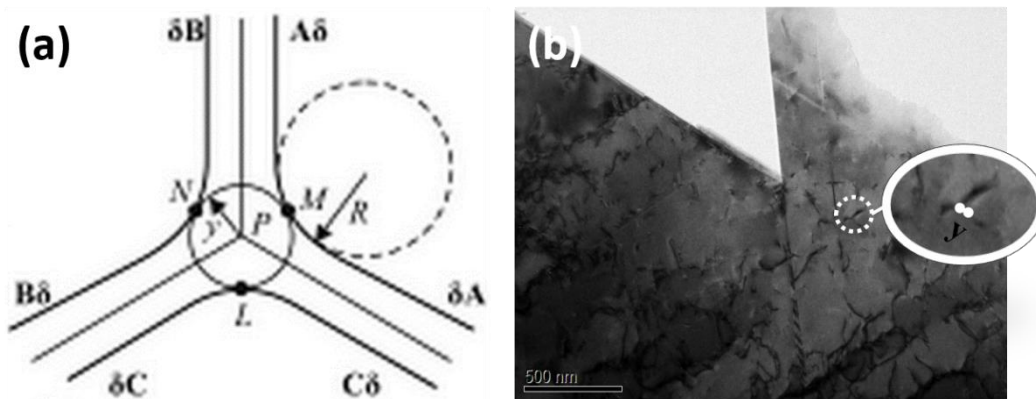


Figure 4.30 (a) The geometry of the dislocation nodes (b) Example of node diameter calculation from S0.5 [65].

The calculations are based on many assumptions. First of all, the dislocation has to be pure edge dislocation with no screw dislocation component. Secondly, all dislocations exist on the same plane no cross-slip should exist. After these assumptions, when the force balance between the dislocation and the matrix is achieved, the SFE can be calculated as;

$$\gamma = \frac{Gb^2}{8\pi\sqrt{3}} * \frac{4.55*(2+\vartheta)*(1-\vartheta)}{y} \quad (\text{Eq.4.3})$$

where G is the shear modulus, b is the magnitude of the burgers vector, ν is the Poisson's ratio and y is the radius of the dislocation nodes [65]. When the physical properties listed on the Table 4.8 are substituted into the equation, the SFE is calculated as $12.0 \pm 4.7 \text{ mJ/m}^2$ after calculating 5 different dislocation nodes. Although several approximations are used, the result is consistent with the findings before. The SFE is sufficiently low enough to suppress cross slip and promote twin formation in CN3MN steel.

Table 4.8 Mechanical properties used in calculations of SFE [1,68].

Physical Properties	
Elastic Modulus (E)	186 GPa
Shear Modulus (G)	69.9 GPa
Poissons Ratio (ν)	0.33
b	2.04Å

Another implication for low SFE can be inferred from Figure 4.31. It is a nice example for the dislocation distribution of low SFE materials. The dislocations are distributed homogeneously throughout the sample, unlike the subgrain formation which is commonly observed in high SFE materials. This type of distribution promotes dislocation-dislocation interactions and block their movements due to the many entanglements of dislocations.

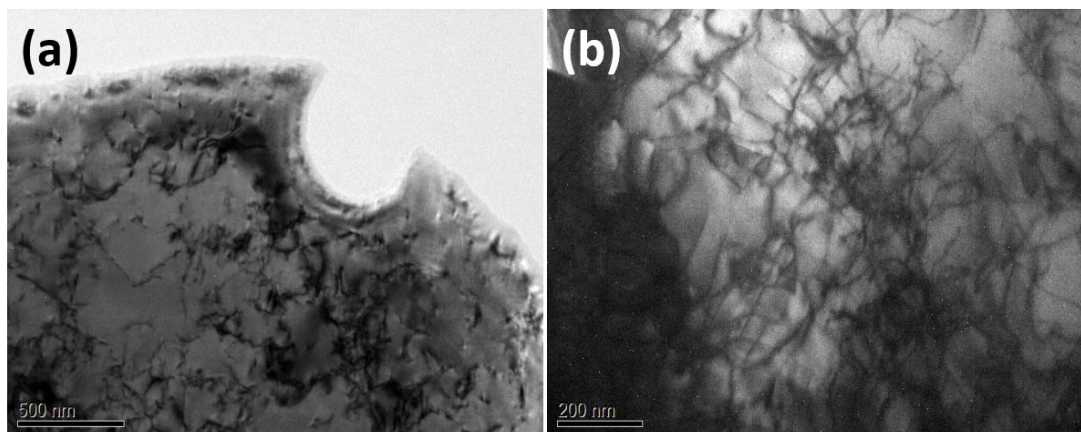


Figure 4.31 (a) and (b) show the dislocation distribution in S16.

Another arrangement of dislocations observed in the CN3MN is illustrated in Figure 4.32. The dislocations are concentrated at some lines linearly, but not like the case in subgrain formation. Murayama *et.al* [64] conducted a study on the comparison of microstructures of Mo and N containing steels with exclusively Mo or N containing steels using the Field Ion Microscopy and Atom Probe Mass Spectroscopy Analyses in order to explain these structures. They concluded that these structures were formed by impingement of Mo-N clusters on the dislocations and they decrease the possibility of cross slip phenomenon. When the Mo-N clusters interact with the dislocations during DSA instead of interaction of only N atoms, the dislocation movement is strictly inhibited. Figure 4.32(c) supports this idea because it caused crack formation just at the tip of these regions like in the Figure 4.32(c) [64].

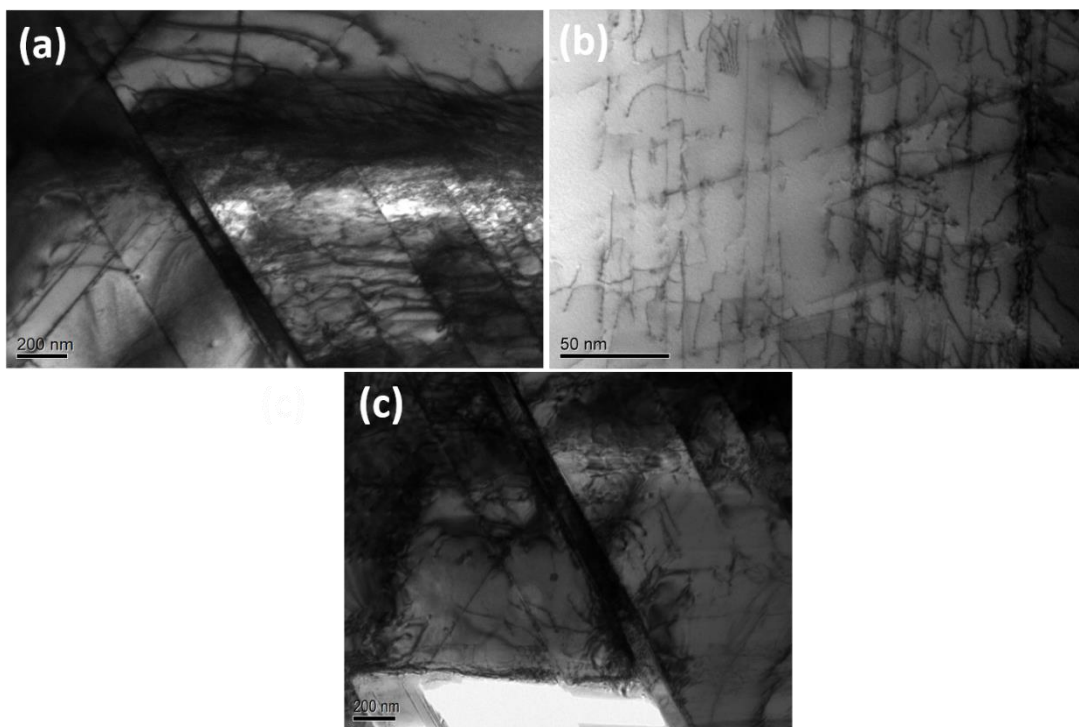


Figure 4.32 Dislocations observed in (a) S8 (b), (c) S16.

CHAPTER 5

CONCLUSION & FUTURE RECOMMENDATIONS

5.1. Conclusions

In this study, the embrittlement observed in CN3MN grade superaustenitic stainless steel after very short annealing times was investigated in details by the use of advanced electron microscopy techniques. The results show a significant drop in fracture toughness of the specimens with increasing annealing time while hardness does not show any significant change. Several mechanisms are proposed to explain this abnormal behavior.

The first mechanism is based on an intergranular embrittlement due to a rapid grain boundary precipitation. The formation of a network of precipitate on the grain boundaries leads to sudden toughness decreases in this highly-alloyed steel. These precipitates could not be matched with any of the known second phase structures (i.e. Laves and Sigma) in stainless steels according to EDS and diffraction studies by TEM. The kinetics of the conventional Laves and sigma precipitation was determined as very sluggish in the literature. However, the kinetics of the newly discovered precipitation investigated in this study is relatively rapid. The local Mo inhomogeneities and casting defects are thought to promote precipitation creating an energetically favorable regions and heterogeneous sites for nucleation and growth of precipitates, respectively.

On the other hand, when the fracture surfaces are examined in details under SEM, there are explicit signs of another failure mechanism. Parallel cracks and cleavage plans are pointing out the existence of transgranular fracture. This makes perfect sense, as the volume ratio of the grain boundaries as compared to individual austenite grains,

was founded to be very low in CN3MN. Moreover, the grain boundary precipitates could not be detected with the resolution of XRD indicating that the overall volume percent of these precipitates should be lower than 1 vol%. TEM analyses revealed twin-like nanodefects formed within austenite matrix matching with the cleavage planes observed in fractography studies under SEM. The cracks are found to propagate along $\langle 110 \rangle$ family of direction, which is the active slip direction for FCC materials. The HRTEM analysis indicated stacking-faults along these defects. The micro scale step-like fracture surfaces are morphologically in good agreement with the defect induced cracking observed within the crystal grains. The stacking sequence of FCC is altered to HCP sequence within the faulted regions. The HCP structure has very limited active slip systems as compared to FCC at room temperature. Therefore, the vast majority of transgranular cracks are formed within the brittle HCP-sites resulting into catastrophic transgranular fracture. The reason of having twinned regions is connected to low stacking-fault energy of CN3MN alloy. SFE was measured to be 12-30 mJ/m² using various TEM techniques.

5.2. Future Recommendations

The underlying reason of having transgranular fracture is connected to having twin-like defects within the austenite matrix. However, the motive of having such defects with respect to short-term annealing could not be clarified. Further computational and experimental studies should be conducted to solve this enigmatic behavior.

The current study mainly includes an embrittlement problem resulted from a specific heat-treatment procedure explained in the experimental procedure chapter. Further optimization studies, based on annealing time and temperature in order to improve mechanical properties, will be very useful. Such a study can also include kinetic software studies such as DICTRA (Diffusion Controlled Transformation) to predict phase formation. It is well known that formation of second phases on the nanometer scale can cause a decrease in the corrosion resistance of highly alloyed steels. In this respect, analysis of the corrosion resistance with respect to applied heat treatments is worth to be investigated.

The characterization techniques used in this study have no ability to detect carbon and nitrogen. Although they are added intentionally at very low amounts, they can play a key role both the precipitation events and decreasing stacking fault energy. In

addition, it is not possible to check whether there is a composition change in the crystallographic defects or not using conventional characterization techniques. For these experiments, an atom probe tomography study would be very useful.

Besides the suggestions above, there are some observations which has not concluded at this study yet. Inhomogeneous Mo distribution is not the only motive for promoting a rapid precipitation in CN3MN steels. Except the S2 and S0.5 all other specimens contain some defected regions, as seen in Figure 4.16. These regions are full of pores and cracks aligned to one another. The interesting point is that as the annealing time increases, these pores are filled up with precipitates. As seen from Figure 5.1(b), the pores are free of any precipitates in S0 condition. However, as shown in Figure 5.1(d) and (f), the pores are filled by the precipitates after certain annealing. When these structures are examined in more details, it is found that the pores and cracks always make an angle of 109.5° to each other, which correspond to the angle between the $\{111\}$ family of planes in cubic structure. Such defects in literature are called slip bands [43,44,56] and they are known to be the trigger of a stress-induced precipitation [57]. The origin of the stress is most likely the two quenching operations applied during the heat-treatments. Since the temperatures before quenching are really high, they may induce thermal residual stresses to the specimens.

The determination of the actual composition of the precipitates within the pores using EDS analysis in SEM is elusive and prone to being incorrect because of the indented nature of the surface. The size of precipitates is extremely small and they are very close to one another. Although EDS cannot be trustful in quantitative analysis of the precipitates within the pores, it gives an idea in terms of compositional variations. An EDS line analysis was conducted within the porous regions and the results are illustrated in Figure 5.2. The variations in the composition between the matrix and precipitates are in good agreement with the previous findings. The precipitates are Mo-riche and Fe-deficient, whereas the matrix is the opposite.

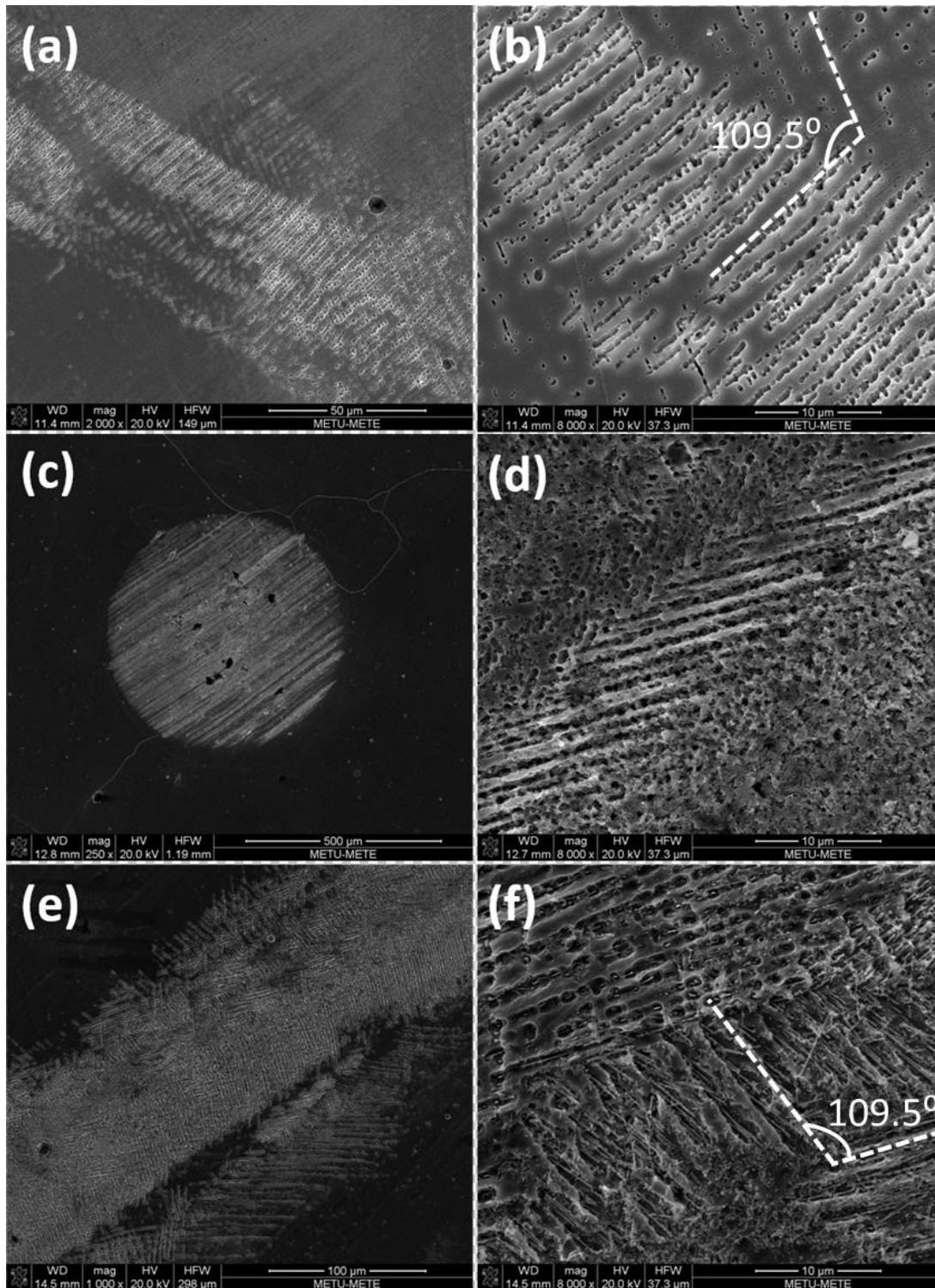


Figure 5.1 Precipitate-free from S0 and precipitate-rich zones from S8 at slip bands.

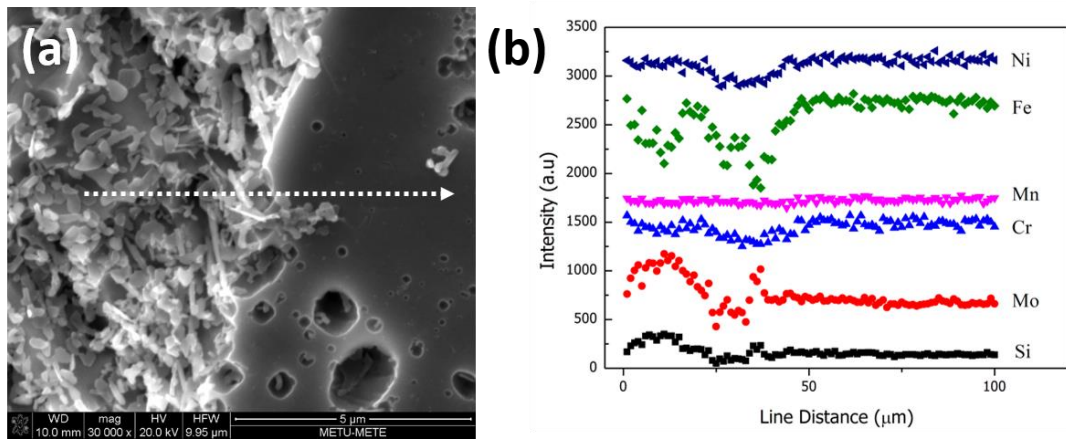


Figure 5.2 (a) Pore filled with precipitates and (b) corresponding EDS line analysis.

Therefore, having the slip bands within the austenite matrix is another factor promoting the formation of precipitation. However, one important question remains; how do these slip band form? Before answering this question, it might be useful to explain the dynamic strain aging (DSA) commonly seen in austenitic stainless steels [58-60]. When the ageing processes occur in alloys containing solute atoms, which can rapidly and strongly segregate to dislocations and lock them during straining, the phenomenon is called as dynamic strain ageing (DSA). In fact, aging can occur at all temperatures, but the processes occur slowly near room temperature and more rapidly at higher temperatures. The maximum effect of DSA can be observed when the solute atoms diffused into the dislocation rich regions. Interstitial solid solution atoms participate more in DSA due to their higher diffusivities. CN3MN contains C and N as interstitial alloying elements which can play critical roles during DSA [58]. The important characteristic of DSA is the formation of slip bands (also known as Lüder Bands) which decrease the toughness and the fatigue life of the steel [58,60]. Although the formation of these bands promote the nucleation of precipitates and decrease the toughness, it should be noted that they do not completely explain the extreme grain boundary precipitation observed in this study since up to 16 minutes precipitates only form along the grain boundaries. Further investigation can be useful to understand the formations of these slip bands and the effects on the mechanical properties.

REFERENCES

- [1] William D. Callister, J. (2007). *Material Science and Engineering - An Introduction*. Utah: Wiley.
- [2] Steel Production by Years.
“<https://www.worldsteel.org/dms/internetDocumentList/bookshop/Word-Steel-in-Figures-2013/document/World%20Steel%20in%20Figures%202013.pdf>”
Last Visited on: 12.06.2014.
- [3] R.E. Smallman, R.J.Bishop. (1999). *Modern Physical Metallurgy*. Oxford: Reed Educational and Professional Publishing Ltd.
- [4] Wever, Archiv für Eisenhüttenwesen, 2 193, 1928-29.
- [5] Schaeffler Diagram (Schneider and Climax Molybdenum Co., Foundry Trade Journal 108, 562, 1960).
- [6] Davis, J. (1976). *Source Book of Stainless Steels*. Ohio: American Society for Metals.
- [7] Powell, G. W. (1948). *Metals Handbook*. Ohio: American Society for Metals.
- [8] D. K. Louie, (2008) *Handbook of Sulphuric Acid Manufacturing, 2nd Edition*, DKL Engineering
- [9] S. Clarke. (2003) “Saramet Alloys – *Applications in Demanding Sulphuric Acid Applications*”, AIChE Convention, Florida, USA.
- [10] Powell, G. W. (1948). *Metals Handbook*. Ohio: American Society for Metals.
- [11] D. Peckner, I.M. Bernstein. (1977). *Handbook of Stainless Steels*. New York: McGraw-Hill.
- [12] ASM Handbook Volume 1: *Properties and Selection: Irons, Steels, and High-Performance Alloys*.
- [13] Wikipedia, 2014, “Martensitic Stainless Steels”
http://en.wikipedia.org/wiki/Martensitic_stainless_steel (Last Visited on: 08.08.2014).
- [14] Verhoeven, J. D. (2007). *Steel Metallurgy for the Non-Metallurgist*. ASM International.
- [15] Heat Treater’s Guide: *Practice and Procedures for Irons and Steels, 2nd Edition*.(1995), ASM International.
- [16] Rickett, R. (1952). Isothermal Transformation, Hardening and Tempering 12% Chromium Steel. *Trans ASM*, 164.
- [17] Harry Bhadeshia, Robert Honeycombe. (2006). *Steels: Microstructure and Properties: Microstructure and Properties*. Cambridge: Elsevier.

- [18] M. Sadeghian, M. Shamanian, A. Shafyei. (2014). Effect of heat input on microstructure and mechanical properties of dissimilar joints between super duplex stainless steel and high strength low alloy steel. *Materials & Design*, 678-684.
- [19] L. Facchini, N. Vicente Jr., I. Lonardelli, E. Magalini, P. Robotti, A. Molinari. (2010). Metastable Austenite in 17–4 Precipitation-Hardening Stainless Steel Produced by Selective Laser Melting. *Advanced Engineering Materials*, 184-188.
- [20] J. Anburaj, S.S. Mohamed Nazirudeen, R. Narayanan, B. Anandavel, A. Chandrasekar. (2012). Ageing of forged superaustenitic stainless steel: Precipitate phases and mechanical Properties. *Material Science and Engineering A*, 99-107.
- [21] ASM Material Data Series. *Worldwide Guide to Equivalent Irons and Steels, 4th Edition*. ASM International, Materials Park, OH, (2000).
- [22] J.O. Nilsson. (1992). Super Duplex Stainless Steels. *Material Science and Technology*, 685-700.
- [23] M.J. Blackburn, J. Nutting. (1964). Metallography of Fe-21%Cr Alloy Subjected to 457°C Embrittlement. *Journal of the Iron and Steel Institute*, 610-613.
- [24] E. O. Hall, S. H. Algie. (1966). The Sigma Phase. *Metallurgical Reviews*, 61-88.
- [25] J.S. Kasper. (1954). The ordering of atoms in the chi-phase of the iron-chromium-molybdenum system. *Acta Metallurgica*, 456-461.
- [26] J.-O. Nilsson, P. Liu. (1991). Aging at 400–600°C of submerged arc welds of 22Cr–3Mo–8Ni duplex stainless steel and its effect on toughness and microstructure. *Material Science and Technology*, 853-862.
- [27] A. L. Bowman, G. P. Arnold, E. K. Storms and N. G. Nereson. (1972). The crystal structure of Cr₂₃C₆. *Acta Crystallographica*, 3102-3103.
- [28] J.M. Vitek, S.A. David, D.J. Alexander, J.R. Keiser, R.K. Nanstad. (1991). Low temperature aging behavior of type 308 stainless steel weld metal. *Acta Metallurgica et Materialia*, 503-516.
- [29] J.W. Cahn, G. Kalonji. (1982). *Proceedings of the Conference on Solid State Transformation*, 3.
- [30] J. M. Vitek. (1987). G-phase formation in aged type 308 stainless steel. *Metallurgical Transactions A*, 154-156.
- [31] K.H. Lo, C.H. Shek, J.K.L. Lai. (2009). Recent Developments in Stainless Steels. *Material Science and Engineering R*, 39-104.
- [32] T.H. Chen, K.L. Weng, J.R. Yang. (2002). The effect of high-temperature exposure on the microstructural stability and toughness property in a 2205 duplex stainless steel. *Materials Science and Engineering: A*, 259-270.
- [33] J.O. Nilsson, P. Kangas, A. Wilson, T. Karlsson. (2000). Mechanical properties, microstructural stability and kinetics of σ -phase formation in 29Cr-6Ni-2Mo-0.38 N superduplex stainless steel, *Metallurgical and materials Transactions A*, 35-45.

- [34] J. Barcik. (1988). Mechanism of σ -phase precipitation in Cr-Ni austenitic steels. *Materials Science and Technology*, 5–15.
- [35] M. Schwind, J. Källqvist, J. O Nilsson, J. Ågren, H.O. André. (2000). σ -Phase Precipitation in Stabilized Austenitic Stainless Steels. *Acta Materialia*, 2473-2481.
- [36] T. Koutsoukis, A. Redjaïmia, G. Fourlaris. (2011). Characterization of Precipitation Sequences in Superaustenitic Stainless Steels. *Solid State Phenomena*, 493-498.
- [37] T. Koutsoukis, A. Redjaïmia, G. Fourlaris. (2013). Phase Transformations And Mechanical Properties In Heat Treated Superaustenitic Stainless Steels. *Material Science and Engineering A*, 477-485.
- [38] N.S.L. Phillips, L.S. Chumbley, B. Gleeson. (2008). Phase Transformations in Cast Superaustenitic Stainless Steels. *ASM International*, 1285-1293.
- [39] C. Muller, L.S. Chumbley. (2010). Fracture Toughness of Heat-Treated Superaustenitic Stainless Steels. *ASM International*, 714-720.
- [40] F. Shi, L. Wang, W. Cui, C. Liu. (2008). Precipitation Kinetics of Cr₂N in High Nitrogen Austenitic Stainless Steel. *Journal of Iron and Steel Research, International*, 72-77.
- [41] F. Vanderschaeve, R. Taillard, J. Foc. (1995). Discontinuous Precipitation of Cr₂N In A High Nitrogen, Chromium-Manganese Austenitic Stainless Steel. *Journal of Materials Science*, 6035-6046.
- [42] P. Shankar, D. Sundararaman, S. Ranganathan. (1994). Cr₂N Precipitation Stages in 316LN Austenitic Stainless Steels. *Scripta Metallurgica et Materialia*, 589-593.
- [43] G.E. Dieter. *Mechanical Metallurgy SI Metric Edition*, New York: McGraw Hill., 1988.
- [44] D.Hull, D.J. Bacon, *Introduction to Dislocations*, Cambridge: Elsevier Ltd., 2011.
- [45] M.C. Marinelli, S. Degallaix, I. Alvarez-Armas. (2006). Dislocation structure developed in the austenitic phase of SAF 2507 duplex stainless steel. *Material Science and Engineering A*, 305-308.
- [46] H. Idrissi, D. Schryvers. (2012). Investigation Of The Elementary Mechanisms Controlling Dislocation/Twin Boundary Interactions In Fcc Metals And Alloys: From Conventional To Advanced TEM Characterization. *Current Microscopy Contributions to Advances in Science and Technology*, 1213-1224.
- [47] C. Wagner. (1957). Stacking faults by low-temperature cold work in copper and alpha brass. *Acta Metallurgica*, 427-434.
- [48] R. E. Schramm, R. P. Reed. (1975). Stacking fault energies of seven commercial austenitic stainless steels. *Metallurgical Transactions A*, 1345-1351.

- [49] C.G. Rhodes, A.W. Thompson. (1977). The composition dependence of stacking fault energy in austenitic stainless steels. *Metallurgical Transactions A*, 1901-1906.
- [50] F.B. Pickering, G.L. Dunlop. (1985). *Proceedings of the Stainless Steels*, 12.
- [51] J.D. Verhoeven, *Fundamentals of Physical Metallurgy*, John Wiley & Sons, 1975.
- [52] Schematic Drawing of Twinning. “<http://practicalmaintenance.net/wp-content/uploads/Schematic-Diagram-of-Twinning-.jpg>” Last Visited on: 19.07.2014.
- [53] ASTM E23-12c, *Standard Test Methods for Notched Bar Impact Testing of Metallic Materials*, ASTM International, West Conshohocken, PA, 2012, www.astm.org.
- [54] W Kurz, D.J. Fisher. *Fundamentals of Solidification, 4th Edition*, Trans Tech Publications, 1998.
- [55] Y.F. Shen, X.X. Li, X. Sun, Y.D. Wang, L. Zuo. (2012). Twinning and martensite in a 304 austenitic stainless steel. *Material Science and Engineering A*, 514-522.
- [56] D.B. Williams, B.C. Carter. *Transmission Electron Microscopy A Textbook for Materials Science*, Springer, 2009.
- [57] T. Koutsoukis, T., E.G. Papadopoulou, S. Zormalia, P. Kokkonidis, and G. Fournalis. (2010). Precipitation Sequences in Cold Deformed Superaustenitic Stainless Steels, *Materials Science and Technology*, 1041-1048.
- [58] H.U. Prasanna, K.R. Udupa. (2013). Dynamic Strain Ageing in AISI 316L Type Stainless Steel as Revealed by Indentation Creep Studies. *Procedia Engineering*, 566-572.
- [59] G. Chai, & M. Anderson. (2013). Secondary Hardening Behaviour in Super Duplex Stainless Steels during LCF in Dynamic Strain Ageing Regime. *Procedia Engineering*, 123-127.
- [60] A. Sarkar, A. Nagesha, P. Parameswaran, R. Sandhya, M.D. Mathew. (2013). Influence of Dynamic Strain Aging on the Deformation Behaviour during Ratcheting of a 316LN Stainless Steel. *Materials Science & Engineering A*, 359-368.
- [61] Clean Steel Part 3.
“<http://www.keytometals.com/page.aspx?ID=CheckArticle&site=kts&NM=200>” Last Visited on 20.01.2015.
- [62] FCC (111) Stacking Sequences
“[https://icme.hpc.msstate.edu/mediawiki/index.php/File:Fcc_\(111\)_Stacking_FFault.jpg](https://icme.hpc.msstate.edu/mediawiki/index.php/File:Fcc_(111)_Stacking_FFault.jpg)”. Last Visited on: 25.01.2015.
- [63] G.D. Huanh, D.K. Matlock, G. Krauss. (1989). Martensite formation, strain rate sensitivity, and deformation behavior of type 304 stainless steel sheet. *Metallurgical Transactions A*, 1239-1246.

- [64] M. Murayama, K. Hono, H. Hirukawa, T. Ohmur, S. Matsuoka. (1999). The combined effect of molybdenum and nitrogen on the fatigued microstructure of 316 type austenitic stainless steel. *Scripta Materialia*, 467-473.
- [65] Q.X. Dai, A.D.Wang, X.N. Cheng, X.M. Luo. (2002). Stacking fault energy of cryogenic austenitic steels. *Chinese Physics*, 596-600.
- [66] J. Unfried-Silgado, L. Wu, F.F. Ferreira, C.M. Garzo, A.J. Ramirez. (2012). Stacking fault energy measurements in solid solution strengthened Ni–Cr–Fe alloys using synchrotron radiation. *Material Science and Engineering A*, 558, 70-75.
- [67] Shetty, M. (2013). *Dislocations and Mechanical Behavior of Materials*. Karnataka: PHI Learning.
- [68] Handbook of Tubular Products. “<http://www.duhig.com/Images/Trent-Plymouth/Trent%20Stainless%20Steel%20and%20Alloy%20Tubular%20Products%20Handbook.pdf>” Last Visited on: 21.01.2015.
- [69] American Society for Metals. *Metals Handbook vol. 3. Alloy Phase Diagrams*. (1994) Metals Park, 140-144.

APPENDIX A

Phase diagrams

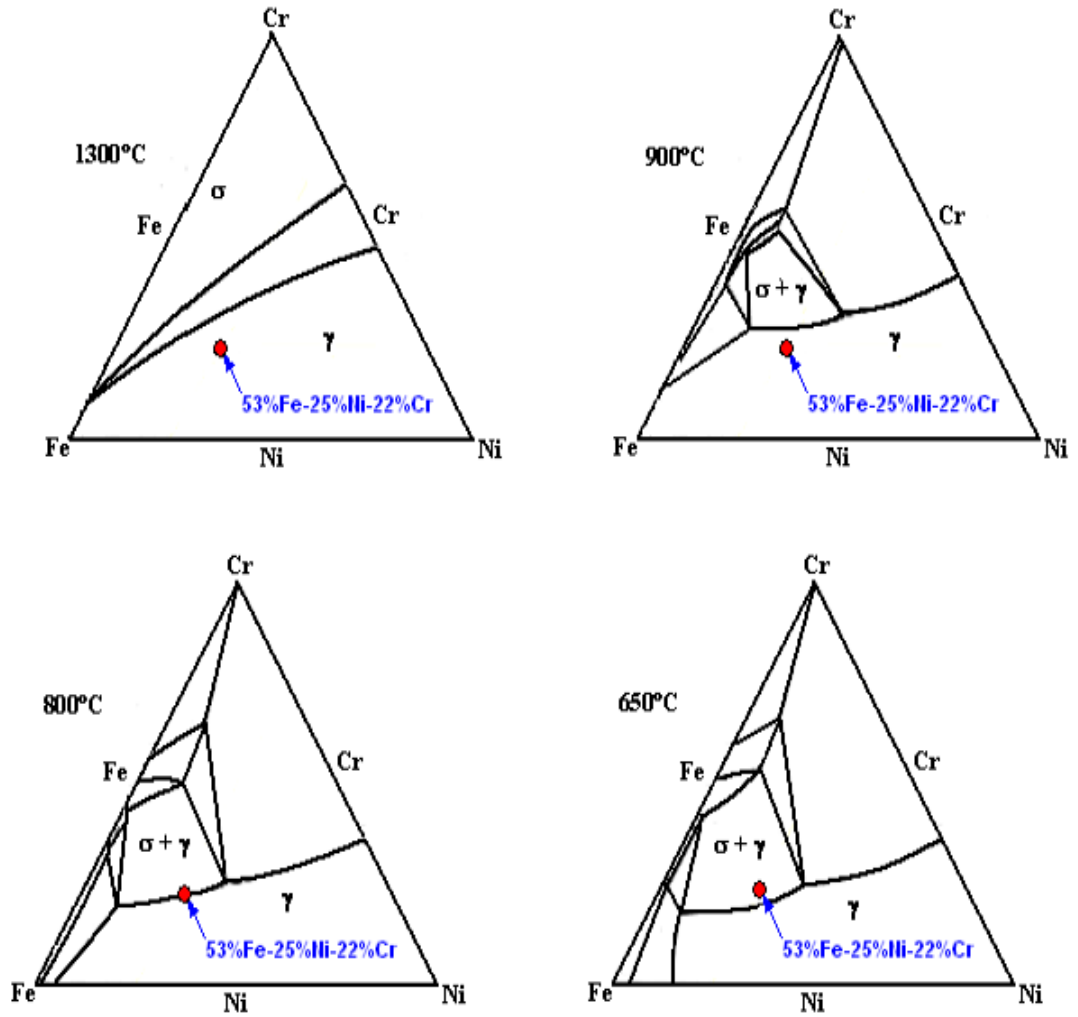


Figure A.1. Isothermal sections from Fe-Cr-Ni Systems [69].

APPENDIX B

SEM Images

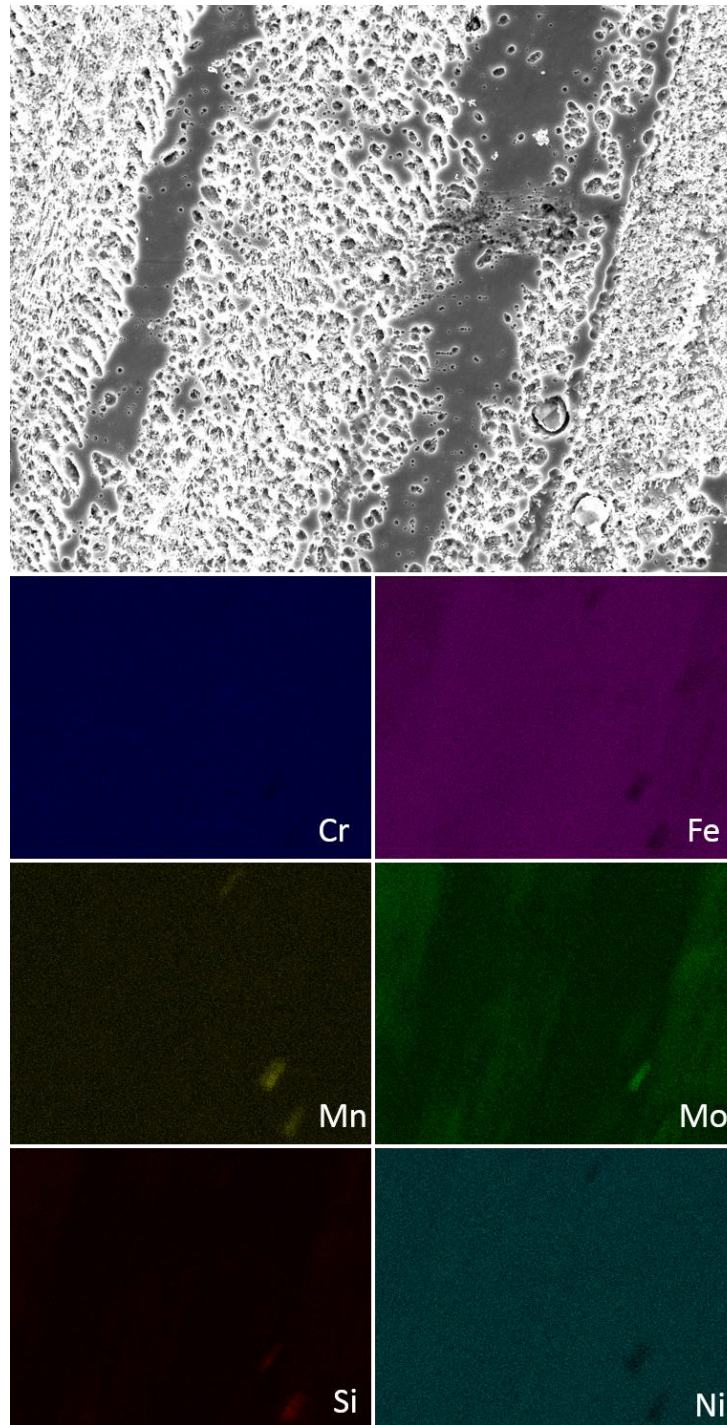


Figure A.2. SE image of precipitations nucleated on the GBs and corresponding elemental maps.